

5-2019

## Investigation of Critical Technologies of Chemical Vapor Deposition for Advanced (Si)GeSn Materials

Joshua Matthew Grant  
*University of Arkansas, Fayetteville*

Follow this and additional works at: <https://scholarworks.uark.edu/etd>



Part of the [Electromagnetics and Photonics Commons](#), [Electronic Devices and Semiconductor Manufacturing Commons](#), and the [Polymer and Organic Materials Commons](#)

---

### Citation

Grant, J. M. (2019). Investigation of Critical Technologies of Chemical Vapor Deposition for Advanced (Si)GeSn Materials. *Graduate Theses and Dissertations* Retrieved from <https://scholarworks.uark.edu/etd/3211>

This Thesis is brought to you for free and open access by ScholarWorks@UARK. It has been accepted for inclusion in Graduate Theses and Dissertations by an authorized administrator of ScholarWorks@UARK. For more information, please contact [scholar@uark.edu](mailto:scholar@uark.edu).

Investigation of Critical Technologies of Chemical Vapor Deposition  
for Advanced (Si)GeSn Materials

A thesis submitted in partial fulfillment  
of the requirements for the degree of  
Master of Science in Microelectronics-Photonics

by

Joshua M. Grant  
Southern Arkansas University  
Bachelor of Science in Engineering Physics, 2015

May 2019  
University of Arkansas

This thesis is approved for recommendation to the Graduate Council.

---

Shui-Qing Yu, Ph.D.  
Thesis Director

---

Gregory Salamo, Ph.D.  
Committee Member

---

Hameed Naseem, Ph.D.  
Committee Member

---

Rick Wise, Ph.D.  
Ex-Officio Member

The following signatories attest that all software used in this thesis was legally licensed for use by Joshua M. Grant for research purposes and publication.

---

Mr. Joshua M. Grant, Student

Dr. Shui-Qing Yu, Thesis Director

This thesis was submitted to <http://www.turnitin.com> for plagiarism review by the TurnItIn company's software. The signatories have examined the report on this thesis that was returned by TurnItIn and attest that, in their opinion, the items highlighted by the software are incidental to common usage and are not plagiarized material.

---

Dr. Rick Wise, Program Director

Dr. Shui-Qing Yu, Thesis Director

## **Abstract**

The development of new materials for efficient optoelectronic devices from Group IV elements is the heart of Group IV photonics. This has direct ties to modern technology as the foundation for the electronics industry is silicon. This has driven the development of silicon-based optoelectronics using these other Group IV materials as silicon is a poor optical material due to its indirect band gap when compared to the III-V semiconductors that are used by most of the optoelectronics industry. While efforts have been made to integrate III-V materials onto silicon substrates, the incompatibility with the complementary metal oxide semiconductor process has limited the viability of this due to the high cost associated with the integration. Germanium has shown potential to be a suitable candidate for possible use though the wavelength range that can be covered is limited as it produces direct bandgaps under tensile strain. Tin-based group IV alloys have been studied and have promising potential in achieving high efficiency optoelectronic devices integrated on silicon. Alloys of germanium-tin have produced many direct bandgap optical devices that have demonstrated the potential for this system. Silicon-germanium-tin alloys hold promise for further expansion of group IV photonics by allowing bandgap and lattice tunability for more complicated device structures and material integrations.

The work presented in this thesis was focused on the critical technologies used to develop these materials using ultra-high vacuum chemical vapor deposition for the epitaxial deposition of films with high optical material qualities. Germanium films were grown at low temperature as well as germanium-tin alloys with highly diluted gas ratios directly on silicon substrates. The germanium films served as buffer layers onto which high quality germanium-tin was deposited using silicon substrates. The growth conditions for the germanium-tin alloys began with a high

flow fraction of tin (IV) chloride. The flow fraction of tin (IV) chloride was reduced which led to an improvement in material quality. By using x-ray diffraction, photoluminescence, and other characterization tools material and optical qualities could be determined. This work additionally looked at the initial phase of development of silicon-germanium towards a rhombohedral crystal phase using sapphire substrates.

## **Acknowledgement**

I would to thank advisor, Dr. Shui-Qing (Fisher) Yu, for his unending support in completion of this thesis. His encouragement during this phase of my career have helped me improve in many areas and his leadership has helped me understand the importance of the research and the potential that I have as a researcher. In my journey to reach this point I could think of no other supervisor or advisor that could have seen me through to this end as he has done. I would like to thank Dr. Hameed Naseem for his insight and discussions with things that I did not quite understand about the Custom built CVD system and its needs. I would like to thank Dr. Salamo for agreeing to be on my thesis committee. I would like to thank Dr. Aboozar Mosleh for introducing me to the world of chemical vapor deposition and helping me understand the systems operation and teaching the techniques needed to grow the materials used for this research. I would like to thank Dr. Seyed Amir Ghetmiri for teaching me how to operate and take care of the optical characterization tools that were necessary for this research. I would like to thank Dr. Rick Wise for his understanding and gentle reminders that I needed at times. I would like to thank Mr. Ken Vickers who brought me into the microelectronics-photonics program during a summer research experience for undergraduates and showing me a more interesting career path than the one I had started with. I would like to thank the Institute for Nanoscience and Engineering for use of the characterization tools. I would also like to thank Dr. Andrian Kuchuk for assisting me in measurements and sample preparation.

I would like to finally like to thank all of the members of the research group that helped with various measurements and calculations, and shared information from their own work to help improve the teams efforts. I would like to thank the growth team members who showed me the way and encouraged me to keep improving everyday. Without the growth team members

working together, the pace at which the research progressed would have been substantially reduced.

This work was funded in part by the Air Force Office of Scientific Research (AFOSR) # FA9550-16-C-0016, Air Force Office of Scientific Research (AFSOR) # FA9550-14-1-0205, the National Aeronautics and Space Administration Established Program to Stimulate Competitive Research (NASA EPSCoR) # NNX15AN18A, and the National Science Foundation (NSF) #DMR-1149605. Any opinions, findings, and conclusions or recommendations expressed in this material are those of the author and do not necessarily reflect the views of the Air Force, NASA, or NSF. This research was carried out using the facilities of the High-Density Electronics Center at the University of Arkansas to grow samples as well as growth of films by ASM America Inc.

I would also like to thank those of my family without whose support this would not have been possible. They have been my foundation when I was unsure and my ear when I needed to vent. My partner for life and better half, Mitzi, has been the greatest support I could ever have been blessed with. My father and Ms. Judy were always there when needed and always gave me a little extra encouragement. I would like to thank my dear friend and mentor, Dr. Abdel Bachri, from Southern Arkansas University for pushing me and believing I had what it took to make this possible when I was not convinced myself. To my friends that I have met along this incredible journey, thank you for the great times and good laughs, and while our paths may diverge in the future, I hope that we will always remain close.

## **Dedication**

To Mitzi Jerry, for her unending love and support, to my father for his unshakable faith in my abilities, to my little brother for convincing me to finish my education when I was unemployed and showing me the way (you got to be first this time).



## Table of Contents

<b>Chapter 1</b>	Introduction/Background .....	1
<b>1.1</b>	Motivation .....	1
<b>1.2</b>	Background .....	2
<b>Chapter 2</b>	Cold-Walled Chemical Vapor Deposition System .....	4
<b>2.1</b>	Unique system configuration capabilities .....	4
<b>2.1.1</b>	Gas farm basic description with layout and safety systems.....	4
<b>2.1.2</b>	CVD system description .....	5
<b>2.2</b>	Safety features .....	8
<b>2.2.1</b>	Exhaust system and secondary containment.....	8
<b>2.2.2</b>	Gas leak detection system.....	11
<b>2.2.3</b>	Unique features .....	12
<b>Chapter 3</b>	Growth and Characterization Documentation .....	15
<b>3.1</b>	Introduction .....	15
<b>3.2</b>	Ellipsometry .....	15
<b>3.3</b>	Raman spectroscopy.....	15
<b>3.4</b>	Photoluminescence.....	18
<b>3.5</b>	X-ray diffraction.....	19
<b>3.6</b>	Description of documentation procedures.....	20
<b>3.7</b>	Description of typical growth day .....	23

<b>Chapter 4</b>	<b>UHV-CVD Growth Development of Ge Buffer on Si.....</b>	<b>32</b>
4.1	Introduction .....	32
4.2	Growth matrix that led to buffer recipe.....	33
<b>Chapter 5</b>	<b>Growth of SiGe on Si.....</b>	<b>40</b>
5.1	Introduction .....	40
5.2	Growth on Si (100).....	40
5.2.1	Material characterization .....	42
5.3	Growth on Si (111) growth matrix.....	49
5.4	Growth of SiGe on sapphire.....	53
<b>Chapter 6</b>	<b>GeSn Growth Work .....</b>	<b>60</b>
6.1	Introduction .....	60
6.2	GeSn on Si.....	61
6.3	GeSn on Ge buffered Si .....	64
6.4	Summary .....	74
<b>Chapter 7</b>	<b>Growth of SiGeSn.....</b>	<b>76</b>
7.1	Introduction .....	76
7.2	Growth matrix and results .....	76
<b>Chapter 8</b>	<b>Conclusions and Future Work .....</b>	<b>81</b>
8.1	Conclusions .....	81
8.2	Future work .....	83

8.2.1	Improvement in material quality and composition .....	83
8.2.2	Design and layout of system .....	85
8.2.3	Operation and safety systems.....	86
<b>References</b>	.....	<b>89</b>
<b>Appendix A: Description of Research for Popular Publication</b>	.....	<b>95</b>
<b>Appendix B: Executive Summary of Newly Created Intellectual Property</b>	.....	<b>99</b>
<b>Appendix C: Potential Patent and Commercialization Aspects of Listed Intellectual</b>	.....	<b>100</b>
<b>C.1 Patentability of Intellectual Property (Could Each Item be Patented)</b>	.....	<b>100</b>
<b>C.2 Commercialization Prospects (Should Each Item Be Patented)</b>	.....	<b>100</b>
<b>C.3 Possible Prior Disclosure of IP</b>	.....	<b>100</b>
<b>Appendix D: Broader Impact of Research</b>	.....	<b>101</b>
<b>D.1 Applicability of Research Methods to Other Problems</b>	.....	<b>101</b>
<b>D.2 Impact of Research Results on U.S. and Global Society</b>	.....	<b>101</b>
<b>D.3 Impact of Research Results on the Environment</b>	.....	<b>102</b>
<b>Appendix E: Microsoft Project for MS MicroEP Degree Plan</b>	.....	<b>104</b>
<b>Appendix F: Identification of All Software Used in Research and Thesis Generation</b>	.....	<b>106</b>
<b>Appendix G: All Publications Published, Submitted, and Planned</b>	.....	<b>107</b>

## List of Figures

Figure 1.1: Section of periodic table highlighting area of interest for this research.....	2
Figure 2.1: Schematic showing layout of gas farm for CVD lab wit layout of gas cabinets for gas cylinder connections and safety systems. ....	5
Figure 2.2: Schematic of UHV-CVD system with gas manifold connections and controls.....	6
Figure 2.3: Design layout of secondary containment exhaust system (a) before upgrade and (b) after upgrade showing the measurement points to determine flow rates for major sections.....	9
Figure 2.4: Image of toxic gas detection monitors installed in UHV-CVD lab. ....	11
Figure 2.6. Image of hot wire element and gas inlet taken during maintenance for filament replacement. ....	13
Figure 2.5. Schematic of plasma electrode configuration in UHV-CVD process chamber showing relation to gas inlet. ....	13
Figure 3.1: Schematic of Raman spectroscopy setup. ....	17
Figure 3.2: Schematic of photoluminescence setup.....	18
Figure 3.3. Schematic of XRD setup. ....	20
Figure 3.4: Image of growth traveler first page showing system required checks and signatures. ....	22
Figure 3.5: Image of documentation binders for hardcopy records of all documents pertaining to each sample.....	23
Figure 3.6: Typical image of a sample after removing from load lock prior to initial characterization. ....	25
Figure 3.7: Template for ellipsometry measurements to be used during the initial characterization of samples.....	27
Figure 3.8: Typical Raman template with data from measurement and reference showing a plot of the intensity as a function of Raman shift wavenumber using Equation 3.1.....	29
Figure 3.9: Typical photoluminescence template showing measurement and reference data plots. ....	30
Figure 4.1: (a) Plot to determine growth rates at varying deposition temperatures based on ellipsometry thickness measurements and, (b) a typical Raman spectroscopy plot. ....	35

Figure 4.2: Typical results from samples used for LT/HT Ge buffer layers from (a) ellipsometry measurements, (b) photoluminescence measurements, and (c) Raman measurements.....	36
Figure 4.3: TEM image of GeSn sample showing Ge buffer .....	37
Figure 4.4: Photoluminescence plots of (a) initial and (b) final Ge buffer growths.....	38
Figure 4.5: SEM image of etch pits showing a calculated TDD of $1.1 \times 10^7 \text{ cm}^{-2}$ .....	39
Figure 5.1: Ellipsometry results typical for two samples grown on Si (100) substrates. ....	42
Figure 5.2: Typical Raman results for two SiGe growths on Si(100) .....	43
Figure 5.3: Combined plot of XRD rocking curve for SiGe (004) for growths on Si (100) performed at 0.1 Torr using recipes in Table 5.1.....	44
Figure 5.4: Combined plot of SiGe (004) Rocking curves from growths on Si(100) performed at 1.0 Torr using recipes in Table 5.2.....	45
Figure 5.5: Typical XRD-RSM plot showing relaxed film growth.....	47
Figure 5.6: Typical XRD rocking curve with Gaussian fitting for SiGe samples grown on Si(100) at 1.0 Torr.....	48
Figure 5.7: Plots of growth rate as a function of temperature (a) and SiH <sub>4</sub> flow rate (b).....	48
Figure 5.8: Comparison plot of growth rate versus deposition temperature for sample grown on Si (100) and Si (111).....	50
Figure 5.10: Typical Raman plots for samples grown on Si (111) showing shifted Ge-Ge LO phonon peak shift and Ge-Si LO phonon peaks near $395 \text{ cm}^{-1}$ .....	51
Figure 5.9: Comparison XRD-RC plot for samples grown on Si (111) showing improvement in quality as temperature increases.....	51
Figure 5.11: Typical absorption coefficient plots from ellipsometry measurements showing shifted cutoff wavelengths.....	52
Figure 5.12: Typical XRD-RC plot showing bi-Gaussian fitting (dotted line). ....	52
Figure 5.13: Ellipsometry plots of the absorption coefficient as a function of wavelength for two SiGe samples grown on sapphire .....	54
Figure 5.14: Comparison of Raman plots for two SiGe samples grown on sapphire at (a) 500 °C and (b) 600 °C.....	55

Figure 5.15: Plot of XRD-RC for growths on sapphire (0001) showing differences in Si incorporation as SiH <sub>4</sub> flow rates change for a given temperature .....	56
Figure 5.16: Combined XRD rocking curve plot of SiGe (111) growths on Si(111) and sapphire (0001).....	57
Figure 5.17: Typical x-ray diffraction phi scans along (004). .....	58
Figure 5.18: AFM image of surface showing multiple trigonal structures.....	59
Figure 6.1: Growth rates of (a) Ge and (b) GeSn at varying deposition temperatures.....	62
Figure 6.2: Typical plots for (a) Raman spectroscopy for thin films showing both Si-Si and Ge-Ge LO phonon peaks, and (b) photoluminescence measurements, for samples grown above 350 °C.....	63
Figure 6.3: XRD-RC plots for (a) Ge and (b) GeSn growths showing improvement in low temperature films with the addition of Sn to the crystalline matrix. ....	63
Figure 6.4. Typical reciprocal space map plots of GeSn along (-2-24) plane for (a) sample A and (b) sample B showing relaxed grown films near pseudomorphic to Si. ....	64
Figure 6.5: Comparison plots of GeSn grown at different temps using (a) photoluminescence and (b) XRD-RC. ....	66
Figure 6.6: XRD-RSM plots with corresponding TEM images for samples grown for 30 min at (a) 300 °C, (b) 270 °C, and for 1 hr. at (c) 270 °C.....	67
Figure 6.7: Images of samples grown with varying SiH <sub>4</sub> flow fractions of (a) 2.5 x 10 <sup>-3</sup> , (b) 1.4 x 10 <sup>-3</sup> , (c) 4.5 x 10 <sup>-4</sup> , and (d) 2.3 x 10 <sup>-4</sup> . ....	69
Figure 6.8: Photoluminescence plot of samples for each SnCl <sub>4</sub> flow fraction reduction. ....	70
Figure 6.9: Comparison plots of XRD-RC data from growths using different SnCl <sub>4</sub> flow fractions showing similar positions for GeSn peaks.....	71
Figure 6.10: SEM imaging of sample surfaces from Sn flow fraction reduction test a) cloudy surface from the initial state, b) hazy surface step 1, and c) clear surface from step 3. ....	72
Figure 6.11. Images of sample grown using lowest SnCl <sub>4</sub> flow fraction showing the cloudy surface returning as temperature was decreased. ....	72
Figure 6.12: Normalized PL results from the temperature reduction growths. ....	73
Figure 6.13: XRD-RC 2θ-ω scans of the temperature reduction growths. ....	73

Figure 7.1: Image of SiGeSn sample showing "tree ring" pattern indicating competition for incorporation between Si and Sn.....	78
Figure 7.2: Absorption coefficient plot for SiGeSn on Ge buffered Si from ellipsometry measurements.....	79
Figure 7.3: Typical Raman spectroscopy plot for SiGeSn on Ge buffered Si.....	79
Figure 7.4: Typical PL plot for SiGeSn on Ge buffered Si.....	80
Figure 8.1. Schematic for the gas mixing system.....	84
Figure 8.2: Image of custom designed impeller for the gas mixing system.....	85

## Lists of Tables

Table 2.1: Table of calculated flow rates from Dwyer online software using measured velocity pressures in various blast gate configurations.....	10
Table 2.2: Comparison of results from calculations for flow rates (a) before and (b) after system upgrades using online software from Dwyer.....	10
Table 4.1: Low temperature growth matrix for early stage development of Ge buffer layer.....	34
Table 4.2 High temperature growth matrix for early stage development of Ge buffer layer. ....	35
Table 5.1: The growth matrix for SiGe on Si (100) using low pressure (0.1 Torr).....	41
Table 5.2:.. The growth matrix for SiGe on Si (100) using high pressure (1.0 Torr).....	42
Table 5.3: Calculations showing d-spacing and lattice constant from Bragg's Law, and percentage of incorporation with and without the bowing parameter from Vegard's Law.....	46
Table 5.4: Growth matrix for growths on Si (111).....	50
Table 5.5: Calculated data from XRD rocking curves providing d-spacing and lattice size.....	53
Table 5.6: Refined growth matrix for SiGe on sapphire substrates for deposition temperature and SiH <sub>4</sub> flow rate dependence.....	54
Table 5.7: Calculations of d-spacing and lattice constants using Bragg's Law from the Gaussian fit of XRD rocking curve peaks.....	55
Table 5.8: Table of measurements from AFM image analysis.....	58
Table 6.1: Table of characterization results from Raman and ellipsometry.....	70



## **Chapter 1** Introduction/Background

Silicon continues to be the primary foundation for technology since its introduction into the semiconductor industry over 70 years ago [1]. This material is used in many devices including computers, cellphones, televisions, and radios that have had an impact on the daily lives of the entire world. The advancement of high technology into our daily lives guarantees that Si will continue to have a place in society for many years to come.

### **1.1** Motivation

The impact that silicon as a semiconductor material has had as an integral part of electronics has been limited by its poor optical properties. Silicon based devices for solar cells have been shown to have an efficiency of only 25% for current devices. Other optical devices and detectors based on Si have shown similar poor performance. It is this issue of efficiency of Si photonic devices that has led modern optical systems to use group III-V materials such as, GaAs, InSb, and InGaAs semiconductors which are highly efficient for light emission. This high efficiency is due the electronic band structure, in momentum space, of the materials having the lowest level of the conduction band align with the highest level of the valence band which is the definition of a direct band gap material. The inefficiency of Si as an emitter is due to it being an indirect band gap material in which the previously described alignment does not occur. This lack of alignment requires interaction from phonons, vibrational virtual particles, which reduces the efficiency of the radiative recombination process. The devices developed from III-V materials are typically fragile and require distinctive fabrication practices. These properties lead to III-V materials being expensive and ill-suited to expand optical electronics into the future. This is in contrast to Si as its processing practices have been highly optimized and the material is inexpensive and sturdy. These issues have led researchers to develop other means by which to

use Si as a base for optical electronic materials. This search has led to developments such as the integration of III-V materials grown on Si-based substrates [2]. It is believed that devices based on Group IV material will be more reliable and less expensive than using hybrid III-V on Si materials [3].

## 1.2 Background

The electronics revolution began with germanium which from 1947 to 1960 was the primary semiconductor material used for transistors and diodes [1]. The shift from Ge to Si in 1960 for the fabrication of devices led to its dominance in the electronics industry [1]. Since that time, the use of these semiconductor materials has matured and led to the development of advanced fabrication techniques and device designs. The research into these and other Group IV materials has continued and led to the development of state-of-the-art materials such as silicon carbide. Group IV materials are pure and alloy materials of carbon, silicon, germanium, tin, and lead shown in the section of the periodic table in (Figure 1). For this work, the concentration on the

					2 <b>He</b> Helium 4.0026
5 <b>B</b> Boron 10.81	6 <b>C</b> Carbon 12.011	7 <b>N</b> Nitrogen 14.007	8 <b>O</b> Oxygen 15.999	9 <b>F</b> Fluorine 18.998	10 <b>Ne</b> Neon 20.179
13 <b>Al</b> Aluminum 26.982	14 <b>Si</b> Silicon 28.086	15 <b>P</b> Phosphorus 30.974	16 <b>S</b> Sulfur 32.06	17 <b>Cl</b> Chlorine 35.453	18 <b>Ar</b> Argon 39.948
31 <b>Ga</b> Gallium 69.72	32 <b>Ge</b> Germanium 72.59	33 <b>As</b> Arsenic 74.922	34 <b>Se</b> Selenium 78.96	35 <b>Br</b> Bromine 79.904	36 <b>Kr</b> Krypton 83.80
49 <b>In</b> Indium 114.82	50 <b>Sn</b> Tin 118.69	51 <b>Sb</b> Antimony 121.75	52 <b>Te</b> Tellurium 127.60	53 <b>I</b> Iodine 126.90	54 <b>Xe</b> Xenon 131.30
81 <b>Tl</b> Thallium 204.37	82 <b>Pb</b> Lead 207.2	83 <b>Bi</b> Bismuth 208.98	84 <b>Po</b> Polonium (209)	85 <b>At</b> Astatine (210)	86 <b>Rn</b> Radon (222)

Figure 1.1: Section of periodic table highlighting area of interest for this research.

growth of the Group IV material system SiGeSn, a ternary alloy, was the primary focus. Many technologies have been developed for the epitaxial growth of Group IV materials. Technologies such as chemical vapor deposition (CVD), molecular beam epitaxy, sputtering, and physical vapor deposition have all been used. The growth of the (Si)GeSn materials by MBE have shown promise by producing high material qualities with high compositions of Sn for the GeSn material [4][5]. One of the issues with the MBE growth is that growth rates traditionally are low resulting in low throughput for each reactor chamber. This in turn results in increased expense for each sample growth. The CVD system of material deposition is capable of much higher growth rates and the ability to deposit on more than one substrate at a time. This results in higher throughput but at the cost of material quality. In recent years, techniques have been developed to improve the material quality and composition of these materials. For this research, the processes related to ultra-high vacuum chemical deposition were investigated.

## **Chapter 2** Cold-Walled Chemical Vapor Deposition System

### **2.1** Unique system configuration capabilities

The cold walled chemical vapor deposition system is comprised of several sections. These sections can be broken down into two major groups. The first group is the gas farm that houses the gas precursor sources. The second major group is the cold walled chemical deposition reactor. The major groups are comprised of subgroups that include safety systems and secondary containment exhaust systems.

#### **2.1.1** Gas farm basic description with layout and safety systems

The gas farm for the chemical vapor deposition system (CVD) is detached from the building due to the toxic, flammable, and pyrophoric nature of the precursor gases contained within. The gas farm is comprised of gas cabinets, gas cylinders, spark detectors, ventilation, secondary containment, and emergency shutoff valves (Figure 2.1). The precursor gases of germane, silane, hydrogen, and methane are contained in high pressure gas cylinders that are connected to the chemical vapor deposition system by individual single run lines comprised of double walled stainless-steel tubing with an outside diameter of 0.25 in. Gas flowing through the lines leaves the gas cylinders through a pressure regulator that is connected to an automatic emergency shutoff valve which is connected to the single run tubing. The emergency shutoff valves have pneumatic control solenoids that allows for manual control of the valve during normal operation but automatically closes when a sudden rush of gas would be detected in a line to prevent gas leakage in case of line failures. Precursor process gases from the gas farm flow to the gas manifold of the CVD system only when the emergency shutoff valve solenoid is energized and the controls for the solenoid are located at the gas farm on each gas cabinet and in

the CVD lab.

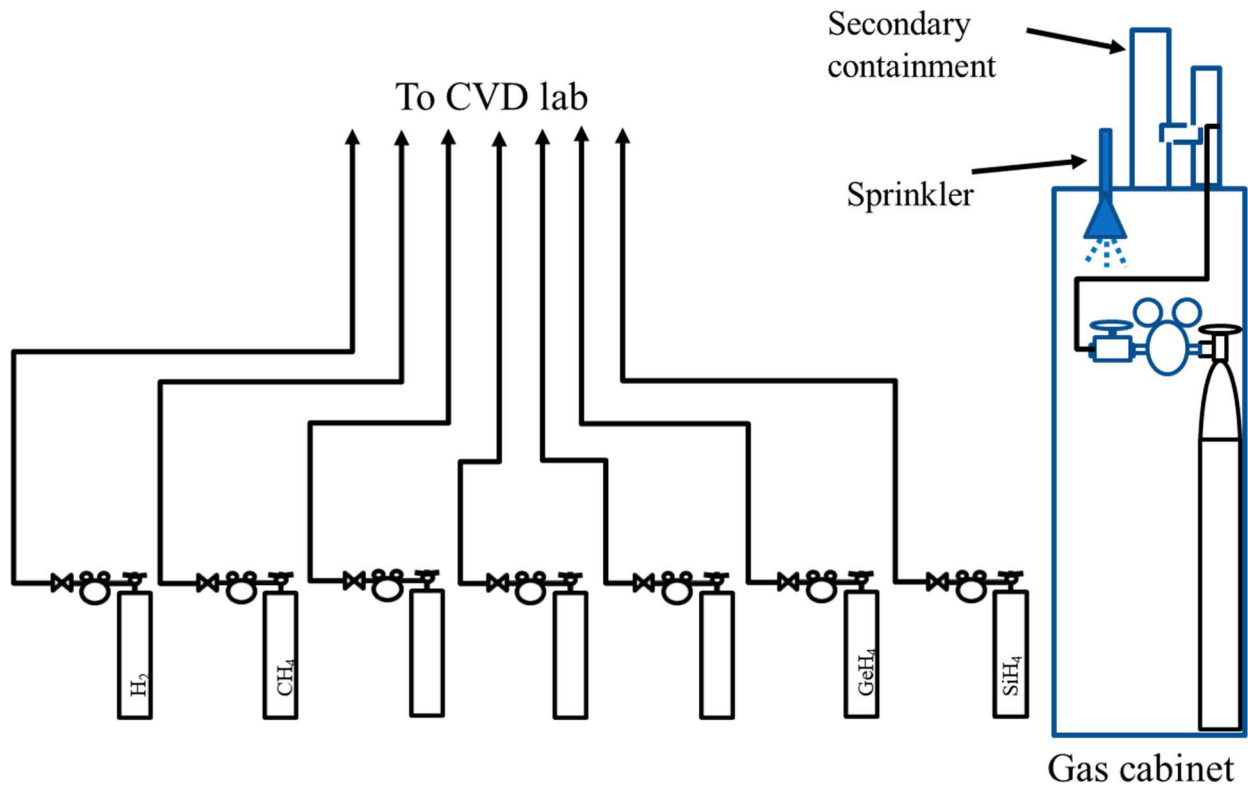


Figure 2.1: Schematic showing layout of gas farm for CVD lab with layout of gas cabinets for gas cylinder connections and safety systems.

### 2.1.2 CVD system description

The chemical vapor deposition system consists of a cold-walled ultra-high vacuum plasma enhanced chemical vapor deposition reactor process chamber, load lock chamber, gas manifold, vacuum pumps, gas reactor column, and a gas mixing system (Figure 2.2). The process chamber and the load lock chamber are identical in size and are separated by a center gate valve. The process chamber for the system is a cold walled design utilizing UHV Design<sup>®</sup> (East Sussex, UK [www.uhvdesign.com](http://www.uhvdesign.com)) Epicentre In-line deposition stage that contains a pyrolytic pressed graphite heating element for sample heating up to 1000 °C. The heater module provides radiative heating to the back side of the substrate that is suspended horizontally below

the heating element by a nickel chromium substrate cradle. The radiative heating of the substrate inside the process chamber is designed to prevent excessive heating of the chamber walls thereby reducing the effect on film defects by contaminants released from the walls. The cradle also acts as the upper biased electrode for the plasma enhancement system and is capable of being rotated

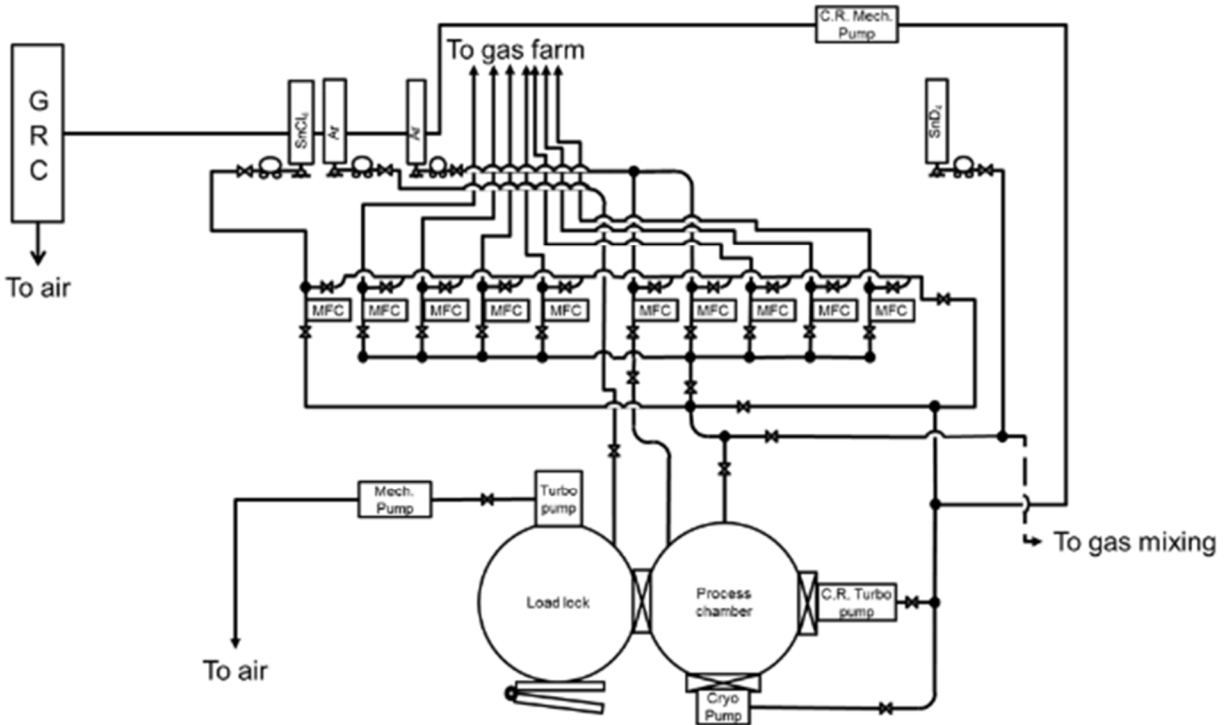


Figure 2.2: Schematic of UHV-CVD system with gas manifold connections and controls.

using an external smart motor by way of a magnetic drive coupling. The plasma systems lower electrode is connected to a magnetically coupled transfer arm that is used to raise and lower the electrode in the chamber. Power for the plasma system is provided by a Seren<sup>®</sup> (Vineland, NJ [www.serenips.com](http://www.serenips.com)) RF power source that is tied to an automatic network matching controller.

The process chamber is differentially pumped using a mechanical pump, a turbo pump, and a cryopump. Using the multiple vacuum pumps the chamber reaches a base pressure in the range of  $10^{-10}$  Torr. The primary pumping is performed by the Edwards model STP 451C

(Burgess Hill, UK [www.edwardsvacuum.com](http://www.edwardsvacuum.com)) corrosive resistant turbo molecular pump that is backed by an Edwards QDP-40 corrosive resistant dry mechanical pump. This configuration is capable of maintaining a pressure range of  $10^{-9}$  Torr. Further pumping using a Marathon<sup>®</sup> CP-8 cryopump (San Leandro, CA [www.marathonproducts.com](http://www.marathonproducts.com)) is required for the process chamber to reach its maximum vacuum base pressure. The process chamber pressure is monitored using an MKS cold cathode gauge (CCG) (Andover, MA [www.mksinst.com](http://www.mksinst.com)) that utilizes an isolation valve to prevent damage from excessive heat and high pressure during growth cycles. During the growth cycle, pressure in the growth chamber is monitored using a one of two MKS Baratron<sup>®</sup> gauges. These gauges are connected to individual MKS pressure controllers. These controllers maintain the possible growth pressures of  $10^{-3}$  to 100 Torr by actuating throttle valves while gas is flowing into the process chamber.

Gas flows reaching the gas manifold are controlled by individual MKS mass flow controllers that are calibrated for each individual process gas that has flow rates less than 100 standard cubic centimeters per minute (scm). Each mass flow controller has the exit solenoid connected to a gas manifold. The mass flow controllers are connected to an MKS power supply/display unit that is capable of monitoring four individual mass flow controllers. The gases are mixed in the gas manifold prior to entry into the process chamber through the pneumatic final entry valve. The gases enter the chamber through the port that contains the hot wire filament, discussed in a later section, passing through a 25 mm tube before exiting near the substrate and cradle. Process gases are extracted from the process chamber using the turbo pump and mechanical backing pump for growths less than 1 Torr or the mechanical pump for growths above 1 Torr. These extracted process gas byproducts are sent to the Edwards gas reactor column that takes the volatile gases and renders them safe by creating inert salts using high

temperatures while exhausting the remaining inert gas to atmosphere.

The load lock chamber is differentially pumped to a base pressure of  $\sim 10^{-8}$  Torr using an Edwards turbo molecular pump backed by an Edwards XDS-10 scroll pump. This configuration allows for the mechanical dry pump to act as a backing pump and a roughing pump simultaneously without installing separate valves for each pump. The load lock chamber serves as the system's entry and exit and contains the transfer arm that has the wafer fork for transferring samples into and out of the process chamber. This chamber is also used to store cleaned and passivated wafers under vacuum conditions lengthening the time passivation will prevent oxide formation on the substrate surface. The chamber is vented using ultra high purity argon gas whose flow is maintained while the load lock is open to reduce contamination from outside sources.

## **2.2 Safety features**

There are many safety features that are installed on the CVD system. These safety systems were installed to ensure safety of not just the lab personnel but the entire facility the lab is in. The systems include the gas monitoring and alarm system, secondary containment system, power protection, and safety interlocks. In this section the exhaust and secondary containment as well as the gas leak detection and monitoring system will be discussed.

### **2.2.1 Exhaust system and secondary containment**

The exhaust and secondary containment are designed to prevent toxic gases from entering the lab in case of leak due to seal or line failure. This system is comprised of gas cabinets, ducting, and exhaust fans. The exhaust fans pull in air from the lab through the ducts and cabinets and pump it to the outside air. The duct work is installed to cover every connection along lines that carry toxic or flammable gases. The current configuration has independent exhaust fans for the gas



farm gas cabinets, the lab gas cabinets, and the mass flow controller manifold cabinet. The gas manifold and lab gas cabinets system was updated due to inadequacies in terms of air flow (measured in cubic feet per minute, CFM) when both the gas manifold and gas cabinets were connected to a single exhaust fan. This was verified by measuring the air flow in the ductwork at multiple points and in multiple blast gate configurations using a pitot tube from Dwyer Instruments (Michigan City, IN [www.dwyer-inst.com](http://www.dwyer-inst.com)) (Figure 2.3). The results of the

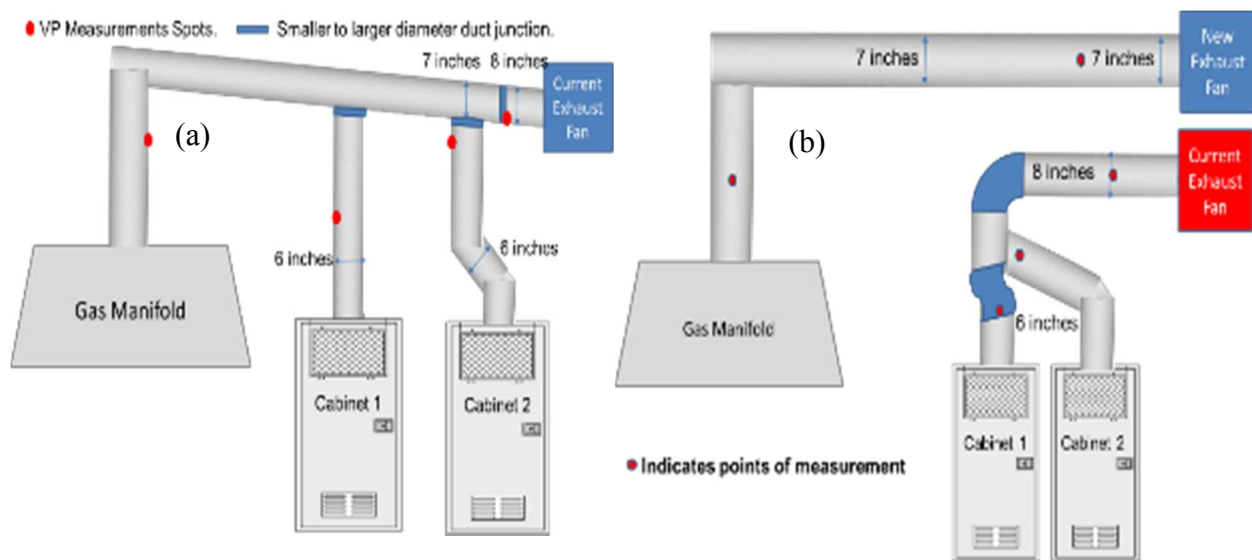


Figure 2.3: Design layout of secondary containment exhaust system (a) before upgrade and (b) after upgrade showing the measurement points to determine flow rates for major sections.

measurements of the velocity pressure taken from the pitot tube on the original design were used to calculate the air flow rate by inputting the system parameters into the online software tool from Dwyer (Table 2.1). The results of this calculation showed that the flow rate through the ductwork was not capable of supporting a minimum of 300 CFM as required by the initial design parameters due to the addition of a second gas cabinet for the gas mixing system, discussed later in Section 8.2. The system was modified by the addition of a second exhaust fan that allowed the gas cabinets and gas manifold to be separated from each other. Measurements were retaken

Table 2.1: Table of calculated flow rates from Dwyer online software using measured velocity pressures in various blast gate configurations.

Position	Manifold		Cabinet 1		Cabinet 2		Final Inlet	
	VP	CFM	VP	CFM	VP	CFM	VP	CFM
All Open	0.05	240	0.06	193	0.07	208	0.65	1131
All Closed	0.4	678	0	0	0	0	0.3	768
Only Manifold+Cabinet 1 are Open	0.11	356	0.13	284	0	0	0.6	1086
Only Manifold+Cabinet 2 are Open	0.14	401	0	0	0.08	223	0.6	1086
Only Cabinet 1+Cabinet 2 are Open	0.02	151	0.06	193	0.07	208	0.6	1086
Only Cabinet 1 Open	0.03	185	0.14	295	0	0	0.55	1040
Only Cabinet 2 Open	0.03	185	0	0	0.11	261	0.55	1040
Only Manifold Open	0.03	185	0	0	0	0	0.65	1131

following the modifications and the results generated showed that the new system had the capacity to not only carry the current demands but maintained the extra capacity for expansion in the future (Table 2.2b).

Table 2.2: Comparison of results from calculations for flow rates (a) before and (b) after system upgrades using online software from Dwyer.

(a) Position	Manifold		Cabinet 1		Cabinet 2		Final Inlet	
Condition/Measurement	VP	CFM	VP	CFM	VP	CFM	VP	CFM
All Open	0.05	240	0.06	193	0.07	208	0.65	1131

(b) Position	Manifold		Manifold Fan inlet		Cabinet 1		Cabinet 2		Cabinet fan Inlet	
Condition/Measurement	VP	CFM	VP	CFM	VP	CFM	VP	CFM	VP	CFM
All Open	0.55	793	0.70	894	0.25	392	0.25	392	0.65	827

### 2.2.2 Gas leak detection system

The gas leak detection system consists of a series of Honeywell Analytics Midas (Lincolnshire, IL [www.honeywellanalytics.com](http://www.honeywellanalytics.com)) gas sensing modules with cartridge inserts tailored to individual gases. These modules are mounted on a wall in the laboratory and connected to the exhaust and secondary containment system with sensing input and output tubes (Figure 2.4). These tubes bring gases into the pump of the module which are then transferred under pressure to the sensing cartridge. Following the measurement, the sampled gases are then exhausted back into the exhaust system. These modules have a sensing range in parts per billion (ppb) of molecules of a particular gas in an atmospheric mixture. The modules are connected to



Figure 2.4: Image of toxic gas detection monitors installed in UHV-CVD lab.

the facility's fire alarm system that provides a visual and audible alarm should a toxic/flammable gas leak be detected. The system is also tied to the emergency shutoff valves in the gas farm and to interlocks on the CVD system. The gas sensors are tied to a network that allows the units to be monitored remotely should a leak be detected. When a gas leak is detected the triggered module will cause all of the valves on the CVD machine and the gas farm to close thereby limiting the risk of exposure. During an alarm condition, the gas sensing modules will also trigger a visual and audible alarm inside the CVD lab. An external gas monitoring panel is also installed by an entrance to the facility nearest the CVD lab. The panel is divided into 16 separate channels that display the current reading of the gas sensing module by means of a 4 to 20 mA signal that is generated by the gas sensing module.

### **2.2.3 Unique features**

The CVD system has multiple unique features that have been added to the initial configuration. These additions, combined with the custom in-house built reactor unit, are what make the CVD system at the University of Arkansas Fayetteville one of a kind. The unique features of the CVD system include plasma enhancement, hot wire filament, and gas mixing. The plasma enhancement system was part of the original reactor system design utilizing an upper and lower electrode that can be biased depending on the location of a shorting plug to make one of the electrodes connect to the earth ground of the machine exterior (Figure 2.5). The system uses a capacitively coupled plasma at a power frequency of 13.56 MHz. The system is capable of producing power up to a maximum of 50 W with an electrode spacing from 20 mm to over 75 mm. The generated plasma generates process gas radicals.

The hot wire filament enhancement is another unique feature to the CVD system. This feature utilizes a tungsten filament that is shrouded to provide for containment of gases injected

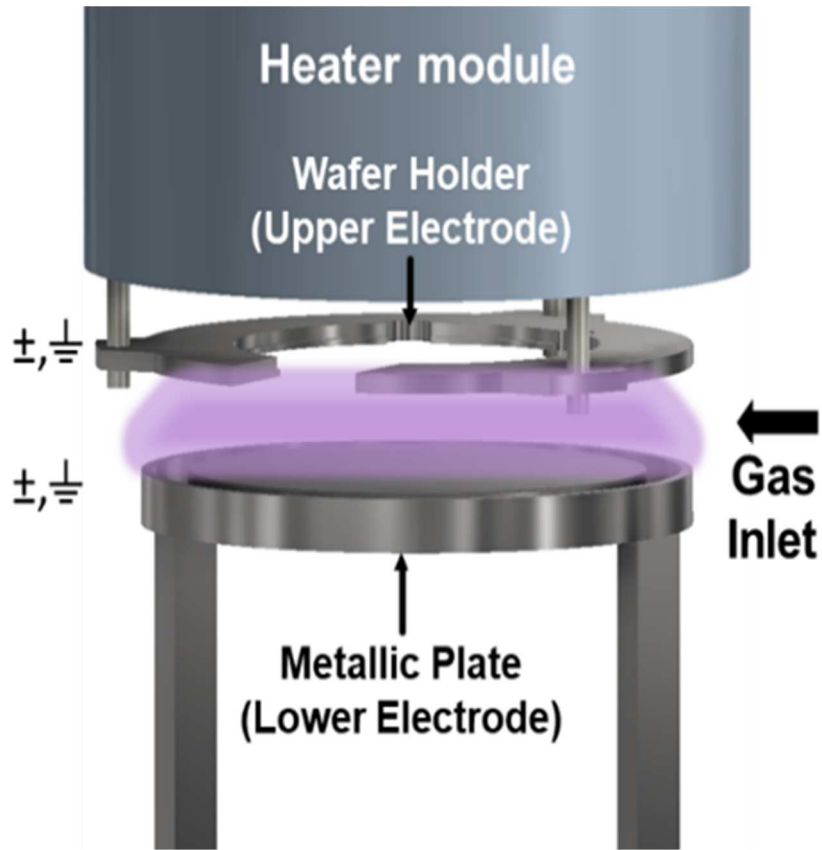


Figure 2.6. Schematic of plasma electrode configuration in UHV-CVD process chamber showing relation to gas inlet.

into the process chamber to ensure that they pass over the element (Figure 2.6). The filament performs as a heating element that reaches temperature high enough to break down hydrogen



Figure 2.5. Image of hot wire element and gas inlet taken during maintenance for filament replacement.

(H<sub>2</sub>) into atomic hydrogen (H). The addition of atomic hydrogen to the CVD growth process can provide enhanced mobility of process gas radicals on the surface of the substrate. This is accomplished by using a direct electrical current which generates light and heat like the filament in an incandescent light bulb. This additional heating of the process gases is also useful when lower growth temperatures are desired by assisting in the breakdown of process gases that normally require high temperatures for surface decomposition.

## **Chapter 3** Growth and Characterization Documentation

### **3.1** Introduction

The materials grown for this study were produced in a custom built cold-walled Ultra High Vacuum Chemical Vapor Deposition (UHV-CVD) reactor with a base pressure of  $10^{-10}$  Torr. The silicon substrates for those samples were prepared using a standard piranha etch cleaning followed by a hydrofluoric acid (HF) passivation. The sapphire substrates were first treated with a titanium coating of the backside of the wafers. The surface was then cleaned with methanol and dried with nitrogen prior to loading into the reactor load-lock. All films were grown as bulk material with no doping as the reactor did not have the capability to use dopants. After each growth cycle, the sample was removed from the reactor and the initial characterizations were performed. The first characterization was ellipsometry followed by Raman spectroscopy, and photoluminescence (PL). Once the initial characterizations were done, samples were chosen for x-ray diffraction (XRD). Transmission Electron Microscopy (TEM) samples were selected from those that had been characterized by XRD. The results of these characterizations are described below along with the description of the characterization set-up used for the measurements.

### **3.2** Ellipsometry

The first characterization used on the grown films was ellipsometry. This characterization was mainly used to determine the film thickness of the grown thin films. The characterization method uses the principle of phase and intensity changes in linearly polarized light as it interacts with a sample. The changes in polarization can occur in one of two forms. The first is a circular polarization in which the light is  $90^\circ$  out of phase, and the second is an elliptical polarization with an arbitrary amplitude and intensity. For this research, a V-Vase<sup>®</sup>

ellipsometer from J.A. Woollam (Lincoln, NE [www.jawoolam.com](http://www.jawoolam.com)) was used for the characterizations. The ellipsometer is divided into two sections with the sample to be measured between them. The first section contains the light source and the polarizer that passes light of a specific polarization. The second section contains the detector and polarization analyzer. The polarized light from the emitter section is reflected off of the sample and is collected by the detector section. The polarization analyzer contains a constantly rotating polarizer that allows different polarizations of light to be sent to the detector. The changes in the polarization of the incident light is measured as  $\psi$  and  $\Delta$  by the ellipsometer. By using a material model and regression analysis the measurements of  $\psi$  and  $\Delta$  can be used to accurately describe a thin film sample. The operating software for the ellipsometer contains a database of material models. However, for materials that are not included in the database, a generalized model must be generated. For the measurements taken, the SiGe and Ge material models were used to provide film thickness and, in the case of SiGe, an estimate of the percent of incorporation of Si in the Ge-rich film. In the case of the GeSn thin films, a generalized model was used to estimate the film thickness and incorporation amount of Sn. This characterization allowed for the determination of growth rates and provided information that could be used to infer the repeatability of a particular growth recipe by comparing the thickness and alloy percentages for multiple samples utilizing the same recipe.

### 3.3 Raman spectroscopy

The second characterization used on the grown films was Raman spectroscopy. Raman spectroscopy is a useful tool in the characterization of epitaxially grown films. Raman can provide insight into a film's crystallinity (whether a film is amorphous or crystalline) based on the shape of the peak and the Raman shift wave number (with units of  $\text{cm}^{-1}$ ) of the peak. Many



factors affect the Raman shift wave number of a sample including composition and strain of the films. The setup used for this study consisted of two light sources, the first of which was a 500 mW 532 nm solid state laser which was filtered to produce 50 mW at the sample. The second light source was a helium neon 632.8 nm producing 5 mW at the sample. The spectrometer used for this setup was a Horiba iHR 550 (Kyoto, JA [www.horiba.com](http://www.horiba.com)) with an attached liquid nitrogen (LN) cooled charge coupled device (CCD) camera. There were multiple mirrors and the appropriate notch filters and beam splitters were used for each laser. The CCD camera was cooled to a temperature between 140 and 150 K. The system was set so only one source could be used at a time and the beam paths were set so that they both converged at the focusing objective and the spectrometer (Figure 3.1).

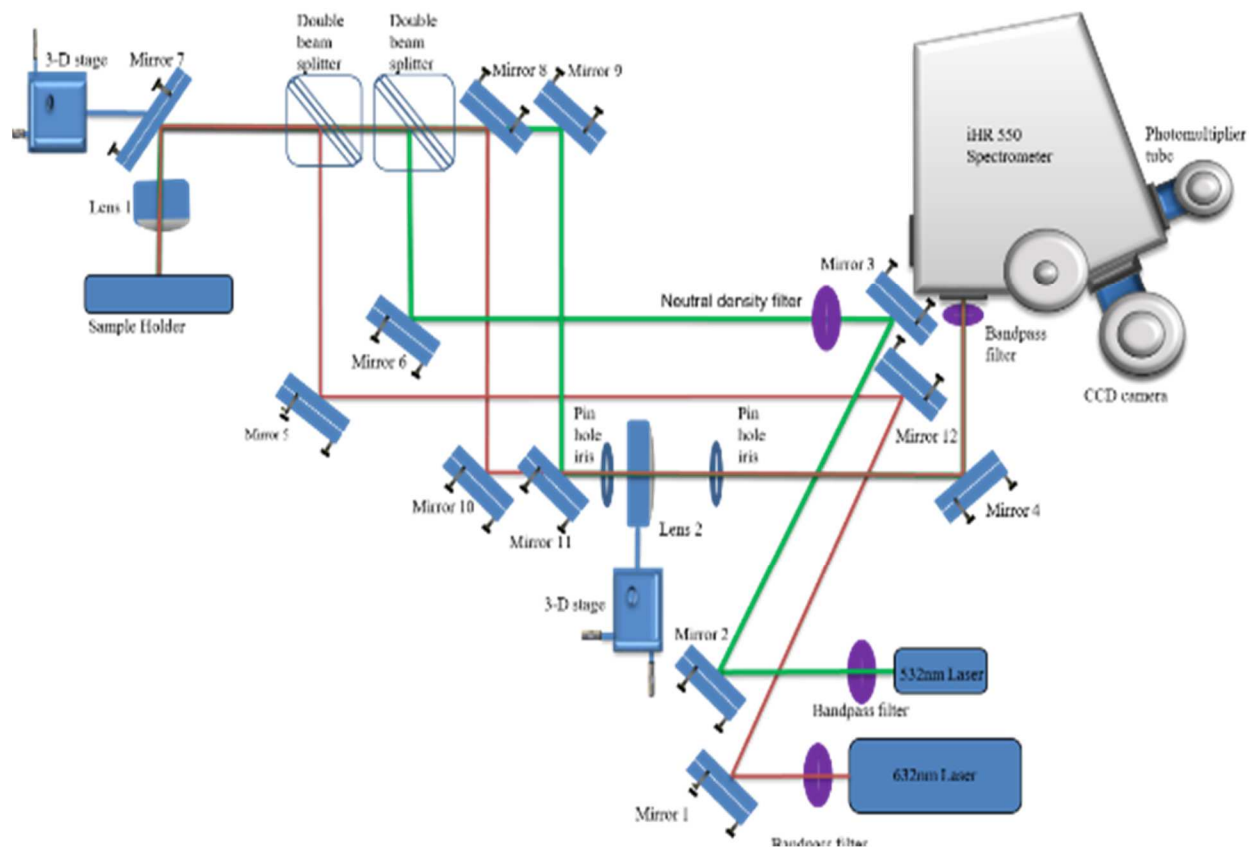


Figure 3.1: Schematic of Raman spectroscopy setup.

### 3.4 Photoluminescence

The third characterization used on the grown films was photoluminescence.

Photoluminescence is a characterization technique that, as the term suggests, uses the emission of light from a sample while using a light source for a provider of energy. The process, in general, is that photons of light from the source, that have energy above the band gap energy of the material, are absorbed in the sample. These absorbed photons interact with electrons in the sample and excite them to a higher energy state. This excitation of the electrons creates an electron-hole pair, or exciton. Radiative recombination of the exciton generates the release of a photon that has an energy that is equal to the band gap energy of the material. The emitted photons are collected and measured using a spectrometer. This characterization provides information on the band gap, recombination process, carrier lifetimes and more information on the sample being studied [6]. For this research, an in-house built PL setup was used for room temperature measurements (Figure 3.2). The set-up was designed to be multifunctional with 6

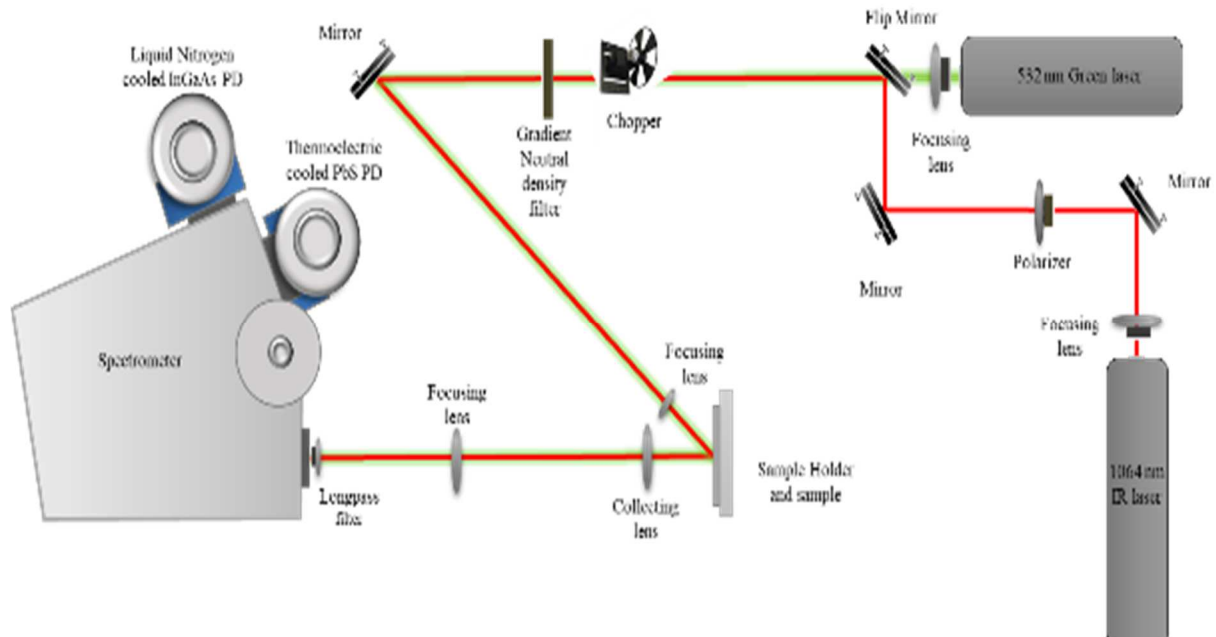


Figure 3.2: Schematic of photoluminescence setup

laser sources and different detectors, to provide a wide range of wavelength coverage, such as PbS, InSb, and InGaAs. The set-up was capable of off-axis PL, microPL and optical pumping at both low temperature and room temperature using separate collection paths. The lasers that were available were a 532 nm continuous wave (cw), a 1064 nm cw, 2000 nm cw, 1550 nm cw, 780 nm pulse Ti-sapphire, Nd: YAG, and a fempto second laser. A Horiba IHR 320 grating-based spectrometer along with a detector, either PbS or InSb, was used for the detection of the emitted light. Samples for this research were measured in the off-axis configuration using only the 532 nm, 1550 nm, and the 1064 nm lasers. The PbS detector was primarily used for the characterization as the wavelength coverage cut-off of 3.0  $\mu\text{m}$  was longer than the emitted wavelength for most of the samples.

### 3.5 X-ray diffraction

The x-ray diffraction (XRD) characterization technique is used to show the atomic structure of a crystalline material. Using the reflections of x- ray intensity in relation to the angles of omega and/or 2-theta, the crystal structure can be determined (Figure 3.3). The angle between the incident x-ray and the surface of the sample for these measurements is the incident angle, omega. The angle between the extended incident beam and the detector angle is the diffracted angle, 2theta. When x-rays are incident to the crystal of a material whose atoms are in a periodic order, electrons will be scattered from the atoms as periodic electromagnetic waves. These waves form an interference pattern which can be detected in terms of intensity at a specific angle. When the function of scanned intensity versus the scanned angles is plotted the resulting plot is called a rocking curve. From the rocking curve, the material quality can be inferred, and lattice constant calculations can be made.

X-ray diffraction is a non-destructive technique that uses x-rays to determine the

arrangement of atoms in crystal materials. The diffraction of the x-rays interacting with a material was determined by the ordered arrangement of the atoms in the material was first shown by William Lawrence Bragg and William Henry Bragg, [7]. Therefore, using this spacing they were able to determine the atomic arrangement of many materials. This technique has become one of the dominant methods for the characterization of the atomic structure of a material. For this research, a Panalytical X'Pert Materials Research Diffractometer (Malvern, UK [www.malvernpanalytical.com](http://www.malvernpanalytical.com)) that had an incident Cu  $K_{\alpha 1}$  beam with a wavelength value of 1.5406 Å was used.

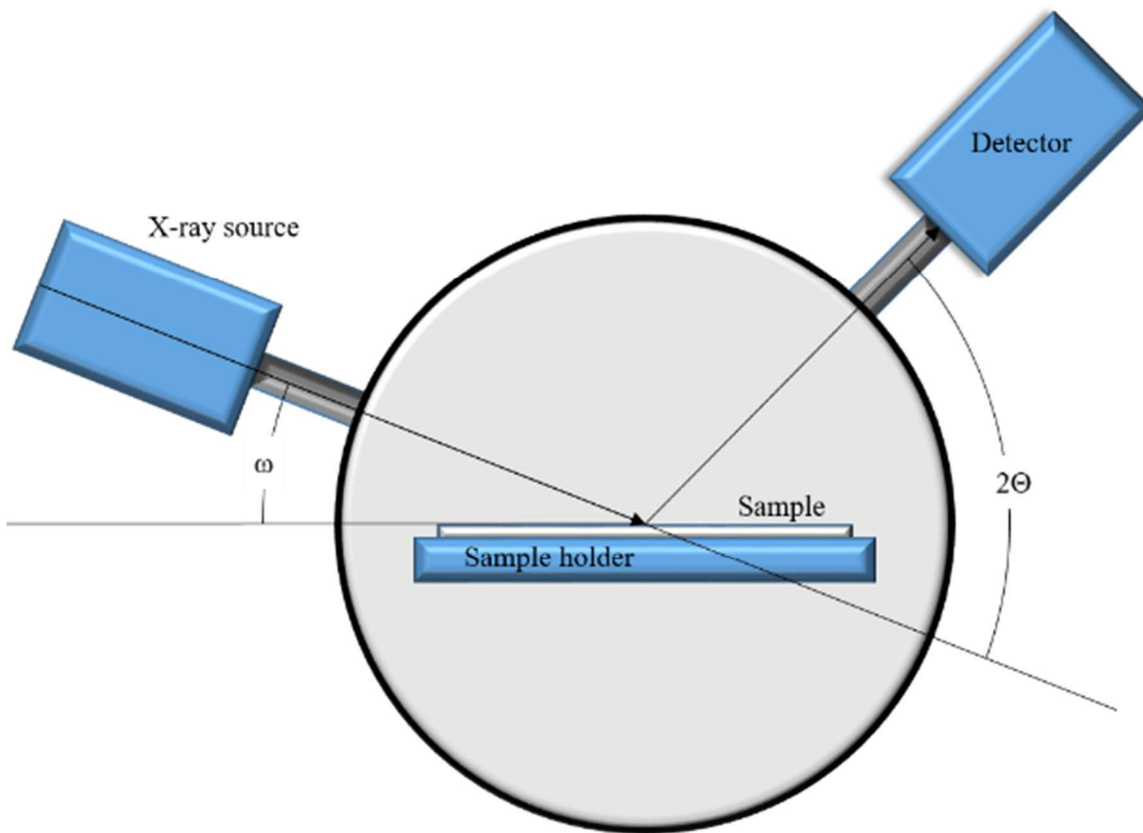


Figure 3.3. Schematic of XRD setup.

### 3.6 Description of documentation procedures

Maintaining proper documentation is critical for any successful laboratory, project,

business, or venture. The ability to receive information rapidly from a specific event for confirmation of data or to look for new trends that were not noticed before can mean the difference in success or failure. For this work, the ability to quickly obtain information from the results of a growth in less than one day provided the ability to adjust recipes for growths and allowed research towards goals to progress in a more efficient manner. To accomplish this, a procedure was established to grow a sample, have it characterized visually and optically, and have those results documented and back to the growth personnel in the same day. The procedure had three main parts: the growth, characterization, and documentation. This section will focus on the documentation procedures.

The documentation procedures consisted of the documents and how they were handled. The documents started with the growth documents. The first of the growth documents was the growth traveler which provided information on the general procedures on the machine operation and was a record of the recipe used for the growth. The growth traveler had to be signed by two individuals as part of a two-man rule that ensured that at no time a single individual was alone in the lab while the machine was in operation (Figure 3.4). The individuals that were required to be in the lab during the growth were the grower and the growth buddy. They had different responsibilities that will be discussed in the next section. The growth documents were the responsibility of the grower to complete. The major growth documents that were required for this research were the growth traveler, mentioned above, the sample cross section, and a sample wafer map. The sample cross section document was designed to contain a general description of the sample to be grown that includes the designed thickness of each epitaxial layer, the relation between the layers, the recipe for that layer, the substrate (material, orientation, and doping type), and the sample identifying nomenclature. The sample wafer map contained an oriented

0508-UF

CHECKLIST	LOCATION	ACTION										
Gas Reactor Column (GRC)	GRC Front	<input checked="" type="checkbox"/> All LEDs are green (Yes/No) ... 2.5 <input checked="" type="checkbox"/> Upper Heater Temperature (C) ... 567 <input checked="" type="checkbox"/> Nitrogen Inlet Regulator Pressure (psi) ... 25 <input checked="" type="checkbox"/> Nitrogen Inlet GRC (psi) ... 54 <input checked="" type="checkbox"/> Inlet Pressure Reading (mbr) ... 4 <input checked="" type="checkbox"/> Lower Heater Temperature (C) ... 500 <input checked="" type="checkbox"/> Nitrogen Purge Flow (LPM) ... 1.8										
Exhaust Temperature actively	Chase	<input checked="" type="checkbox"/> Channel 1 (C) ... 31.8 <input checked="" type="checkbox"/> Active cooling (C) ... 20 <input checked="" type="checkbox"/> Regulator on QDP 40 (psi) ... 12										
Chiller	Chase	<input checked="" type="checkbox"/> Water Level Visible <input checked="" type="checkbox"/> Nitrogen Purge Regulator Pressure (psi) ... 40										
QDP 40 Mechanical Pump	Chase	<input checked="" type="checkbox"/> Total Purge Flow (slm) ... 50 <input checked="" type="checkbox"/> GRC Exhaust (in. of water) ... 20 <input checked="" type="checkbox"/> Outside Cabinet Exhaust (in. of water) ... 0.65 <input checked="" type="checkbox"/> Regulating needle valve set value										
Exhaust Extraction System	Wall behind GRC	<input checked="" type="checkbox"/> Mass Flow Controller Exhaust (in. of water) ... 0.75										
Flow Controller	Flow Controller	<input checked="" type="checkbox"/> Purge Nitrogen inlet pressure (10 psi) ... 9 <input checked="" type="checkbox"/> Base Pressure of Process Chamber (Torr) ... 2.4 x 10 <sup>-8</sup> <input checked="" type="checkbox"/> Base Pressure of Load Lock Chamber (mbar) ... 3.6 x 10 <sup>-8</sup>										
Corrosive Resistant Turbo Pump	Chase											
Base Pressure	Pressure Controller Int											
Gas Alarms	Gas Sniffers	<table border="1"> <thead> <tr> <th>Inside Lab</th> <th>Outside Lab</th> </tr> </thead> <tbody> <tr> <td>Hydrogen, Methane (% LEL) ... 0</td> <td>Hydrogen, Methane (% LEL) ... 0</td> </tr> <tr> <td>Germane, Silane (PPB) ... 0</td> <td>Germane - Farm (PPB) ... 0</td> </tr> <tr> <td></td> <td>Silane - Farm (PPM) ... 0</td> </tr> <tr> <td></td> <td>Germane, Silane - Chase (PPB) ... 0</td> </tr> </tbody> </table>	Inside Lab	Outside Lab	Hydrogen, Methane (% LEL) ... 0	Hydrogen, Methane (% LEL) ... 0	Germane, Silane (PPB) ... 0	Germane - Farm (PPB) ... 0		Silane - Farm (PPM) ... 0		Germane, Silane - Chase (PPB) ... 0
Inside Lab	Outside Lab											
Hydrogen, Methane (% LEL) ... 0	Hydrogen, Methane (% LEL) ... 0											
Germane, Silane (PPB) ... 0	Germane - Farm (PPB) ... 0											
	Silane - Farm (PPM) ... 0											
	Germane, Silane - Chase (PPB) ... 0											
Gas Cylinders	in Fume Hood Cab	<input checked="" type="checkbox"/> Process Ar Bottle Inlet Pressure (psi) ( greater than 500 psi) ... 1600 <input checked="" type="checkbox"/> Process Ar Bottle Outlet Pressure (psi) ... 15 <input checked="" type="checkbox"/> Vent Ar Bottle Inlet Pressure (psi) ( greater than 500 psi) ... 700 <input checked="" type="checkbox"/> Vent Ar Bottle Outlet Pressure (psi) ... 15										
Gas Used	Gas Used	Operator Signature: <i>Perry C. Lee</i> Partner Signature: <i>[Signature]</i> Date: 24 Jul 2017										
	1 GE H <sub>2</sub>											
	2 AR											
	3											
	4											
	5											
	6											
	7											

Page 1

Date of Template Revision 07/19/2016  
Date Modified for Custom Experiment 10/17/2016

UHV-CVD Lab Rm 4505 Template RevB

Figure 3.4: Image of growth traveler first page showing system required checks and signatures.

diagram of the sample and was used to identify sections of the sample as they were removed for testing that could not be done on the sample as a whole piece. This document contained a record of the piece that was missing, its original location on the sample wafer, and who removed it from the wafer. These documents were placed in binders for hard copy records of each growth ordered by specific document type and sample identifier (Figure 3.5).

The characterization documents were used to document the individual characterizations that were performed on a sample. These documents had individual templates for each measurement. They contained the sample identifier, the date of characterization, the individual performing the characterization, and the conditions that the characterization was performed under. Templates were created for the ellipsometry, Raman spectroscopy, photoluminescence, and x-ray diffraction measurements. The documents were created after each characterization was performed by the individual performing the characterization. The completed documents

were printed and bound to be maintained for hard copy records as noted above in (Figure 3.5). All of the documents were stored as soft copies on a SharePoint site to be made available to any member of the research team at any time for use or discussion of results.



Figure 3.5: Image of documentation binders for hardcopy records of all documents pertaining to each sample.

### 3.7 Description of typical growth day

The typical growth day consisting of the growth and characterization of three samples started with a discussion of the last growth of the previous day while growth pre-checks were being performed. These checks started with checking the gas reactor column followed by the chamber purge gas regulators. These checks were to ensure that the gas reactor column was in a condition that would allow for the harmful byproducts of the process gas reaction to be rendered harmless by converting them into salts at high temperature (above 550 °C) with a catalyst. The checks continued to the process chamber base pressures and secondary containment condition.

The last checks inside the lab were to ensure the status of the toxic gas detection system for all active channels. The checks were continued in the chase to verify backing pump and the associated chiller condition. The final checks in the laboratory chase were to verify the pressure setting on all of the outside supplied nitrogen gas regulators. Following all of the checks, the decision was made on the first growth recipe for the day. This decision was based off of the results of the second growth from the previous day.

During the UHV-CVD machine pre-checks, members of the growth team would perform the pre-checks and start the individual characterization tools so that they would be in a ready condition. The last growth from the previous day was collected by members of the growth team to be characterized, while the grower and buddy were performing the growth of the first daily samples.

At that time the recipe was finalized and the prepared sample substrate that was preloaded into the process chamber the previous day was placed on to heat by setting the desired growth temperature and allowing the substrate to come to temperature at a slow ramp rate of < 40 °C/min to avoid major overshoot of the temperature and to reduce thermal shock. Once the desired temperature was reached, the substrate was allowed to heat soak for 20 min to reduce temperature gradients across the wafer surface as the sample cradle acted like a heatsink to remove heat from the edges of the wafer. Following the heat soak, the growth recipe was followed using the procedures in the previously discussed growth traveler. The process chamber was purged of all gases following the growth process. This purge was completed using the carrier gas for the sample growth by increasing the pressure in the process chamber to above 750 mTorr and then pumping the chamber down to a pressure level of  $10^{-5}$  Torr multiple times. This was to ensure that no process gases remained in the chamber before the sample was removed



from the chamber and transferred to the load lock chamber. The sample was allowed to cool to a temperature below 150 °C before it was then transferred to the load lock chamber. Following transfer to the load lock, the sample was removed from the machine by bringing the load lock chamber to atmospheric pressure by inflating the chamber pressure with non-reactive purge gas with the load lock door unlatched.

The sample was removed from the chamber and the next prepared substrate was loaded

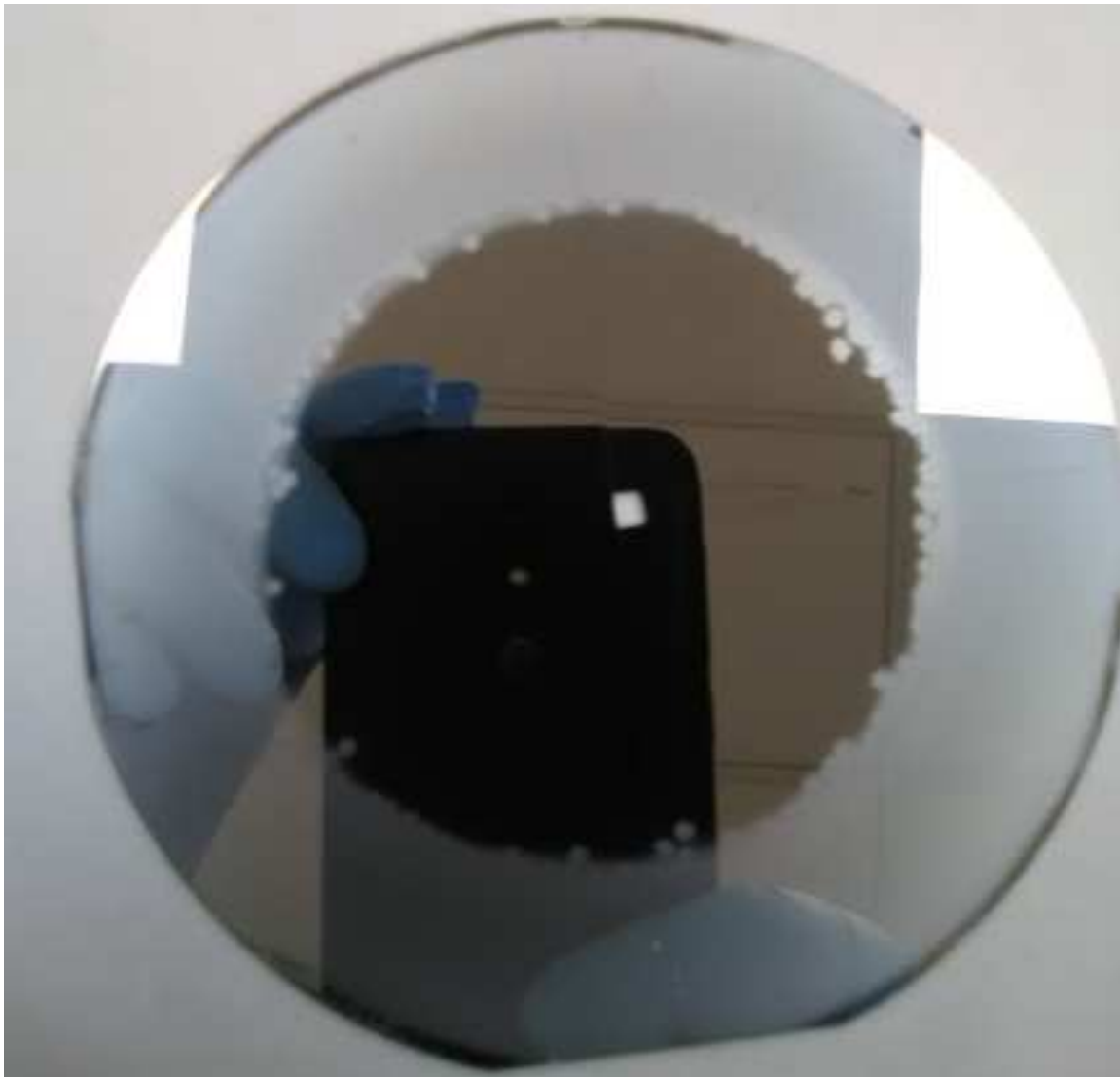


Figure 3.6: Typical image of a sample after removing from load lock prior to initial characterization.

on to the transfer arm to be transferred to the process chamber. The load lock was placed in a pump down condition to reach a pressure  $\sim 10^{-7}$  Torr before moving the sample onto the growth process chamber sample cradle. A visual inspection of the sample was performed after removing it from the UHV-CVD machine and photos of the sample were taken for documentation purposes and uploaded to the SharePoint site (Figure 3.6). The visual inspection was to determine the success or failure of the growth, and the initial description of the growth was noted on the growth traveler.

The sample was then taken by the member that is scheduled to go to the ellipsometry characterization tool for the initial characterization work. The individual that was operating the ellipsometry tooling notified the team member that was running the photoluminescence and Raman tooling that the first growth was completed, and that the individual was needed in the growth lab for the second growth of the day. The individual that brought the sample to ellipsometry was responsible for performing the characterization. The data from ellipsometry was collected and fit using models in the software from J.A. Woollam. The data collected included information on the individual layer thicknesses and was used to calculate the growth rate of each layer. The data that was fit to the model was used to find the absorption coefficients of the targeted layer as a function of wavelength. This data was saved and transferred to the template using Origin Labs's (Northampton, Ma [www.originlab.com](http://www.originlab.com)) Origin software (Figure 3.7). The documents from the ellipsometry characterization were printed for the hardcopy records and uploaded to the SharePoint site. The individual in the lab with the photoluminescence and Raman tooling finished the remaining characterizations on the previous days last sample and ensured that the documents were printed for hard copy records and uploaded to the SharePoint site.

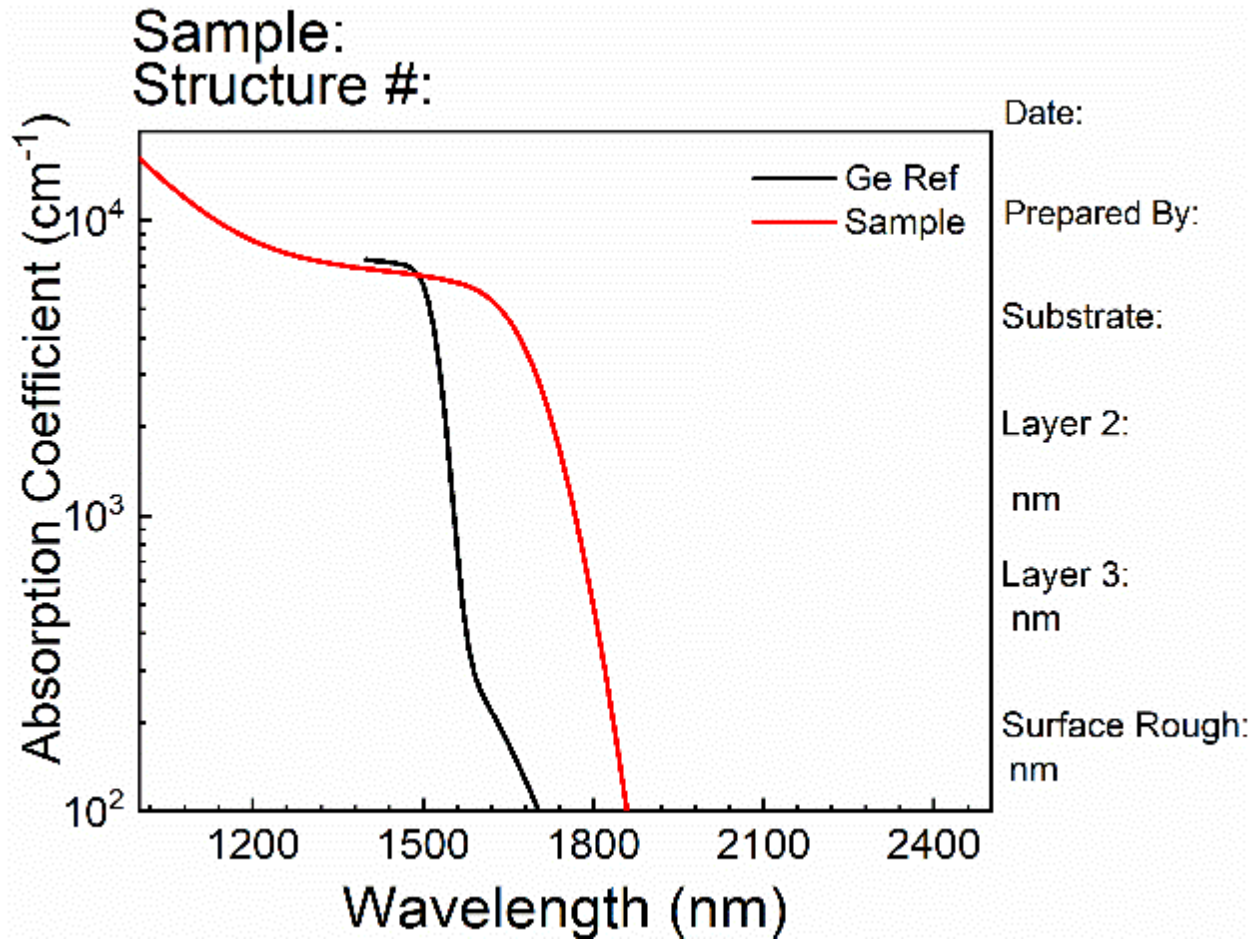


Figure 3.7: Template for ellipsometry measurements to be used during the initial characterization of samples.

When the ellipsometry characterization of the sample was finished, the sample was taken to the Raman spectroscopy tool and the characterization was performed by the individual that had been at the ellipsometry station. The Raman characterization was performed by first ensuring the alignment of the system using the standard operating procedures developed for the system. The system's operating software was then checked to ensure that operating parameters for the characterizations were properly set. The first measurement of the characterization set was a calibration measurement of a reference sample of bulk substrate, primarily Ge, that was determined based on the desired composition of the sample to be measured. The data from each measurement was saved on the computer containing the operating software using the sample

identification as the primary folder and the measurement description as the filename of a .csv file type. Following the calibration measurement, measurements were made of the sample at three locations along the sample surface. The measurement locations were the sample center, a point approximately  $\frac{1}{2}$  the radius of the sample, and a point  $\sim 10$  mm from the sample edge. The measurement locations allowed for the comparison of the sample for growth uniformity based on how much refocusing needed to be done to the objective lens between measurements, the difference in peak intensity of the measurements, and the difference in peak wavelength position of the measurement. Once all of the measurements were taken and the data saved, the data was copied to a flash drive to be processed using the individual's laptop before placing the processed data into the template for the Raman measurements (Figure 3.8).

The data for the calibration sample was extracted into an Excel spreadsheet for the purpose converting the plot intensity as a function of wavelength to a plot of wavenumber versus intensity by using Equation 3.1.

$$n = ((1/\lambda_1) - (1/\lambda_2)) * 10^7 \quad (\text{Equation 3.1})$$

where  $n$  is the wavenumber in  $\text{cm}^{-1}$ ,  $\lambda_1$  is the wavelength of the incident laser source in nm, and  $\lambda_2$  is the wavelength output from the spectrometer for each intensity measured in nm. The peak position of the calibration sample was linearly shifted by the amount required to ensure the peak position was maximized at  $300 \text{ cm}^{-1}$  to eliminate day-to-day variations in the measurement setup. This corrected data from the Excel template was transferred to the Raman template in Origin and the intensity data for the sample measurements were then transferred to the template in the Origin software and the template was completed by the individual that performed the characterization. This completed document was printed for binding in the hardcopy records as well as uploaded to the SharePoint site.

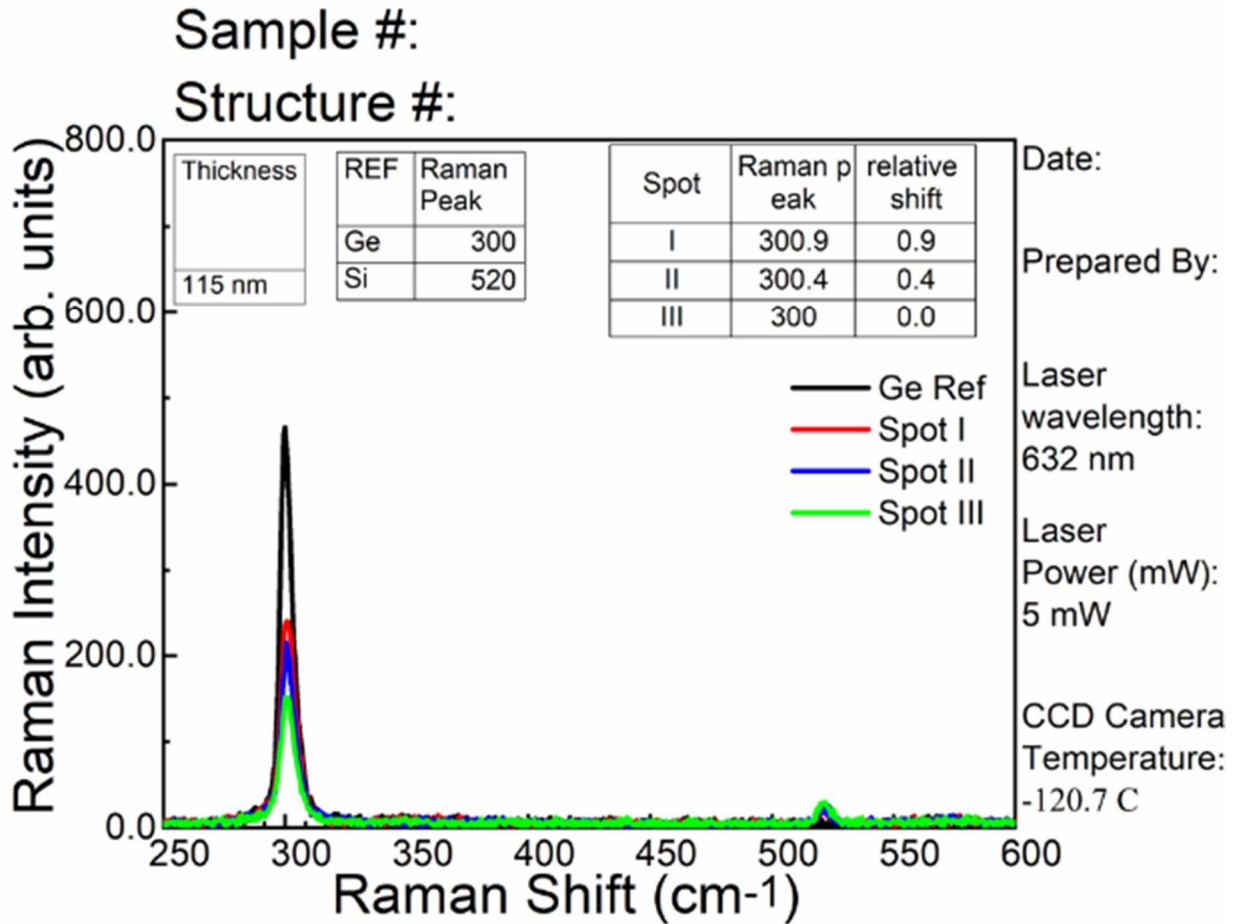


Figure 3.8: Typical Raman template with data from measurement and reference showing a plot of the intensity as a function of Raman shift wavenumber using Equation 3.1.

The photoluminescence measurement was performed on the sample following the completion of the other measurements. This characterization started with the reference sample of bulk substrate, typically Ge, for a comparison of the peak intensity with the measurements taken from the sample to be characterized. This data was collected as an intensity versus wavelength plot using the same locations on the sample to be characterized and saved in an Origin work book as the photoluminescence spectrometer is operated using the supplied Origin software to control the experiment. This data was saved to a flash drive as well as the tool's computer. The flash drive was used to transfer the data to the individual's computer for fitting

into the Origin template for photoluminescence (Figure 3.9). The completed photoluminescence characterization document was uploaded to the SharePoint site and printed for the hardcopy records.

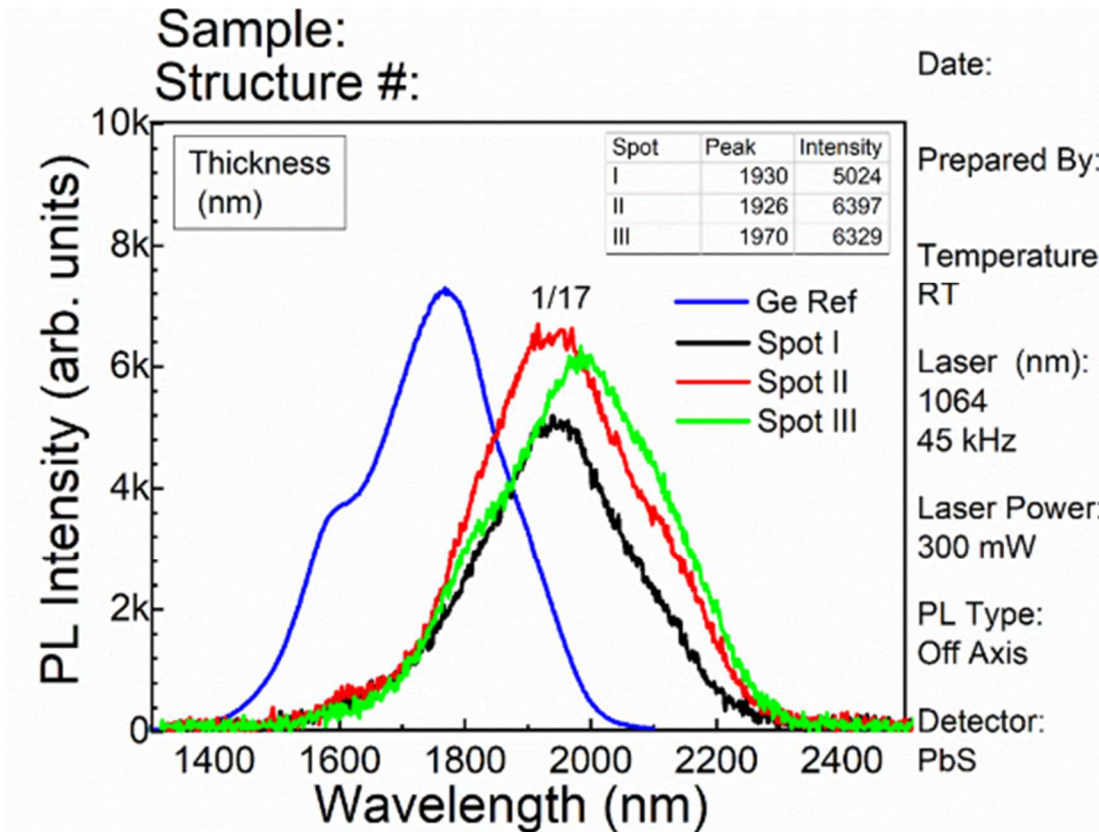


Figure 3.9: Typical photoluminescence template showing measurement and reference data plots.

Following the completion of the three initial characterizations, the sample was returned to the UHV-CVD growth lab and placed in sample storage.. The results for the initial characterizations were brought to the growth lab and discussed with the growth team members who were finishing the second growth of the day (which had its recipe based on the last growth of the previous day), so as to prepare for the third growth of the day using the results from the first. This near same day turnaround for characterization data allowed for the efficient adaptation of needed changes to rapidly progress toward the objectives of the long term growth

plan. The characterization process of running one sample through the characterizations while the next sample was growing ensured that at no point was the characterization more than one sample behind the growth. When the final growth of the day was finished and all of the day's characterizations had been completed, printed, and uploaded, the documents were distributed to the binder groups in each of the characterization labs. The final task of the day was the responsibility of the growth team leader. This task was the distribution of a daily growth summary that contained a spreadsheet of the day's growth recipes and characterization results and a brief description of the growth's purpose, success or failure, and any issues that may have occurred during that day with the equipment. The efficient use of the obtained characterization data and equipment reports allowed the research to progress rapidly and plan for possible issues with equipment.

## Chapter 4 UHV-CVD Growth Development of Ge Buffer on Si

### 4.1 Introduction

The growth of GeSn on silicon substrates has given the field of silicon photonics a material system that has the potential for complementary metal oxide semiconductor (CMOS) compatibility and with a means to tune the material's band gap to improve device performance. These can be high performance devices such as lasers, light emitting diodes, and photodetectors. The GeSn material system incorporated to the silicon platform has shown high commercialization value as indicated by the high rates of success of photonic devices in recent years[8][9][10].

The growth of this material system on silicon is not without issues. The most significant issues are the large lattice mismatch between GeSn and Si which is larger than 4.2% along with a low solubility of Sn in Ge which is smaller than 0.5%. Another issue is the crystal stability of Sn that changes from a diamond cubic structure ( $\alpha$ -tin) to body centered tetragonal ( $\beta$ -tin). This  $\alpha$ - $\beta$  transition typically occurs around a nominal temperature of 13.2 °C. Due to these issues, multiple techniques have been developed to perform the growths of GeSn under non-equilibrium conditions such as chemical vapor deposition (CVD) and molecular beam epitaxy (MBE). The growth of GeSn by CVD has been studied by many groups for more than a decade [11][12][13][14][15]. During these investigations, different precursors were used for both Ge and Sn. The most recent Sn precursors used for CVD growth have been stannane ( $\text{SnD}_4$ ) and stannic chloride ( $\text{SnCl}_4$ ), with commercially available  $\text{SnCl}_4$  being the lower cost and more stable of the two. The precursors for Ge have varied as well from high order hydrides such as digermane ( $\text{Ge}_2\text{H}_6$ ) and trigermane ( $\text{Ge}_3\text{H}_8$ ) to the low cost germane ( $\text{GeH}_4$ ). In this section, the growth of the silicon-germanium-tin (SiGeSn) material system will be discussed.



## 4.2 Growth matrix that led to buffer recipe

The lattice mismatch between GeSn and Si causes compressive strain that increases as the amount of Sn incorporation increases. This induced strain results in poor crystal quality and reduces amounts of Sn in the grown films. To reduce this strain, high quality Ge buffers have been grown on Si substrates. The growth of high-quality Ge on Si has been studied using three primary methods. The two main methods used have been: (i) using a graded SiGe buffer [16][17], and (ii) using a two-step buffer with an annealing step [18][19][20]. The third method used is aspect ratio trapping, where a pattern of windows whose depth to width ratio is  $>1$  is formed in a silicon dioxide layer that is deposited on the substrate and the threading dislocations are trapped in the patterned area. The issue with this method comes from the dislocations that form on the surface when the lateral overgrowth from each patterned window merges. The graded SiGe buffer layer uses a multiple layer film growth technique that increases from low Ge composition SiGe to only Ge in the final layer. This buffer growth method has produced buffer layers that have a threading dislocation density (TDD) in the range of  $10^6 \text{ cm}^{-2}$ [21]. The primary issue with this method is that the buffer layers typically average several micrometers in thickness. The two-step growth method uses a low temperature first step, that promotes two-dimensional growth, and a high temperature second step followed by an anneal. This technique has been shown to produce high quality Ge films with TDD in the range of mid  $10^6 \text{ cm}^{-2}$  with buffer thicknesses in the range of  $1 \text{ }\mu\text{m}$ [22]. The growths for this study used the two-step method without an anneal step due to technical issues with the equipment.

The Ge buffer that was developed used a LT/HT growth method that produced films that were suitable to be the foundation for the growth of GeSn. The process started with the growth of high temperature Ge directly on Si. These growths were done to find a starting point for the

low temperature step using a fixed growth pressure of 1 Torr. This step involved varying the temperature, from 300 °C to 400 °C, and the GeH<sub>4</sub> mass flow rates to provide a growth rate that prevented island formation and promoted two-dimensional growth (Table 4.1).

Table 4.1: Low temperature growth matrix for early stage development of Ge buffer layer.

Ge First Step			
GeH <sub>4</sub> : 10 sccm; Ar: 25 sccm; time 60 min			
Temp \ Press	0.1 torr	0.5 torr	1 torr
330 °C			
350 °C			
370 °C			

These growths were examined using ellipsometry and Raman spectroscopy. The ellipsometry measurements were used to determine film thickness (Figure 4.1a). Raman spectroscopy measurements were used to determine the wave number difference between the as-grown film and bulk Ge wafer and as a confirmation of film thickness from pumping laser penetration depth (Figure 4.1b). The second set of growths were used to determine the temperature that provided the best growth rate and film quality to produce a high-quality Ge buffer layer. These growths used the same growth pressure of 1 Torr as the low temperature step. The temperatures and GeH<sub>4</sub> flow rates were again varied to find the best combination to produce possible results without using an annealing step (Table 4.2). These samples were measured using ellipsometry and Raman spectroscopy to determine the starting point for the full LT/HT buffer growth conditions. The grown films were measured using ellipsometry, Raman

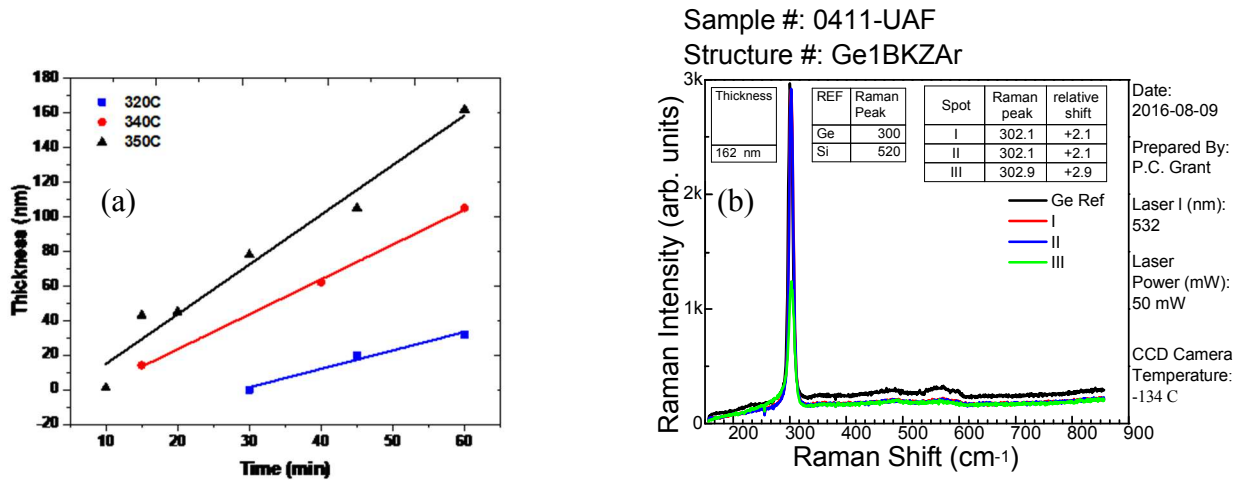


Figure 4.1: (a) Plot to determine growth rates at varying deposition temperatures based on ellipsometry thickness measurements and, (b) a typical Raman spectroscopy plot.

spectroscopy, and photoluminescence (PL). The growth conditions for the full buffer were determined through an optimization of the first and second step by varying the flow rates of the second step and the temperatures for both steps to achieve the best quality using the PL results for comparison with the highest intensities being the determining factor for further

Table 4.2 High temperature growth matrix for early stage development of Ge buffer layer.

Ge Second Step				
GeH4: 10 sccm; Ar: 25 sccm; time 20 min				
Press	0.1 Torr	0.5 Torr	1 Torr	
Temp				
550 °C				
600 °C				
650 °C				

characterization (Figure 4.2). The results of the measurements were compared to reference samples of a bulk Ge wafer to provide a standard by which film quality could be compared to

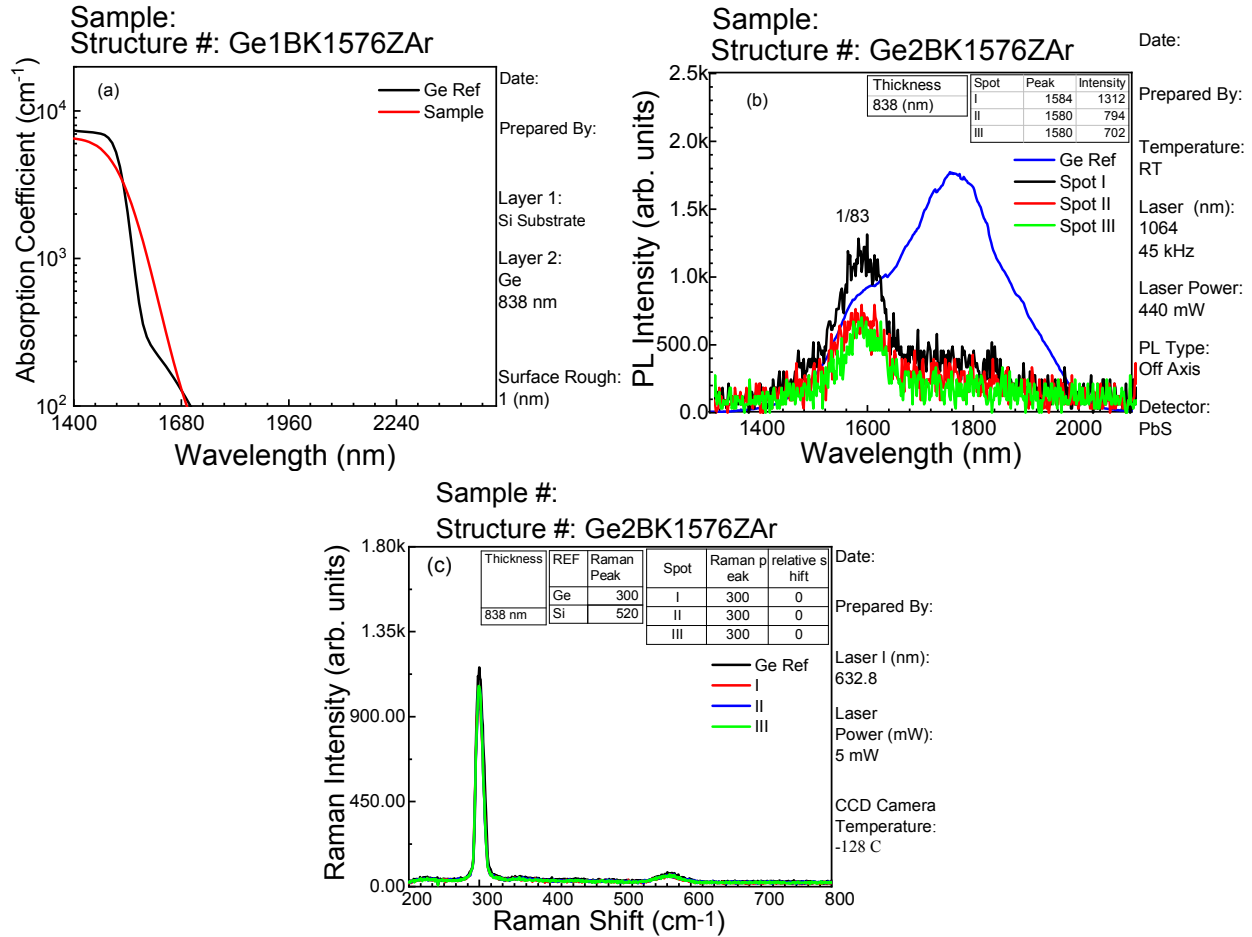


Figure 4.2: Typical results from samples used for LT/HT Ge buffer layers from (a) ellipsometry measurements, (b) photoluminescence measurements, and (c) Raman measurements.

earlier growth initial characterizations to identify samples warranting further characterization by transmission electron microscopy (TEM). Etch pit density would be performed to determine TDD of the films. The samples for development of the Ge buffer were grown using 4-inch p-type Si (001) wafers. The wafers were prepared using a standard piranha etch (a solution of H<sub>2</sub>SO<sub>4</sub> and H<sub>2</sub>O<sub>2</sub> in a ratio of 1:1) followed by a HF passivation dip as reported in previous work by Mosleh, et al [23]. The film thickness measured from the ellipsometry data fitting was also

confirmed by TEM as shown in (Figure 4.3). The buffer recipe, once finalized, was highly repeatable as was determined through characterization of later grown samples discussed in

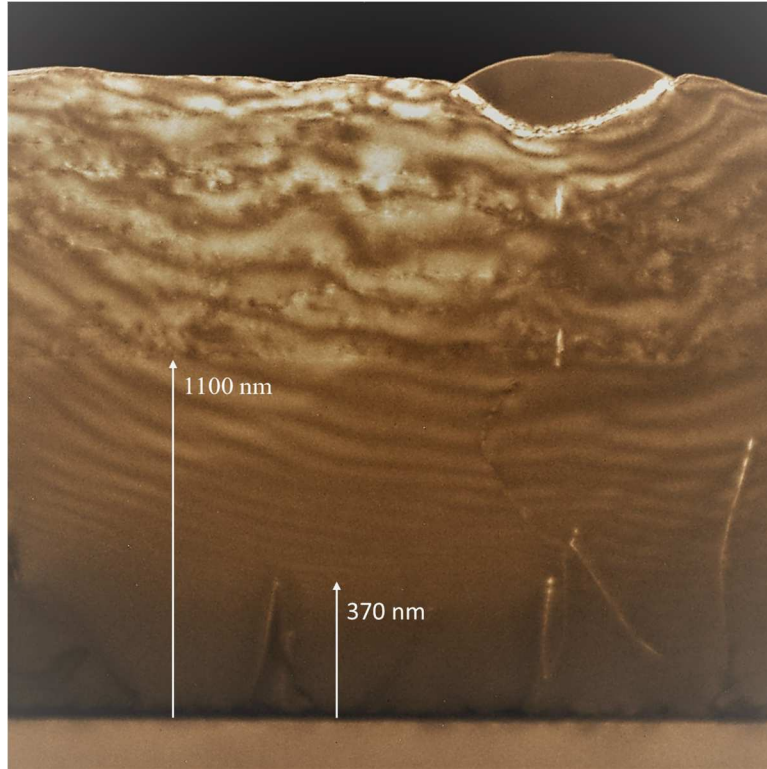


Figure 4.3: TEM image of GeSn sample showing Ge buffer.

Chapter 6 (Figure 6.6) and produced a buffer that had a first layer of  $\sim 350$  nm thickness followed by the second layer that gave a total film thickness of  $\sim 1$   $\mu\text{m}$ .

The PL of the grown films was the final determining factor as to which samples got further testing. The early growths of the buffer layer started with no PL response when compared to the bulk Ge reference (Figure 4.4). The final optimized buffer layer growth showed a PL response that showed a ratio of  $1/8$  when the direct band gap peaks were compared. This response measurement also showed a shifting to longer wave lengths as compared to the bulk reference that could be attributed to tensile strain in the buffer layer. This tensile strain occurred

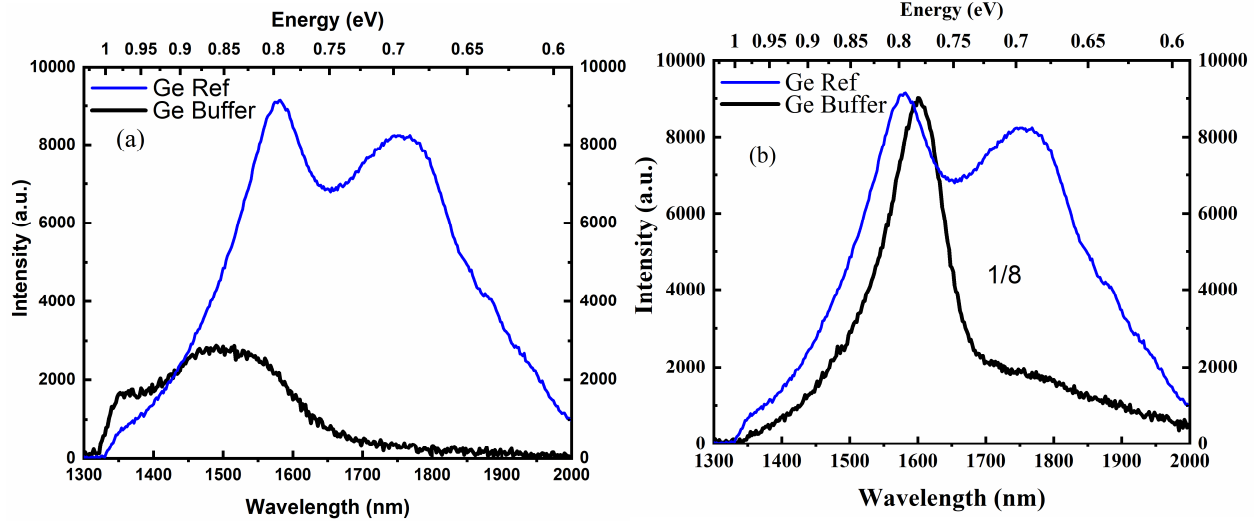


Figure 4.4: Photoluminescence plots of (a) initial and (b) final Ge buffer growths.

due to a difference in the thermal expansion coefficients between Si and Ge which are  $2.6 \times 10^{-6} \text{ cm } ^\circ\text{C}^{-1}$  and  $5.9 \times 10^{-6} \text{ cm } ^\circ\text{C}^{-1}$ , respectively. This caused the high temperature second step Ge layer to develop tensile strain as the sample cooled. The buffer samples producing the lowest reference to sample direct peak intensity ratio were chosen for the etch pit analysis where an iodine-based etchant was prepared by mixing 67 mL of acetic acid ( $\text{CH}_3\text{COOH}$ ), 20 mL of nitric acid ( $\text{HNO}_3$ ), 10 mL of hydrogen fluoride (HF), and 30 mg of iodine ( $\text{I}_2$ ) described by H.C.Luan, et al [20]. This etchant was applied to the sample then a SEM image was taken of the surface. This image showed pits in the surface where the etchant attacked the points where threading dislocations terminated at the surface. These pits were counted and a TDD was calculated (Figure 4.5). The results from these measurements showed that the optimized buffer had a TDD that was in the range of  $1 \times 10^7 \text{ cm}^{-2}$ . This measurement was within one order of magnitude of the range of high-quality optimized Ge buffer layers which have been reported in the range of  $\sim 10^5$  to  $10^6 \text{ cm}^{-2}$  and used a final annealing step to further reduce the TDD in the film [20]. The buffers were determined to be of sufficient quality that GeSn growth work onto the buffer layers could begin. Further improvements in the buffer layer may be possible using an annealing step

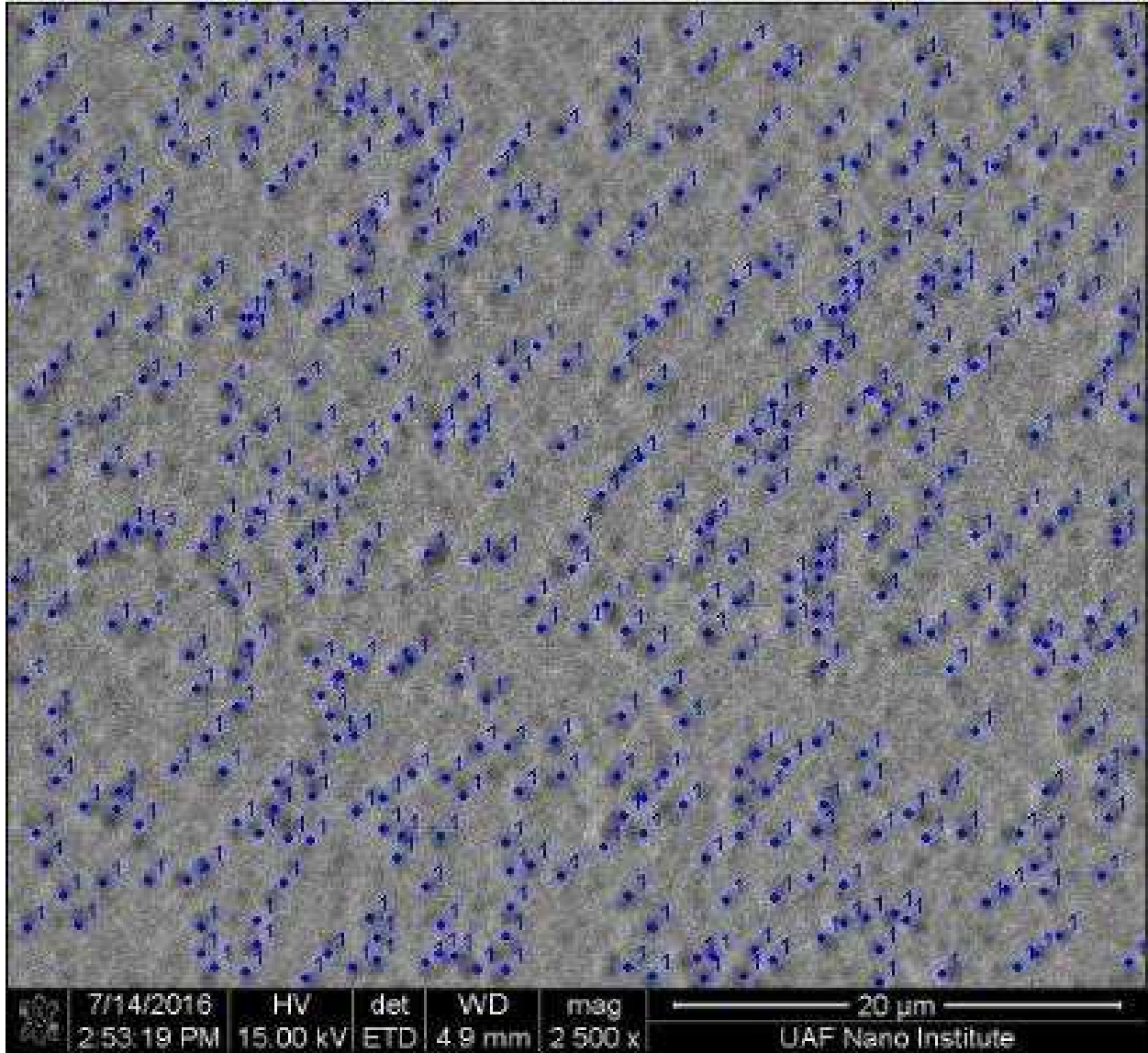


Figure 4.5: SEM image of etch pits showing a calculated TDD of  $1.1 \times 10^7 \text{ cm}^{-2}$ .

which was not possible during the buffer development due to limitations caused by technical issues with the substrate heater in the UHV-CVD chamber.

## **Chapter 5** Growth of SiGe on Si

### **5.1** Introduction

The materials grown for this study were produced in a custom built cold-walled Ultra High Vacuum Chemical Vapor Deposition (UHV-CVD) reactor with a base pressure of  $10^{-10}$  Torr. The substrates for those samples which were silicon were prepared using a standard piranha etch cleaning solution of  $\text{H}_2\text{SO}_4$  and  $\text{H}_2\text{O}_2$  at a ratio of 1:1 followed by a hydrofluoric acid (HF) passivation. When sapphire substrates were used, they were treated with a 1  $\mu\text{m}$  titanium coating on the backside of the wafers to aid in heating the wafer from the radiative heating in the process chamber due to the transparency of the sapphire substrates. The wafer surface was then prepared with methanol and dried with nitrogen prior to loading into the reactor load-lock. All films were grown as bulk material with no doping since the reactor did not have the capability to use dopants. After each growth cycle, the sample was removed from the reactor and the initial characterizations were performed. These characterizations of ellipsometry and Raman spectroscopy allowed for quick feedback so that recipe adjustments could be made to reduce the amount of time required to complete the matrix and advance toward the research goals.

### **5.2** Growth on Si (100)

The planning for this series of growths started with the formulation of a growth matrix. The matrix was determined using known working recipes for the growth of Ge buffers using the custom built cold walled Ultra High Vacuum Chemical Vapor Deposition (UHV-CVD) reactor. The matrix was broken into two divisions based on growth pressure. The first division was defined using a growth pressure of 0.1 Torr was used with the second division being 1.0 Torr. The pressure setting for these growths were determined from previous work done for



germanium growth on silicon and these pressures were found to provide the best starting point for low growth rate. Prior to growth, the substrates were cleaned using the above described wafer preparation and loaded in to the load lock of the ultra-high vacuum chemical vapor deposition chamber. The sample substrates in the load lock were kept at a base pressure of  $10^{-7}$  Torr to reduce native oxide formation. The substrates were then transferred individually to the process chamber of the chemical vapor deposition reactor where they were heated to growth temperature. The growth temperature was maintained for 20 minutes for a heat soak to ensure that the substrate was uniform in temperature to prevent thermal gradients due to the sample cradle acting as a heat sink. The temperature range for these growths was from 450 °C to 700 °C. The germanium precursor flow rates were set at 5 sccm for the growth pressure of 0.1 Torr. A flow rate of 10 sccm was used for growths at a pressure of 1.0 Torr. The flow rates for the silicon precursor varied between 1 sccm and 10 sccm for both growth pressures. The flow rates for the argon carrier gas was set at 200 sccm for the 0.1 Torr growth pressure and a flow rate of 25 sccm was chosen for the 1.0 Torr growth pressure. The length of time for all growths was fixed at 15 minutes. The growth matrices from these growths were used to develop the growth recipes for the later silicon-germanium growths on sapphire. The growth matrices for growths on silicon (100) are shown in Tables 5.1 and 5.2, respectively.

Table 5.1: The growth matrix for SiGe on Si (100) using low pressure (0.1 Torr).

Low Pressure SiGe Growth Matrix Si (100)		Grown samples shown		Precursor GeH <sub>4</sub> F.R. (sccm): 10					
Time	FR (sccm) of Carrier Gas (Ar)	Growth Pressure (Torr)	Temperature Precursor SiH <sub>4</sub> F.R. (sccm)	450	500	550	600	650	700
15	200	0.1	1						
			2.5	A1		D1			B1
			5			C1			
			10			E1			

Table 5.2.: The growth matrix for SiGe on Si (100) using high pressure (1.0 Torr).

High Pressure SiGe Growth Matrix Si (100)		Grown samples shown		Precursor GeH4 F.R. (sccm): 10						
Time	F.R. (sccm) of Carrier Gas (Ar)	Growth Pressure (Torr)	Precursor SiH4 F.R. (sccm)	Temperature						
				450	500	550	600	650	700	
15	25	1	1							
			2			E2				
			4	A2/F2	B2		D2			
			6							
			8			G2				
			10			C2				

### 5.2.1 Material characterization

The initial characterization of the grown samples was taken using ellipsometry and Raman spectroscopy. This characterization was used to determine which samples were to be further characterized using x-ray diffraction measurements. The ellipsometry results from these growths showed that under low pressure and high dilution of carrier gas, the growth rates of the films ranged from no film growth to a maximum of 11 nm/min. The absorption coefficients generated from the fitting of ellipsometry data showed that the absorption cutoff wavelength reduced as the percent incorporation of silicon increased in the samples. Typical results from the fitting of the ellipsometry data can be seen in Figure 5.1 where the silicon percentage was about

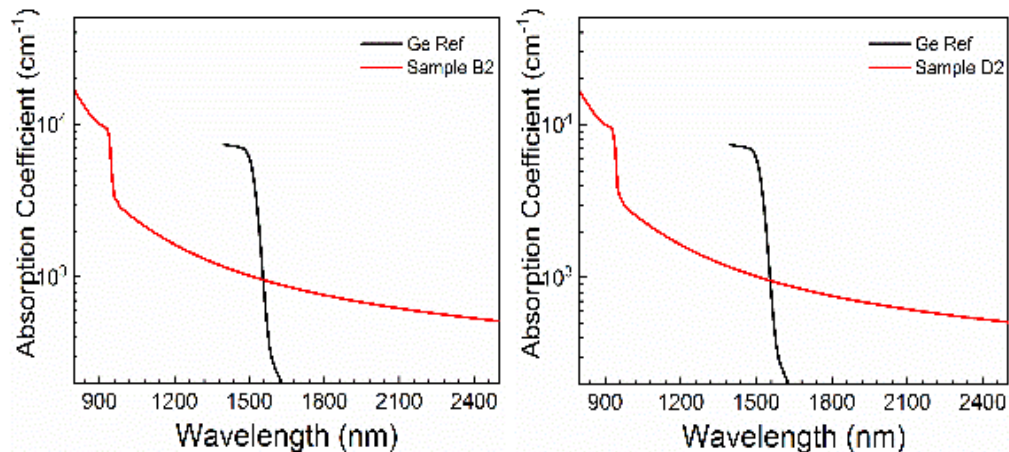


Figure 5.1: Ellipsometry results typical for two samples grown on Si (100) substrates.

18% and the cutoff was below 1000 nm. The samples showed a peak around 395  $\text{cm}^{-1}$  in the Raman spectroscopy measurements. Since the films that were grown were an alloy of both germanium and silicon, they had an expected critical thickness of less than 100 nm [24]. The assumption for relaxed layers was made for those sample grown on silicon due to thickness fittings from ellipsometry. The assumption of relaxation allowed for any shifting of the Raman wavenumber for the longitudinal optical (LO) phonons to be attributed to the incorporation of silicon in the grown films when compared to the germanium bulk samples (Figure 5.2).

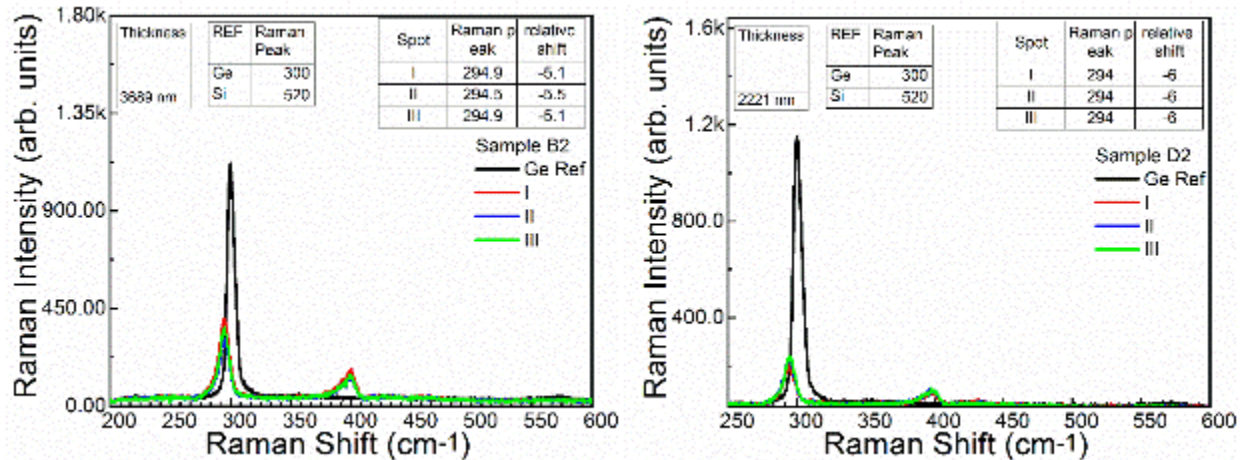


Figure 5.2: Typical Raman results for two SiGe growths on Si(100).

The XRD rocking curve measurements for the samples grown at lower pressure showed that the films were defective which was determined from the low intensity and the full width half maximum of the peaks. The incorporation of Si in the films varied with temperature and flow rate changes as shown in the shifting of the peak positions (Figure 5.3). With the increase in growth pressure and dilution, the quality of the grown films improved. This improvement of quality of the grown films was determined from the intensity gains and the narrowing of the FWHM of the XRD rocking curves of the measured samples (Figure 5.4). From the fitting of the peak positions, calculations were used to determine the d-spacing of the crystal structure of the

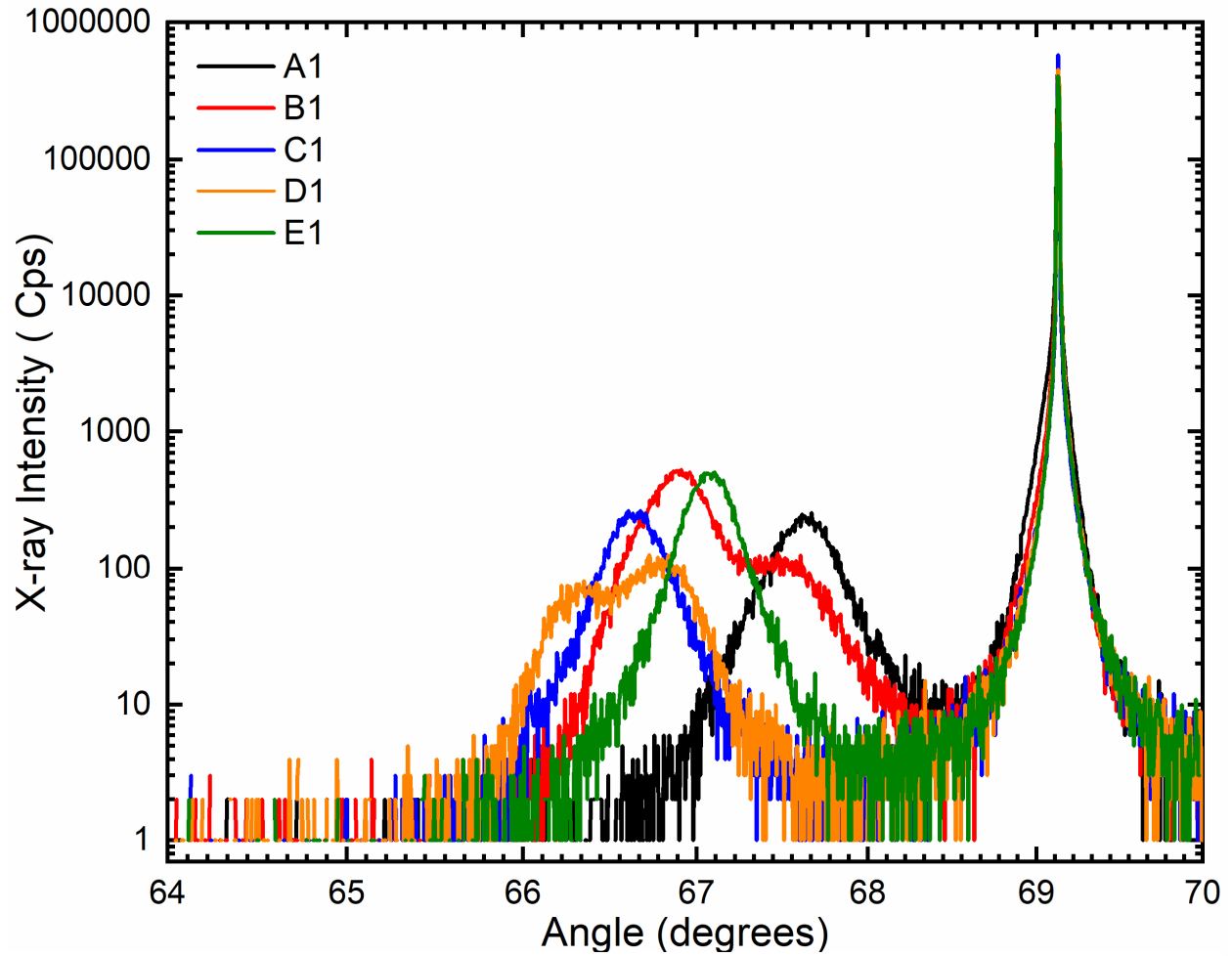


Figure 5.3: Combined plot of XRD rocking curve for SiGe (004) for growths on Si (100) performed at 0.1 Torr using recipes in Table 5.1.

films. From the d-spacing calculations the lattice size was calculated. Using the calculated lattice size, calculations were made to determine the percent of incorporation of silicon into the film using Vegard's law (Table 5.3). The calculations for the d-spacing were made using Bragg's law

$$d_{hkl} = 1.54 \text{ \AA} / 2 \sin \theta_{hkl} \quad (\text{Equation 5.1})$$

where  $d_{hkl}$  is the d-spacing and  $\theta_{hkl}$  the fitted peak angle for the  $2\theta$ -omega plot/2 (in radians).

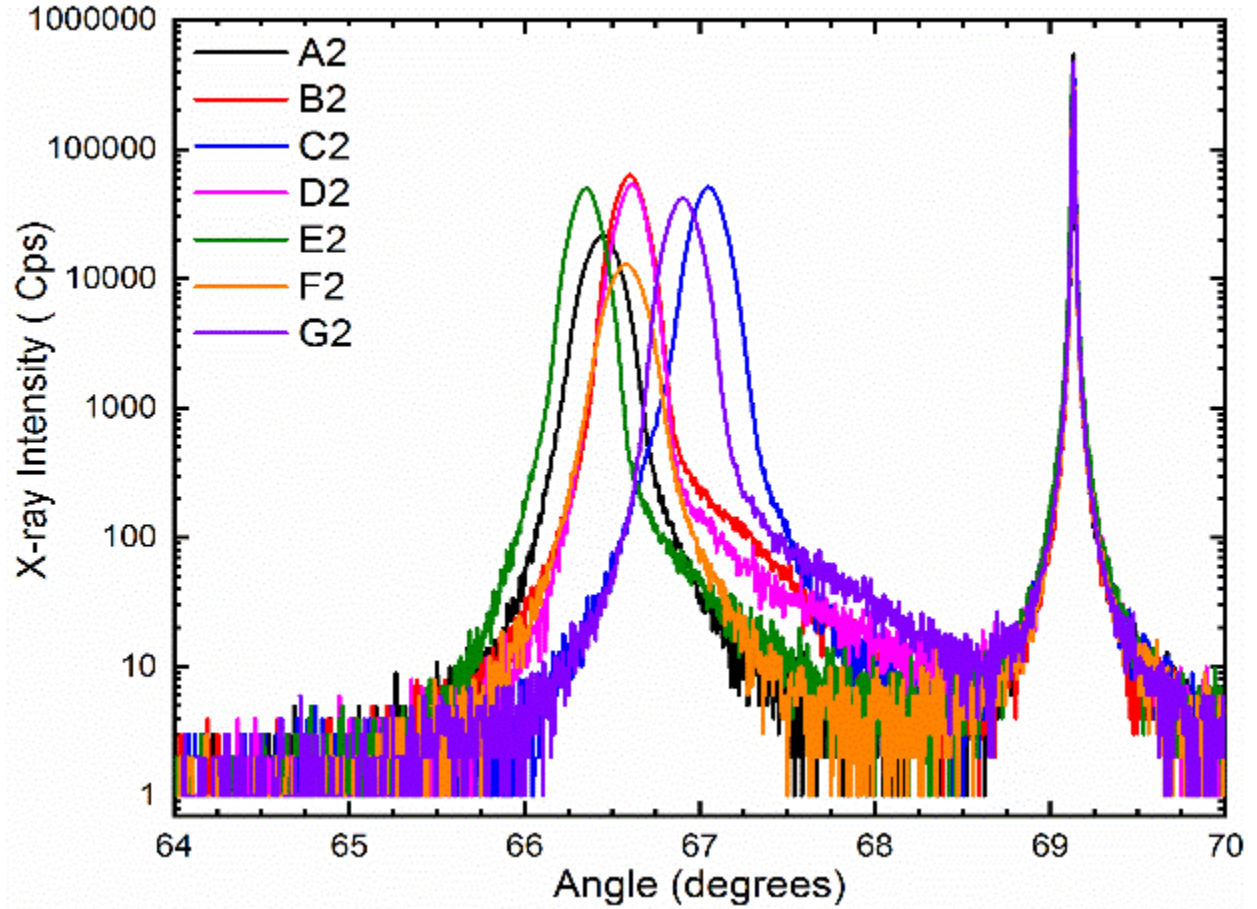


Figure 5.4: Combined plot of SiGe (004) Rocking curves from growths on Si(100) performed at 1.0 Torr using recipes in Table 5.2.

The lattice size was calculated using.

$$a_0 = d_{hkl} / \sqrt{h^2 + k^2 + l^2} \quad (\text{Equation 5.2})$$

where the parameter  $a_0$  is the lattice size,  $d_{hkl}$  is the d-spacing from Equation 5.1 and  $h$ ,  $k$ , and  $l$  are the Miller indices of the incident plane for the x-ray beam. The percent of incorporation of Si ( $x$ ) and Ge ( $1 - x$ ) could be calculated using Vegard's law for binary alloys

$$a_0^{Si_x Ge_{1-x}} = (1 - x)a_0^{Ge} + a_0^{Si} - b^{SiGe} x(1 - x) \quad (\text{Equation 5.3})$$

where  $a_0^{Si_x Ge_{1-x}}$ ,  $a_0^{Ge}$ , and  $a_0^{Si}$  are the lattice constants of  $Si_x Ge_{1-x}$ , Ge, and Si, respectively. The

Table 5.3: Calculations showing d-spacing and lattice constant from Bragg's Law, and percentage of incorporation with and without the bowing parameter from Vegard's Law.

Substrate	Sample #	Thickness (nm)	FWHM	Fitted 2Theta Position	d-Spacing	with bowing factor			Linear		
						Vegard's law lattice constant	Si%	Ge%	Vegard's law lattice constant	Si%	Ge%
Si (100)	A2	1811	0.224	66.444	1.406	5.62	13.3	86.7	5.62	15.1	84.9
Si (100)	A1	69	0.401	66.323	1.408	5.63	9.8	90.2	5.63	11.1	88.9
Si (100)	B1 High Peak	160	0.396	66.888	1.398	5.59	25.9	74.1	5.59	29.6	70.4
	B1 Low Peak		0.507	67.498	1.387	5.56	42.4	57.6	5.55	49.3	50.7
Si (100)	C1	125	0.352	66.642	1.402	5.61	19.0	81.0	5.61	21.6	78.4
Si (100)	D1 Low peak	138	0.380	66.319	1.408	5.63	9.7	90.3	5.63	10.9	89.1
	D1 High peak		0.411	66.793	1.399	5.60	23.2	76.8	5.60	26.5	73.5
Si (100)	E1	149	0.303	67.075	1.394	5.58	31.0	69.0	5.58	35.7	64.3
Si (100)	B2	3689	0.190	66.598	1.403	5.61	17.7	82.3	5.61	20.1	79.9
Si (100)	C2	2548	0.200	67.049	1.395	5.58	30.3	69.7	5.58	34.8	65.2
Si (100)	D2	2221	0.180	66.609	1.403	5.61	18.0	82.0	5.61	20.5	79.5
Si (100)	E2	2482	0.182	66.349	1.408	5.63	10.6	89.4	5.63	11.9	88.1
Si (100)	F2	1388	0.233	66.576	1.403	5.62	17.1	82.9	5.61	19.4	80.6
Si (100)	G2	3581	0.201	66.901	1.397	5.59	26.3	73.7	5.59	30.1	69.9

bowing parameter of SiGe is taken as  $b^{SiGe} = 0.026$  nm [3]. As film thickness increased, the films relaxed more and a 125 nm film with 19% Si was nearly fully relaxed on Si (100) (Figure 5.5).

The growths at higher pressure had XRD rocking curve measurements that showed crystal quality improvement through all temperature ranges. The FWHM calculations from the XRD rocking curves showed that the lower pressure growths varied between 0.30 to as high as 0.60 degrees. The high pressure growths showed a FWHM ranging from 0.18 to 0.23 degrees (Figure 5.6), which was indicative of higher quality material when compared to the growths at lower pressure. These measurements showed a definitive shift in peak position as incorporation of Si increased with increases in flow rate of silane and also that temperature above 500 °C only provided minor improvement in crystal quality. The calculated growth rates of the films were

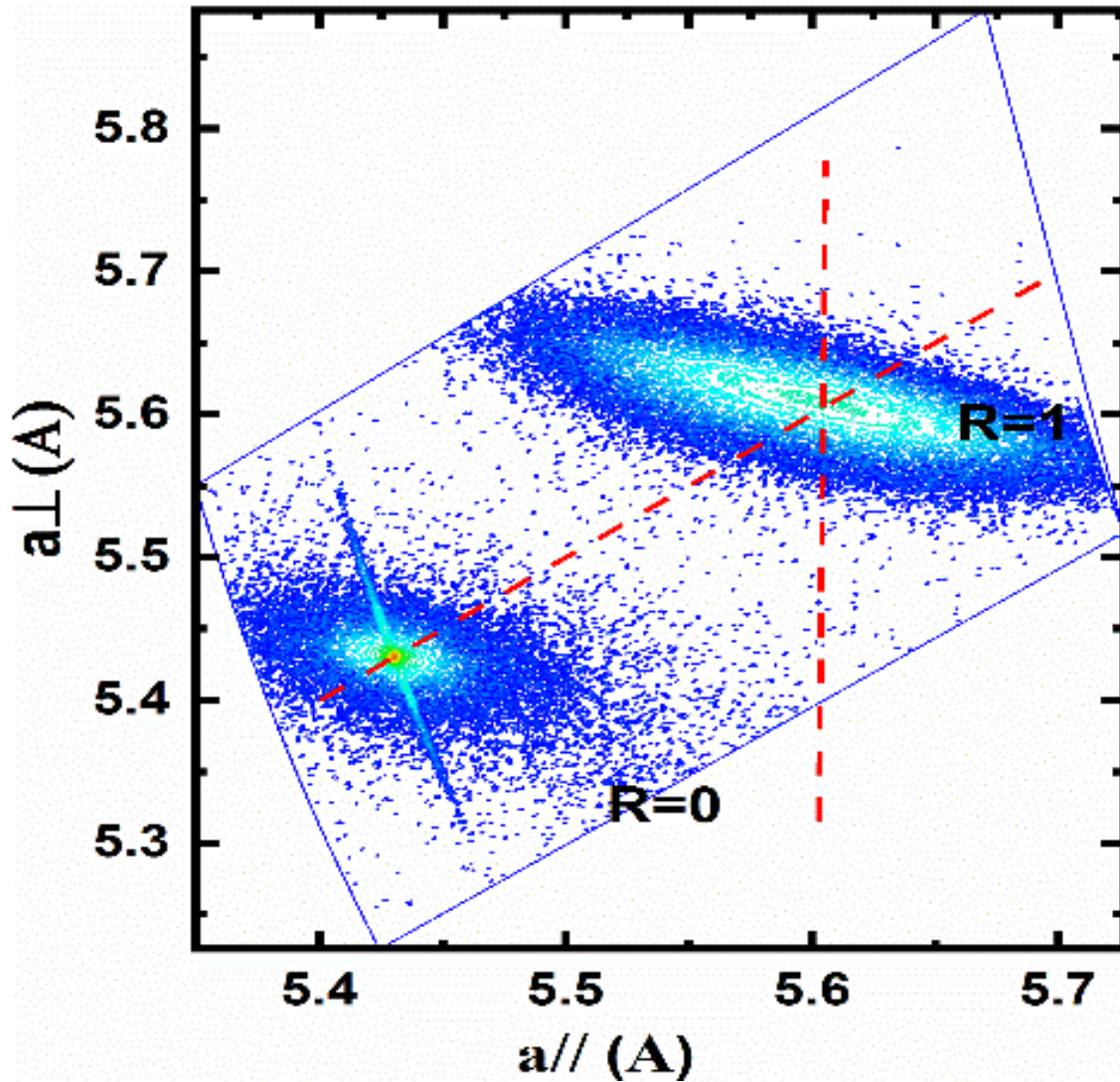


Figure 5.5: Typical XRD-RSM plot showing relaxed film growth.

from 93 nm/min to as high as 246 nm/min for the high pressure growths as compared to the low pressure growths which ranged from 4.6 nm/min to 10.6 nm/min. The growth rates of the samples as a function of temperature show a reduced growth rate through the entire selected growth window for low pressure growths when compared to the high pressure growths (Figure 5.7a). It was noted that the high pressure growths increased in growth rate until 500 °C where the rate peaked and the decrease following this peak was indicative of a gas-phase transport regime to mass flow limited regime crossover. The temperatures above 500 °C entered the mass



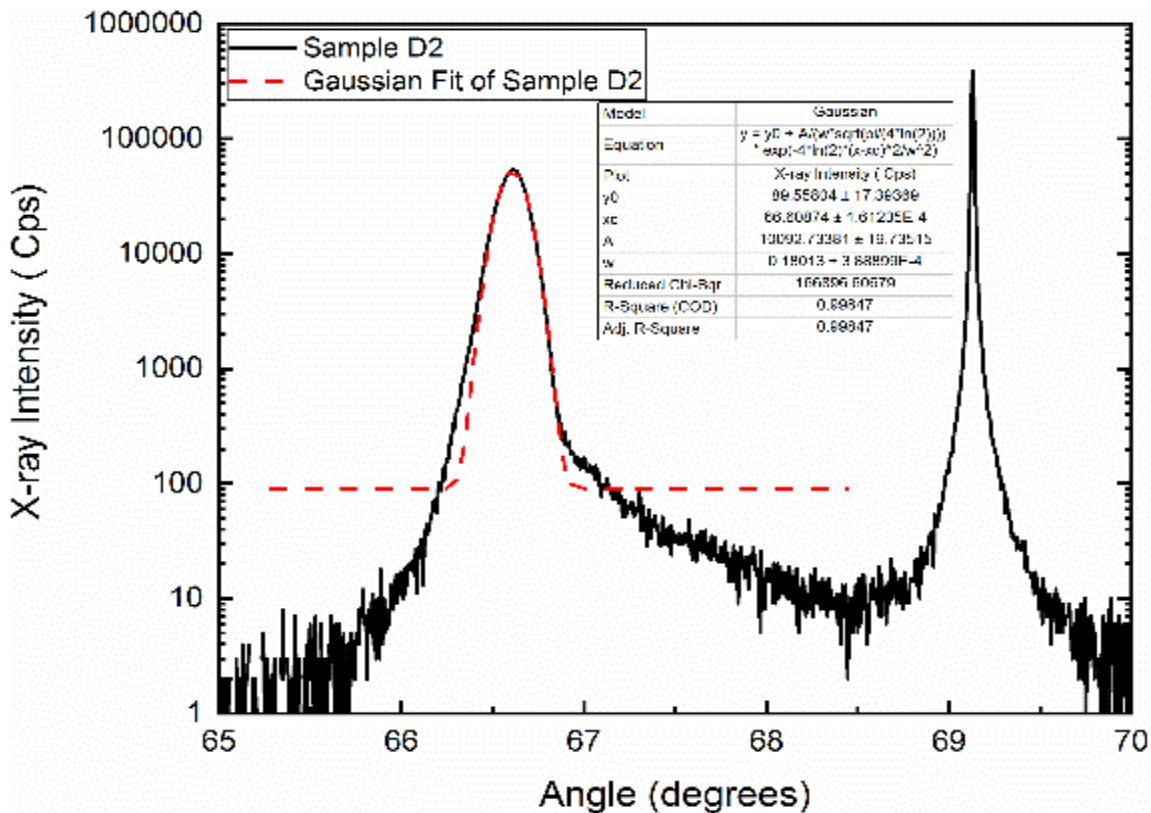


Figure 5.6: Typical XRD rocking curve with Gaussian fitting for SiGe samples grown on Si(100) at 1.0 Torr.

flow limited regime as some precursors decomposed faster than others and deposited elsewhere in the chamber. It was determined the higher growth rates of the high pressure growths would

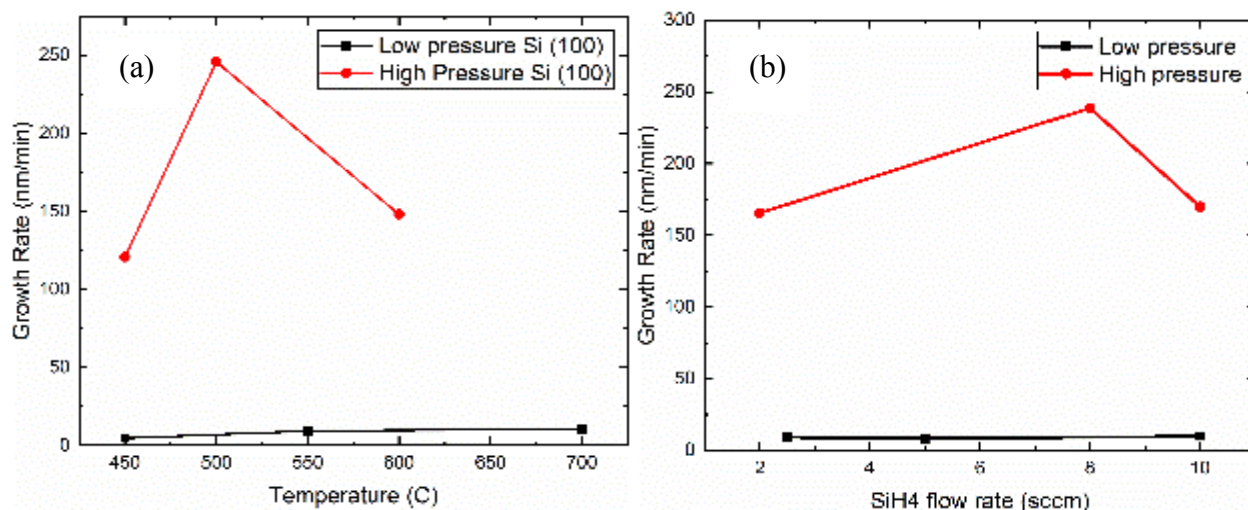


Figure 5.7: Plots of growth rate as a function of temperature (a) and SiH4 flow rate (b).



provide the needed recipes for the planned future growths as the growth rate was expected to be reduced when other substrates with different crystalline orientations were used. The recipes developed here and their high growth rates were used to subsequently develop the recipes for the matrices for the growths of SiGe on Si (111) substrates.

### **5.3 Growth on Si (111) growth matrix**

The growth on Si (111) was done with the intention of using the growths as a comparison for the planned growths on c-plane sapphire. The planning for this series of growths started with the formulation of a growth matrix. The matrix was determined using recipes from the growth of SiGe on Si (100) using the custom built cold walled Ultra High Vacuum Chemical Vapor Deposition (UHV-CVD) reactor. Prior to growth the substrates were cleaned using the above described wafer preparation and loaded in to the load lock of the ultra-high vacuum chemical vapor deposition chamber. The sample substrates in the load lock were kept at a base pressure of  $10^{-7}$  Torr to reduce native oxide formation. The substrates were then transferred individually to the process chamber of the chemical vapor deposition reactor where they were heated to growth temperature. The growth temperature was maintained for 20 minutes for a heat soak to ensure that the substrate was uniform in temperature to prevent thermal gradients due to the sample cradle acting as a heat sink. The temperature range for these growths was from 500-600 °C. The flow rate for the germanium precursor was 10 sccm for a growth pressure of 1.0 Torr. The flow rate for the silicon precursor was set at 4 sccm. The flow rate for the carrier gas was set at a rate of 25 sccm. The length of time for all growths was fixed at 15 minutes (Table 5.4). These growths had a reduced growth rate when compared to the above-mentioned high-pressure growths on Si (100) (Figure 5.8).

The XRD rocking curve measurements of the samples showed that the material quality

Table 5.4: Growth matrix for growths on Si (111).

SiGe Growth Matrix Si (111)		Grown samples shown			Precursor GeH <sub>4</sub> F.R. (sccm): 10						
Time	F.R. (sccm) of Carrier Gas (Ar)	Growth Pressure (Torr)	Temperature			450	500	550	600	650	700
			Precursor SiH <sub>4</sub> F.R. (sccm)								
15	25	1	1								
			2								
			4		A3	B3	C3				
			6								
			8								
			10								

was poor but that the quality improved as the growth temperature increased. These measurements also showed a definitive narrowing of the peak shape with increase in temperature

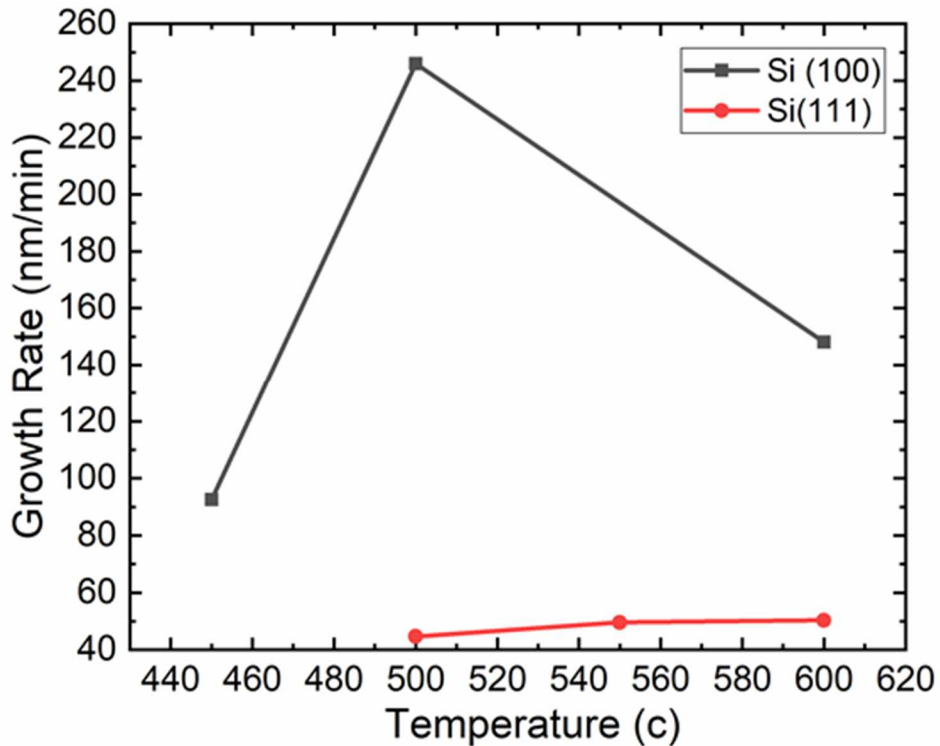


Figure 5.8: Comparison plot of growth rate versus deposition temperature for sample grown on Si (100) and Si (111).

indicating improvement in the crystal quality (Figure 5.9). The samples showed a peak around 395 cm<sup>-1</sup> in the Raman spectroscopy measurements (Figure 5.10). Ellipsometry measurements of

the samples also showed that the absorption cutoff with respect to the wavelength (Figure 5.11) shifted toward shorter wavelengths as the incorporation of Si increased in the films when

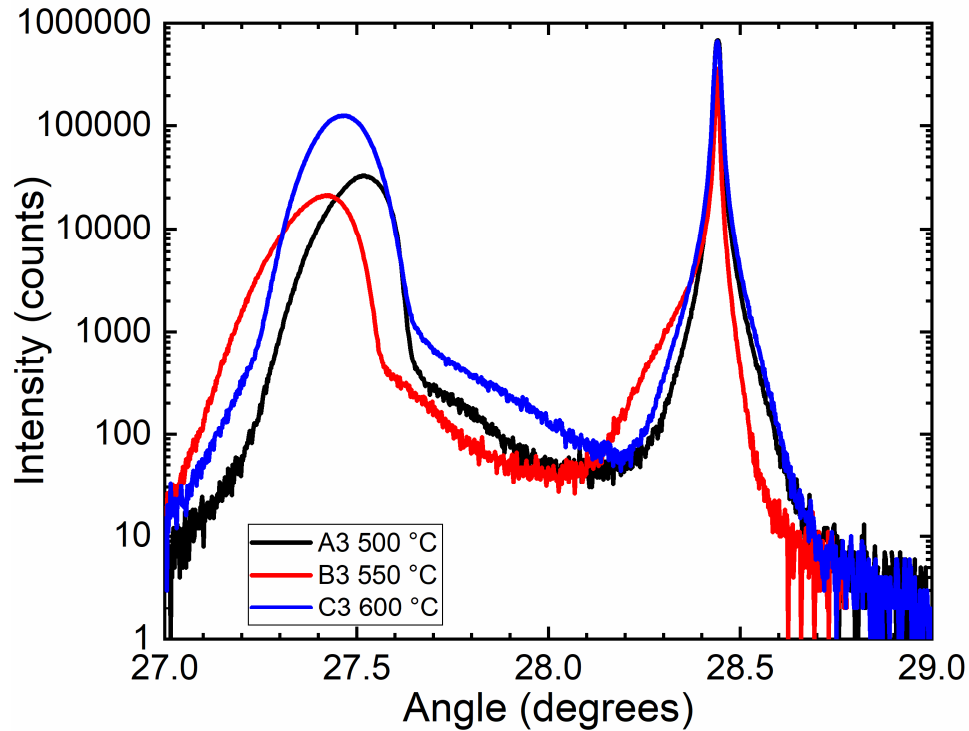


Figure 5.10: Comparison XRD-RC plot for samples grown on Si (111) showing improvement in quality as temperature increases.

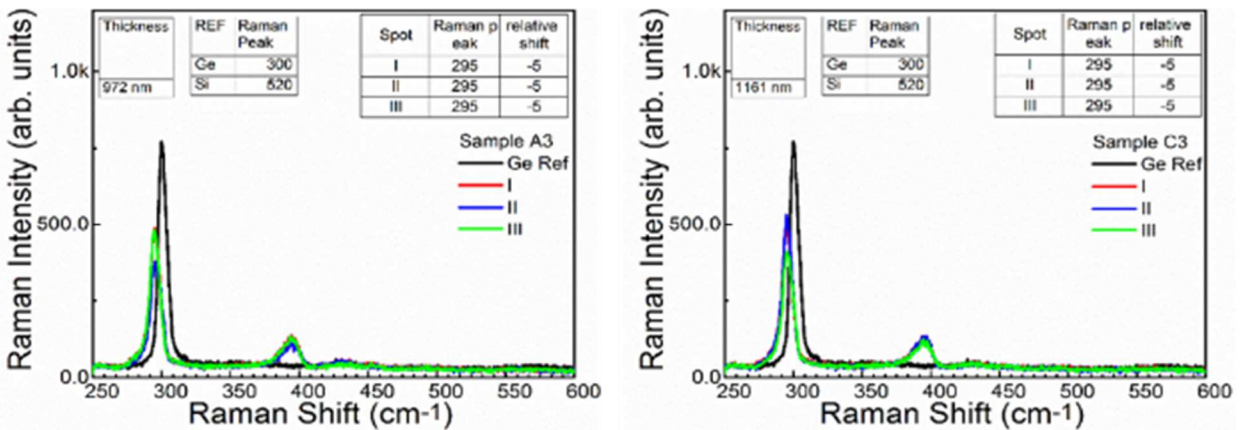


Figure 5.9: Typical Raman plots for samples grown on Si (111) showing shifted Ge-Ge LO phonon peak shift and Ge-Si LO phonon peaks near 395  $\text{cm}^{-1}$ .

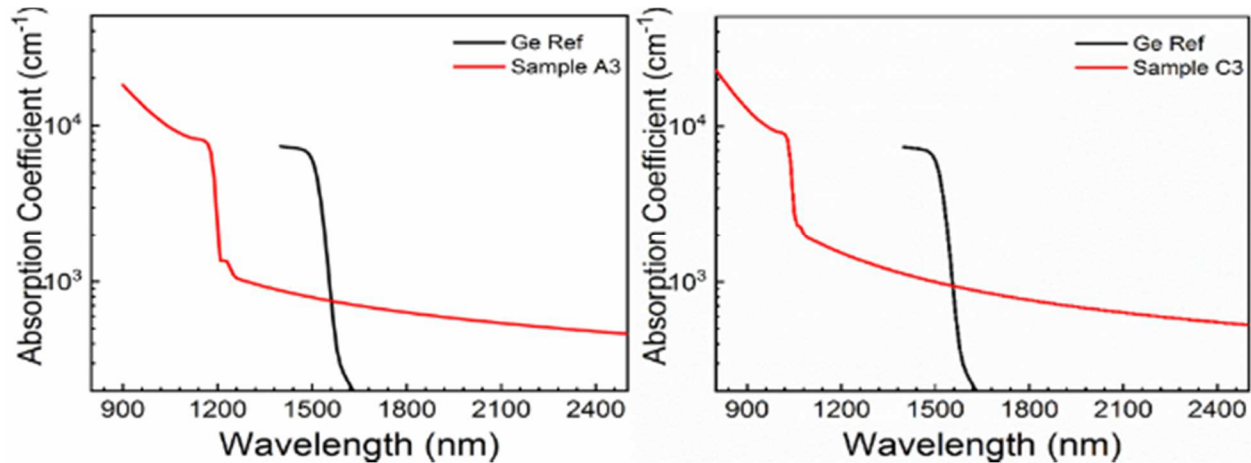


Figure 5.11: Typical absorption coefficient plots from ellipsometry measurements showing shifted cutoff wavelengths.

compared to data in Table 5.3. The FWHM of the XRD measurements ranged from 0.07 to 0.09 degrees using a bi-Gaussian fitting due to the asymmetric peak shape (Figure 5.12). The

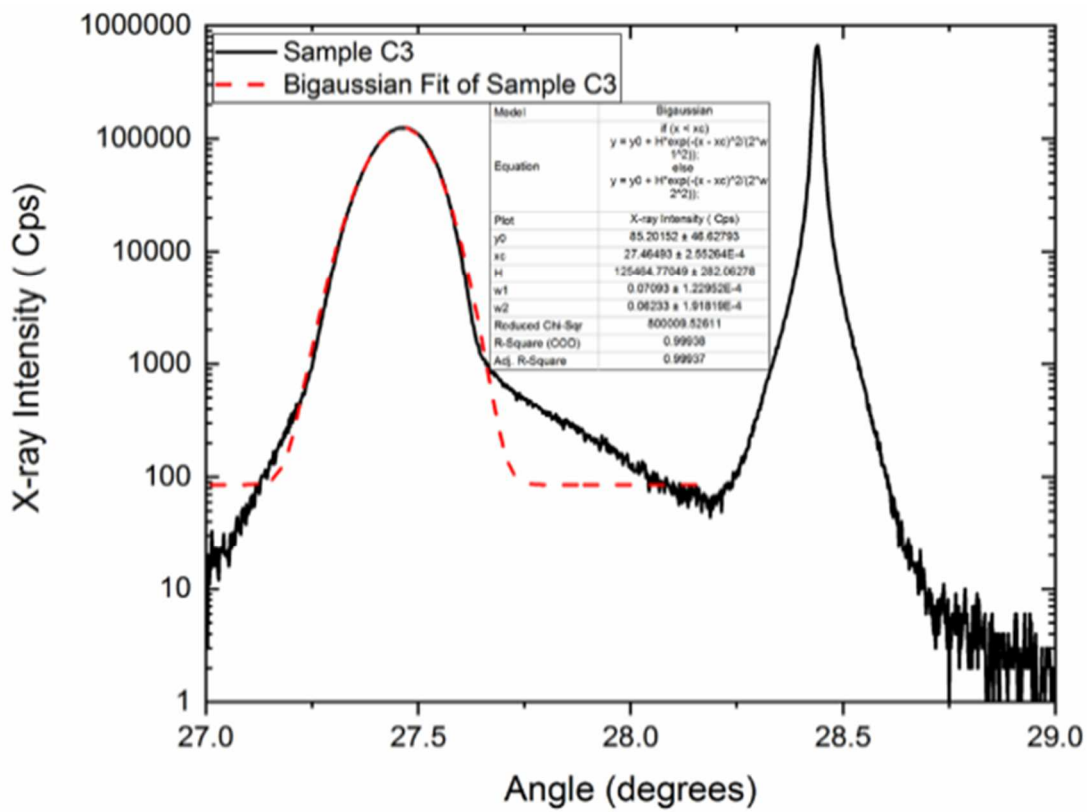


Figure 5.12: Typical XRD-RC plot showing bi-Gaussian fitting (dotted line).

incorporation of Si ranged from 10 to 13% for the samples and was calculated from fitted peak positions using Bragg's law and incorporation percentages based on Vegard's law with and without bowing parameters (Table 5.5). However, as these growths were only used to provide verification of growth parameters, no further growth work was pursued.

Table 5.5: Calculated data from XRD rocking curves providing d-spacing and lattice size.

Substrate	Sample #	Thickness (nm)	FWHM	Fitted 2Theta Position	d- Spacing	w/ bowing factor			Linear		
						Vegard's law lattice constant	Si%	Ge%	Vegard's law lattice constant	Si%	Ge%
Si(111)	A3	972	0.083 0.048	27.526	3.238	5.610	19.3	80.7	5.61	22.0	78.0
Si(111)	B3	1098	0.094 0.056	27.407	3.252	5.633	10.2	89.8	5.63	11.4	88.6
Si(111)	C3	1161	0.070 0.062	27.465	3.245	5.621	14.7	85.3	5.62	16.6	83.4

#### 5.4 Growth of SiGe on sapphire

The sapphire substrates were first treated with a titanium coating to the backside of the wafers. The surface was then cleaned with methanol and dried with nitrogen prior to loading into the reactor load-lock. The titanium coating was applied to a thickness of 1000 nm in stages of 250 nm using an electron beam evaporator. The titanium backing was to absorb radiative heat from the heating element since wafer heating was noncontact radiative heating in the process chamber. These growths varied in temperature range from 500-600 °C with the flow rates of silane varying from 2-6 sccm (Table 5.6). These were done to examine the temperature dependence and silane flow rate dependence for the material as the recipes were refined to accomplish a rhombohedral growth of SiGe on sapphire substrates using the chemical vapor deposition method as no such work has been reported. As with the prior growths, these were

done for a fixed time of 15 min. The germane flow rate was set at 25 sccm following the high-pressure matrix developed during the Si (100) growths. The growth pressure was set at 1.0 Torr

Table 5.6: Refined growth matrix for SiGe on sapphire substrates for deposition temperature and SiH<sub>4</sub> flow rate dependence.

SiGe Growth Matrix Sapphire		Grown samples shown		Precursor GeH <sub>4</sub> F.R. (sccm): 10						
Time	F.R. (sccm) of Carrier Gas (Ar)	Growth Pressure (Torr)	Temperature	450	500	550	600	650	700	
			Precursor SiH <sub>4</sub> F.R. (sccm)							
15	25	1	1							
			2			D4				
			4		A4	B4	C4			
			6			E4				
			8							
			10							

as was used in the prior growths.

The films grown during for this portion of the research were characterized using ellipsometry, growth rate, absorption coefficient, crystal quality, lattice sizes, and silicon incorporation of each of the grown samples. The ellipsometry results from these growths showed that the growth rate for the films varied from 33-60 nm/min. The absorption coefficients generated from the fitting of ellipsometry data showed that the absorption cutoff wavelength reduced as the percent incorporation of silicon increased in the samples (Figure 5.13). The Raman spectroscopy of the

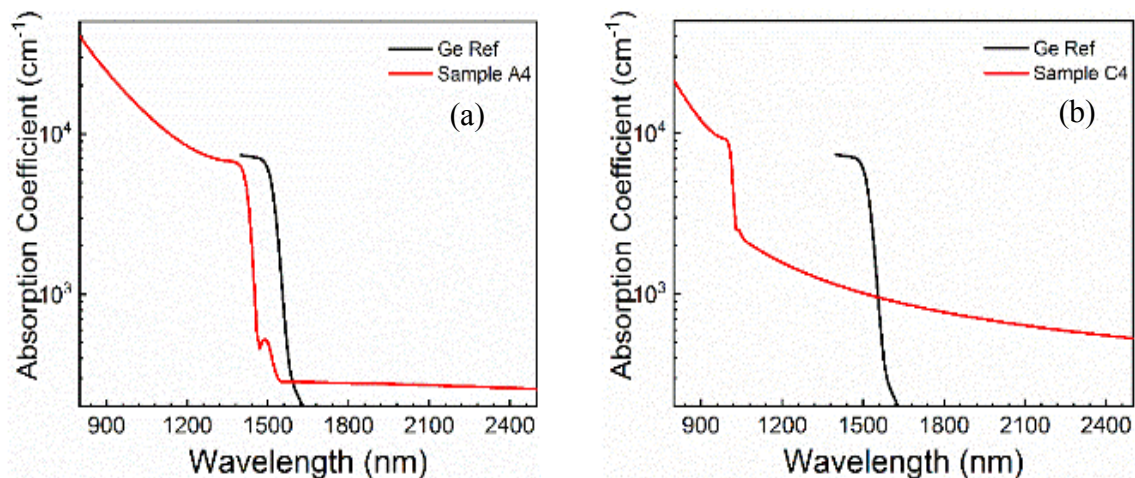


Figure 5.13: Ellipsometry plots of the absorption coefficient as a function of wavelength for two SiGe samples grown on sapphire.

sample showed a Si-Ge peak at a Raman shift of 395  $\text{cm}^{-1}$  which was also observed in the growths on Si (100) and Si (111) (Figure 5.14). The XRD rocking curves showed that the incorporation increased with an increase in flow rate of silane and that material quality improved with increases in temperature. The composition of the films ranged from 5-22 % from the fitting

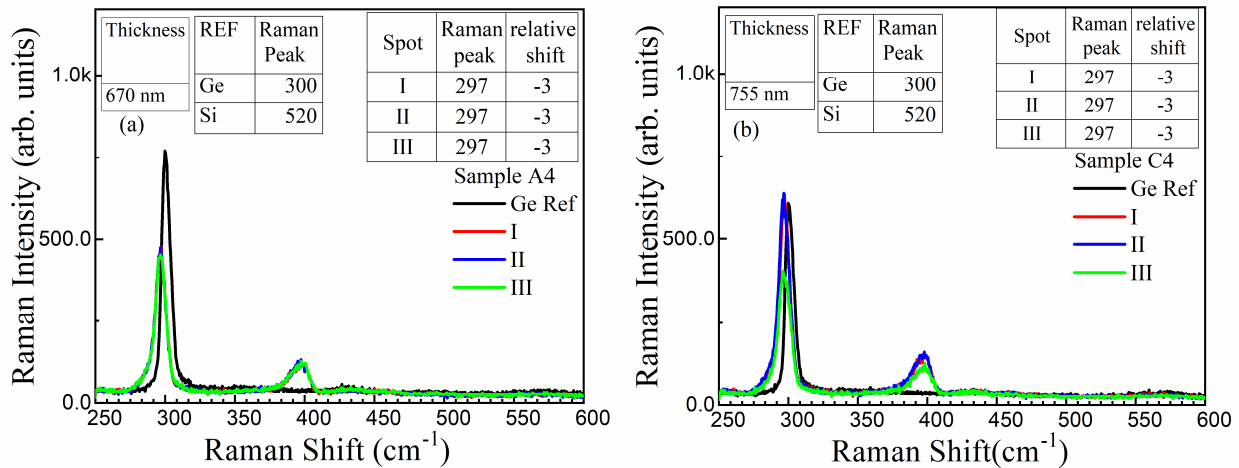


Figure 5.14: Comparison of Raman plots for two SiGe samples grown on sapphire at (a) 500 °C and (b) 600 °C.

of the peak positions of the XRD rocking curves when applied to Equations 1, 2, and 3 (Table 5.7). The FWHM of the XRD rocking curve measurements varied from 0.22-0.24 degrees. The incorporation of Si in the films varied as the  $\text{SiH}_4$  flow rate changed as shown in the shifting of

Table 5.7: Calculations of d-spacing and lattice constants using Bragg's Law from the Gaussian fit of XRD rocking curve peaks.

Substrate	Sample #	Thickness (nm)	FWHM	Fitted 2Theta Position	d-Spacing	w/ bowing factor			linear		
						Vegard's law lattice constant	Si%	Ge%	Vegards law	Si%	Ge%
Sapphire	A4	670	0.248	27.454	3.246	5.62	13.9	86.1	5.62	15.7	84.3
Sapphire	B4	744	0.241	27.445	3.247	5.63	13.2	86.8	5.62	14.9	85.1
Sapphire	C4	755	0.226	27.444	3.247	5.63	13.1	86.9	5.62	14.8	85.2
Sapphire	D4	500	0.238	27.340	3.259	5.65	5.0	95.0	5.65	5.6	94.4
Sapphire	E4	905	0.236	27.567	3.233	5.60	22.4	77.6	5.60	25.6	74.4

the peak positions (Figure 5.15). The intensity increases were observed for the samples as the

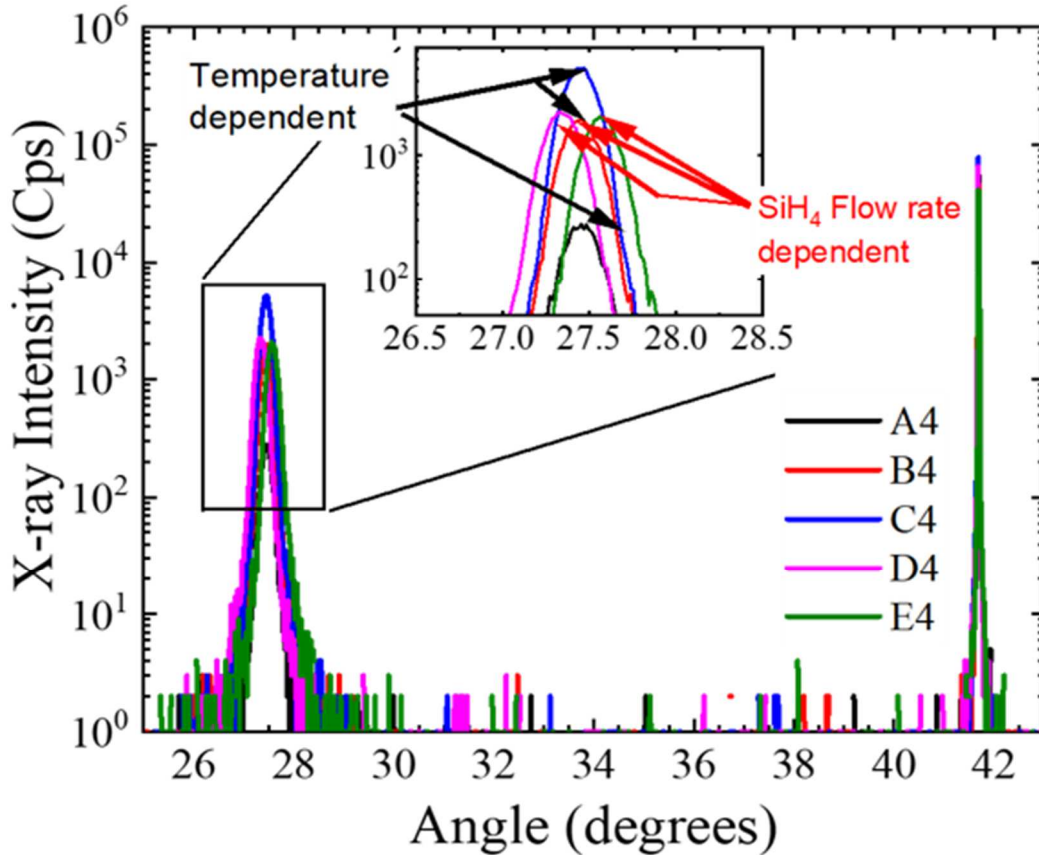


Figure 5.15: Plot of XRD-RC for growths on sapphire (0001) showing differences in Si incorporation as  $\text{SiH}_4$  flow rates change for a given temperature.

temperature increased for a given  $\text{SiH}_4$  flow rate which was consistent with material quality improvement at the same levels of incorporation. The x-ray diffraction rocking curves were compared for the growths on Si (111) and sapphire substrates (Figure 5.16). The peaks for the SiGe (111) were in alignment for films on both substrates. The intensity of the samples grown on Si (111) was larger than those grown on sapphire. This increase in intensity can be explained by the lattice parameters of Si (111) being more closely matched to SiGe (111) as both are cubic structures with lattice constants of 5.43 and 5.62 Å, respectively. Whereas, the lattice structure of sapphire (0001) is trigonal with a lattice parameter of 4.73 Å. X-ray diffraction rocking



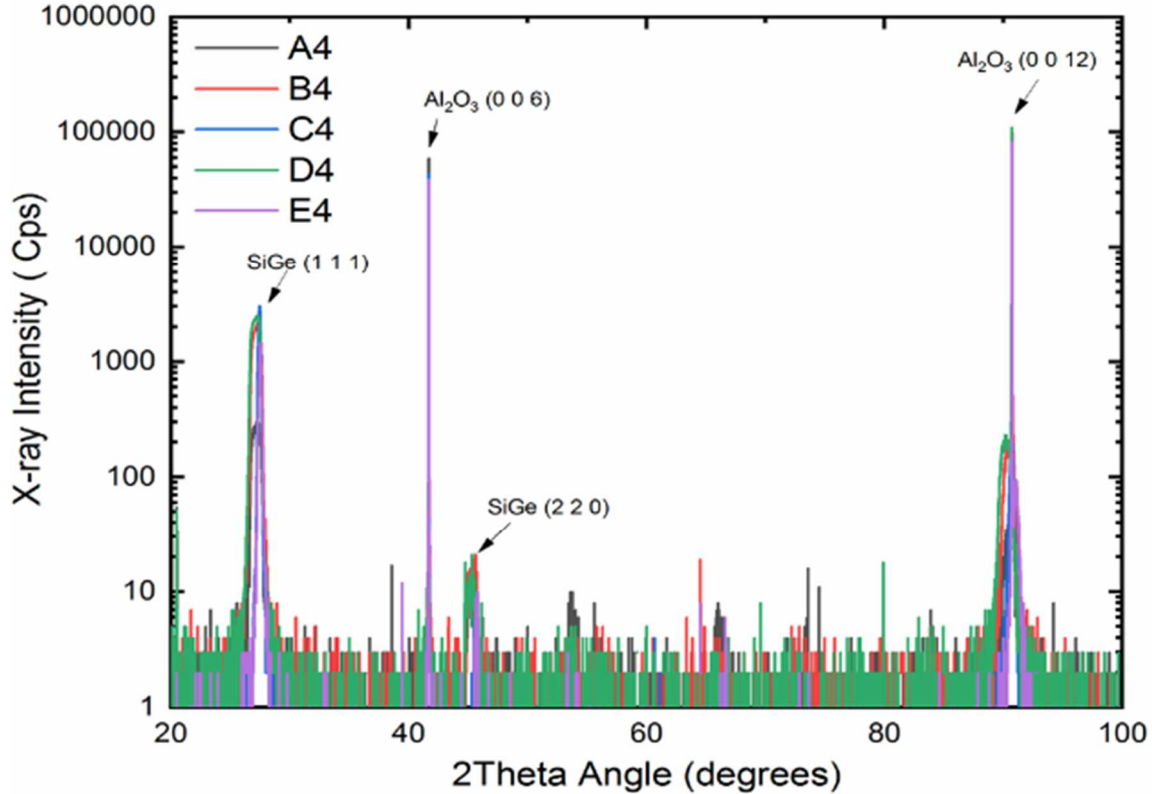


Figure 5.16: Combined XRD rocking curve plot of SiGe (111) growths on Si(111) and sapphire (0001).

curves were obtained over a wide degree range. The rocking curves showed peaks for SiGe (111) at  $\sim 27.44$  degrees, sapphire (006) at  $\sim 41.68$  degrees, sapphire (0012) at  $\sim 90.72$  degrees, and a low intensity SiGe (220) peak at  $\sim 45.33$  degrees. The peak for SiGe (220) indicates there was a polycrystalline structure in the films grown on sapphire (006). X-ray diffraction phi scans were measured along the (004) plane for all of the samples. The results of the phi scans showed evidence of crystal twins separated by 60 degrees (Figure 5.17). AFM images were obtained from these samples and the results show that the film surface was rough varying from 39.2-67.4 nm Rms (Table 5.8). The imaged surface appeared to have trigonal structures that would indicate a three-dimensional growth regime (Figure 5.18). This growth could be caused by the twinning of the crystal resulting in the rough surface. This type of surface could also be related

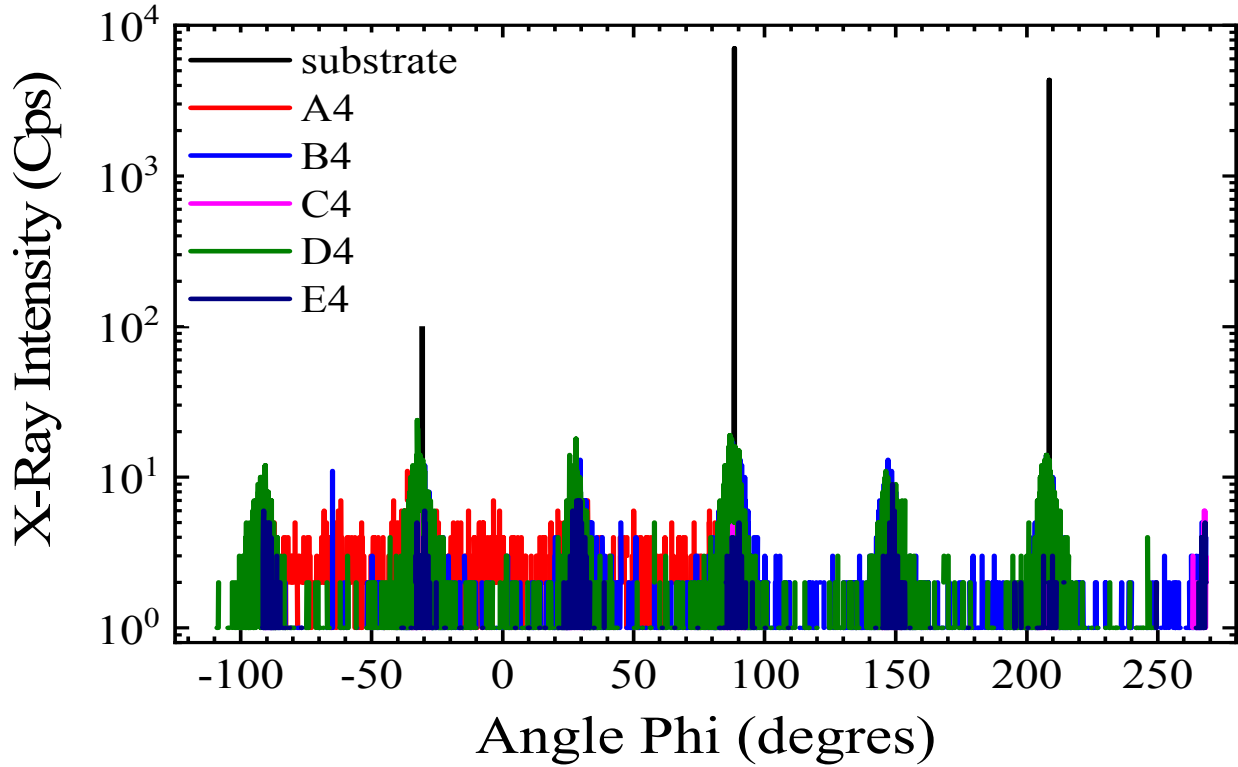


Figure 5.17: Typical x-ray diffraction phi scans along (004).

to the surface roughness of the sapphire substrate which did not have a high heat anneal performed prior to the deposition of titanium backing.

Table 5.8: Table of measurements from AFM image analysis.

Sample	5x5 $\mu\text{m}$	10x10 $\mu\text{m}$	
A4	25.24 nm	41.12 nm	Ra
A4	31.33 nm	50.57 nm	Rrms Roughness
B4	30.17 nm	31.5 nm	Ra
B4	37.33 nm	39.21 nm	Rrms Roughness
C4	44.86 nm	46.1 nm	Ra
C4	54.77 nm	56.91 nm	Rrms Roughness
D4	35.37 nm	53.34 nm	Ra
D4	44.24 nm	67.47 nm	Rrms Roughness
E4	59.72 nm	38.25 nm	Ra
E4	71.9 nm	47.29 nm	Rrms Roughness

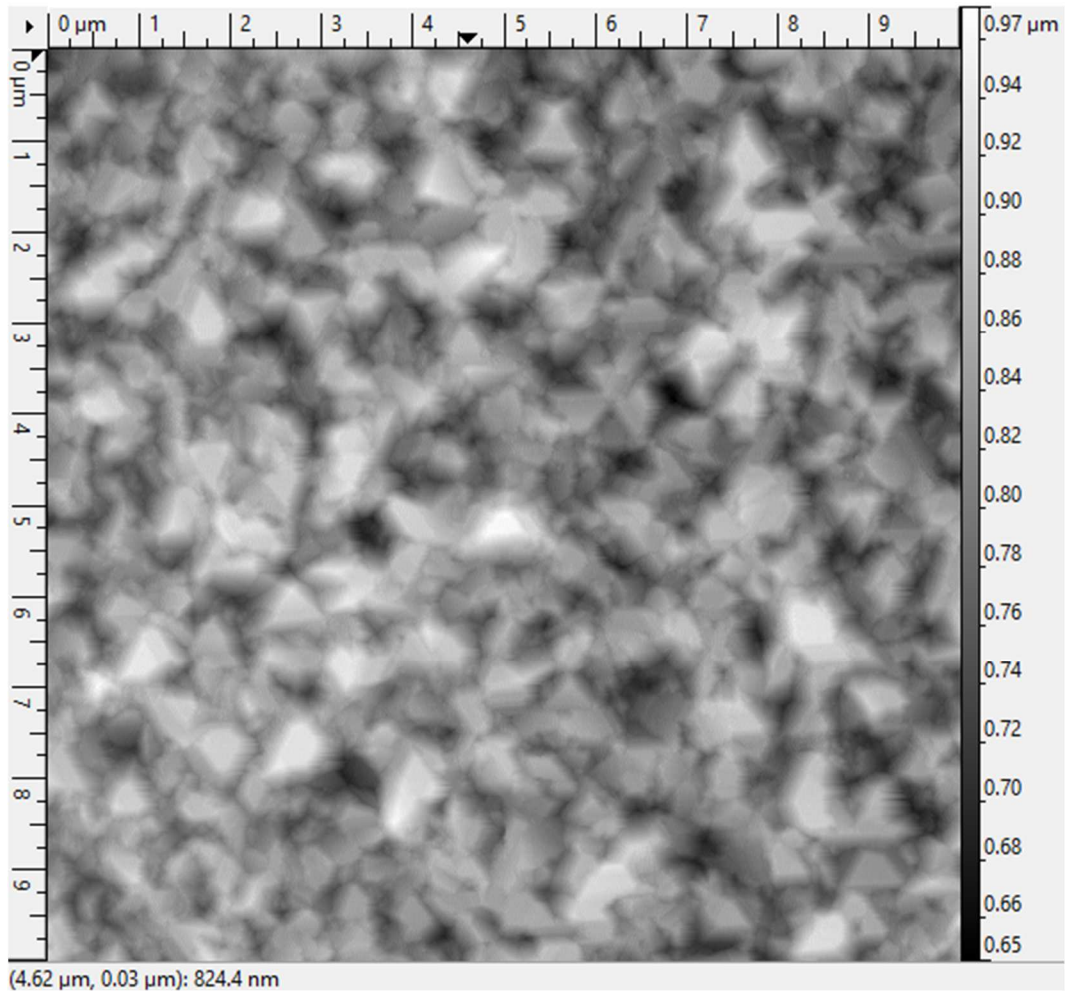


Figure 5.18: AFM image of surface showing multiple trigonal structures.

## Chapter 6 GeSn Growth Work

### 6.1 Introduction

The introduction of the GeSn material system to group IV photonics has provided an integrable direct band gap material for photonic use on silicon substrates [25][26]. Devices based on direct band gap GeSn such as LEDs, lasers, and photodetectors have shown the potential of this material system [27][28][29]. Commercialization of applications based on devices developed from this material system could provide new inexpensive and efficient light emission and detection systems and components to the photonics market.

The growth of the GeSn material system is challenged due to the instability of semiconductor Sn ( $\alpha$ -Sn) at temperatures greater than 13 °C and the low solubility of Sn in Ge (<1%) [30]. Growth techniques have been developed to face the challenges and provide growth of this material system under non-equilibrium conditions such as low temperature growth by MBE [31][32][33][34] or CVD [35][36][18][37]. The growth by chemical vapor deposition has been studied for more than a decade by multiple groups. During these studies, many different Ge and Sn precursor sources have been tried along with different carrier gases to achieve high quality material with high amounts of Sn incorporation [38][39][40][41]. In the early development phase for the GeSn material, the growths were performed using SnD<sub>4</sub>, deuterium stabilized stannane, for the Sn source precursor [35]. The high instability and cost of this precursor source led to a search for a cheaper and more stable Sn precursor source. The Sn precursor stannic chloride (SnCl<sub>4</sub>) was first demonstrated and reported in 2011 by Vincent, et al [42]. The use of high order hydrides of Ge have been studied as Ge precursors [35]. The use of these high order Ge hydrides was common due to their low temperature decomposition [37]. The low cost of the commercially available precursor, germane (GeH<sub>4</sub>), has resulted in use

recently for the growth and development of Ge and GeSn using UHV-CVD systems [37][23][43][29].

The growth of the GeSn material system will be discussed in this section. The growth of GeSn directly to the silicon substrate, on Ge buffered Si, and the process by which the Sn composition and material quality was improved will be covered. This will cover the effects of temperature and pressure on the material system and the necessary adjustments to the growths to achieve desired material properties. The properties of the GeSn material will be explored through different optical characterizations to provide information on growth rate, composition, uniformity, and material quality.

## 6.2 GeSn on Si

The growth of GeSn on Si substrates provided a basis for the development of the GeSn material system by UHV-CVD. These growths were performed using 4-inch p-type substrates that were prepared using a piranha etch solution followed by a HF passivation described by Mosleh, et al [23]. The processed wafers were then used for growths in the cold walled UHV-CVD chamber with a base pressure range of below  $10^{-9}$  Torr. These growths used the precursors of GeH<sub>4</sub>, SnCl<sub>4</sub>, and the carrier gas Ar.

The growths of GeSn on Si substrates were performed using various temperatures, SnCl<sub>4</sub> flow rates, growth pressures, and times. The flow rates for the germanium precursor GeH<sub>4</sub> and the Ar carrier gas were fixed at 10 sccm and 25 sccm, respectively. The temperatures ranged from 300 °C to 450 °C. The flow rate of SnCl<sub>4</sub> was varied within the range of 0.02 sccm to 0.5 sccm. The growth pressure for this series of growths was varied from 100 mTorr to 1 Torr. The time for these growths ranged from 10 to 120 min. The characterizations from these growths provided information on the growth rate dependence on temperature and SnCl<sub>4</sub> flow rate,

material quality, material composition, and lattice parameters using ellipsometry, Raman spectroscopy, PL, and XRD measurements. UHV-CVD growth of GeSn directly on Si was used as the basis for the starting point of this work [23]. Most of the work started with known recipes that produced Ge on silicon substrates as mentioned in Section 4.2 and, adding a dilute amount of SnCl<sub>4</sub> (0.02 sccm) to the process, those grown films were compared to Ge films grown using the same recipes minus the SnCl<sub>4</sub> precursor. The growth rates for the grown films were extracted from fits of ellipsometry data that provided film thickness as a function of time (Figure 6.1).

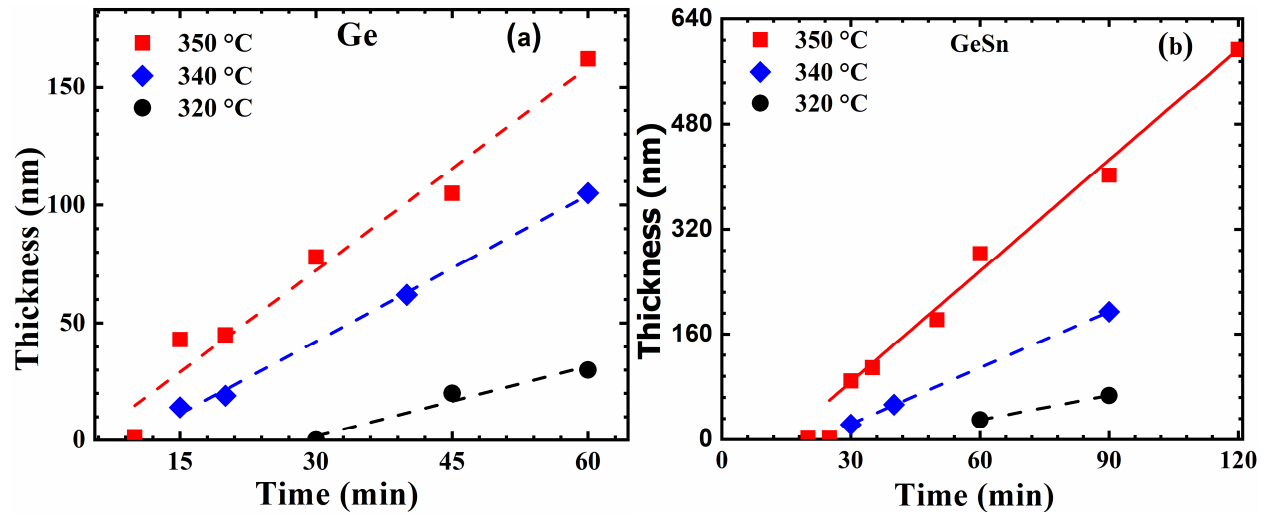


Figure 6.1: Growth rates of (a) Ge and (b) GeSn at varying deposition temperatures.

This provided growth rates for Ge and GeSn that ranged from 1 to 2.8 nm/min and 1.2 to 5.6 nm/min, respectively. The Raman spectra for the selected growths was used to verify film thickness and the incorporation of Sn in GeSn films shown in (Figure 6.2a). Photoluminescence from the selected growths showed no PL for low temperature samples while samples grown at temperatures above 350 °C show room temperature photoluminescence (Figure 6.2b). The films showed increased PL intensity as the film thickness increased. Using the results from the ellipsometry, Raman spectroscopy, and PL measurements, films were further characterized using

XRD. The XRD of the selected GeSn films provided data on the crystal quality and composition

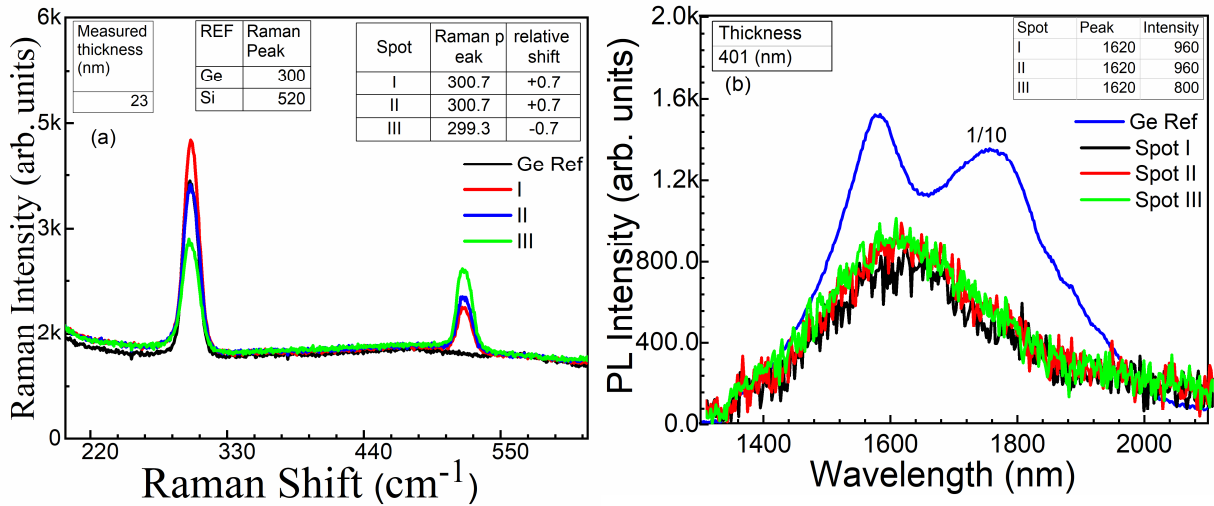


Figure 6.2: Typical plots for (a) Raman spectroscopy for thin films showing both Si-Si and Ge-Ge LO phonon peaks, and (b) photoluminescence measurements, for samples grown above 350  $^{\circ}\text{C}$

as well as the lattice parameters and strain. X-ray diffraction rocking curves were produced using  $2\theta$ - $\omega$  scans of the samples. The intensity of the measurements as a function of the  $2\theta$  angle provided the information on quality by comparing the full-width half-maximum (FWHM) of the Ge peak (Figure 6.3a) and the GeSn peak (Figure 6.3b). The FWHM of the GeSn peaks ranged

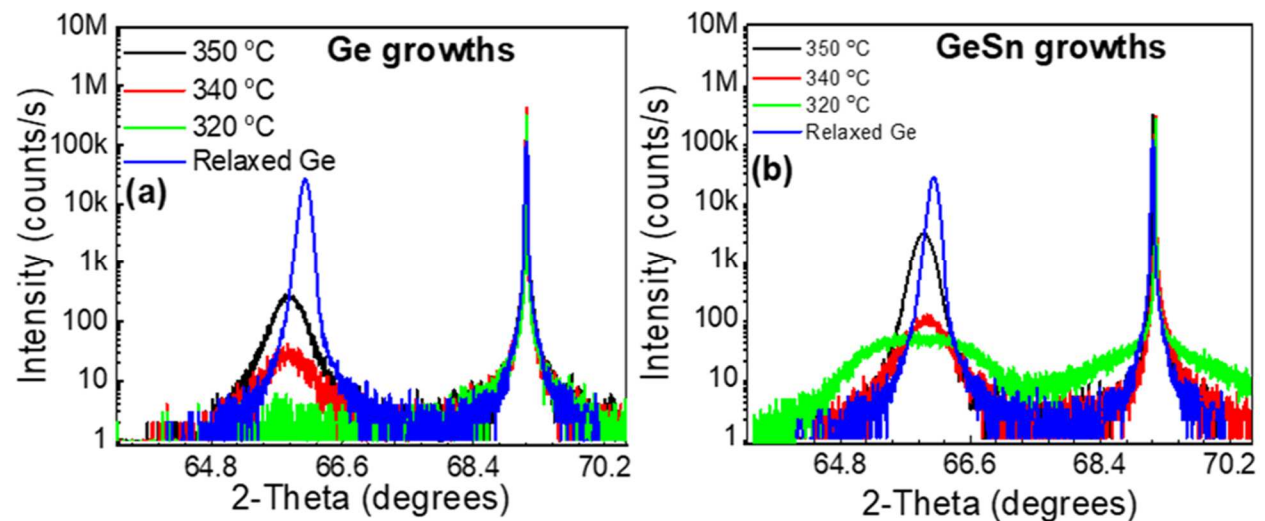


Figure 6.3: XRD-RC plots for (a) Ge and (b) GeSn growths showing improvement in low temperature films with the addition of Sn to the crystalline matrix.

from  $0.246^\circ$  to  $0.887^\circ$  with the smaller angles being indicative of higher quality material. These samples also had a reciprocal space map (RSM) measurement performed using XRD along the (-2-24) plane (Figure 6.4). This RSM measurement provided the information to calculate the strain and composition using the method described by Mosleh, et al [11]. The strain in the

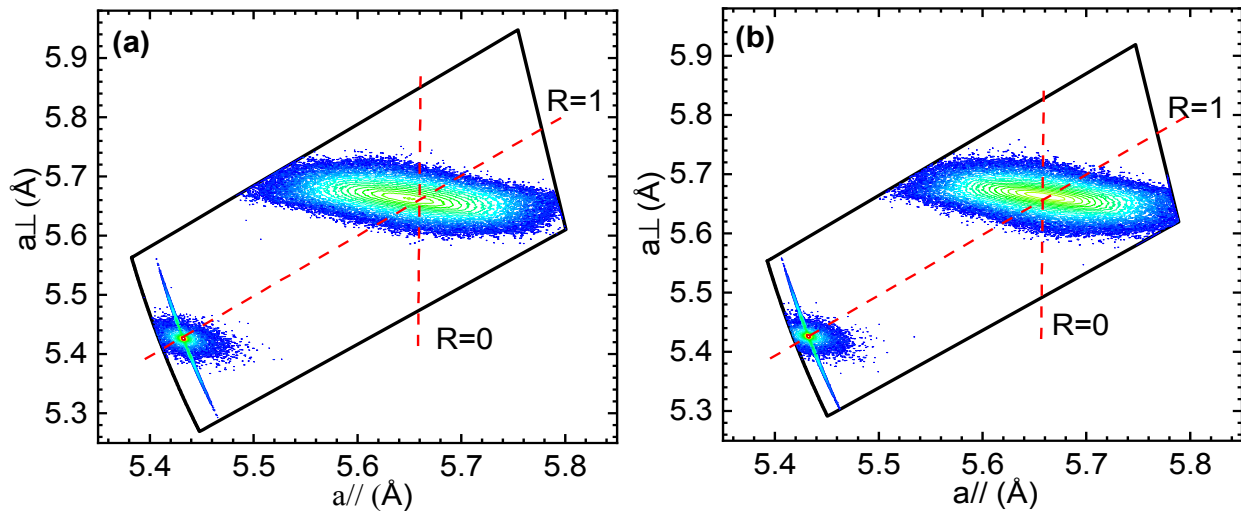


Figure 6.4. Typical reciprocal space map plots of GeSn along (-2-24) plane for (a) sample A and (b) sample B showing relaxed grown films near pseudomorphic to Si.

measured films ranged from 0.06% to 0.13% compressive with the Sn compositions ranging from 0.28% to 0.75%. The low amount of compressive strain in the grown films indicated the films were near fully relaxed. These growths provided important information for subsequent growths as material quality and compositional improvements were necessary to reach the goal of high quality and high Sn composition material.

### 6.3 GeSn on Ge buffered Si

The growth of the GeSn material system has shown challenges due to the lattice mismatch of 4.2% between Ge and Si and the incorporation of Sn in the Ge matrix only increases the mismatch [37]. This mismatch causes strain to form in the epitaxial alloy film. This induced



strain limits the amount of Sn that can be incorporated into the GeSn system [44]. To reduce this difference in lattice mismatch, the LT/HT buffer growth method discussed in Section 4.2 was grown first followed by the epitaxial growth of GeSn. This series of growths used the information discussed in the previous sections to produce recipes for the growth of GeSn on Ge buffered Si. The dilute GeSn on Si growths provided the necessary starting point to greatly reduce the number of experiments needed to achieve high quality with increased Sn incorporation. This started by choosing a temperature at the upper end of the targeted growth matrix. This upper limit was chosen so that sufficient temperature range existed below in the growth window that Sn incorporation could be increased for the starting low SnCl<sub>4</sub> flow rate [44]. This series of growths were varied using temperature and SnCl<sub>4</sub> and GeH<sub>4</sub> flow rates to determine the dependence on temperature and SnCl<sub>4</sub> flow fractions. For these growths, temperatures below 350 °C were chosen to maintain CMOS compatibility of the epitaxial films. The time for the growths was varied in two rounds of growths, the first for 30 min and the second for 60 min for the GeSn layer. The growth pressure for these growths was fixed at 2.0 Torr. These growths were followed by a reduction in the SnCl<sub>4</sub> flow rate until the current machine configuration could no longer support further SnCl<sub>4</sub> dilution. Following the reduction of the SnCl<sub>4</sub> flow rate to the limit, the growth temperature was further reduced until the surface of the produced samples showed visual defects.

The growths for this study were accomplished using p-type, 4-inch Si wafers that were prepared using the previously described method [23]. The growths were characterized using ellipsometry, Raman spectroscopy, PL, XRD, and TEM imaging. The first round of growths grown at 30 min started at 325 °C and the temperature was reduced until growth did not occur at 240 °C using fixed flow rates and pressures. This series of films was used to define the

temperature dependence of Sn composition. The PL results were used to verify Sn incorporation along with results from XRD rocking curves (Figure 6.5). The PL results show that there was a definitive shifting to longer wavelengths which was indicative of increased Sn incorporation.

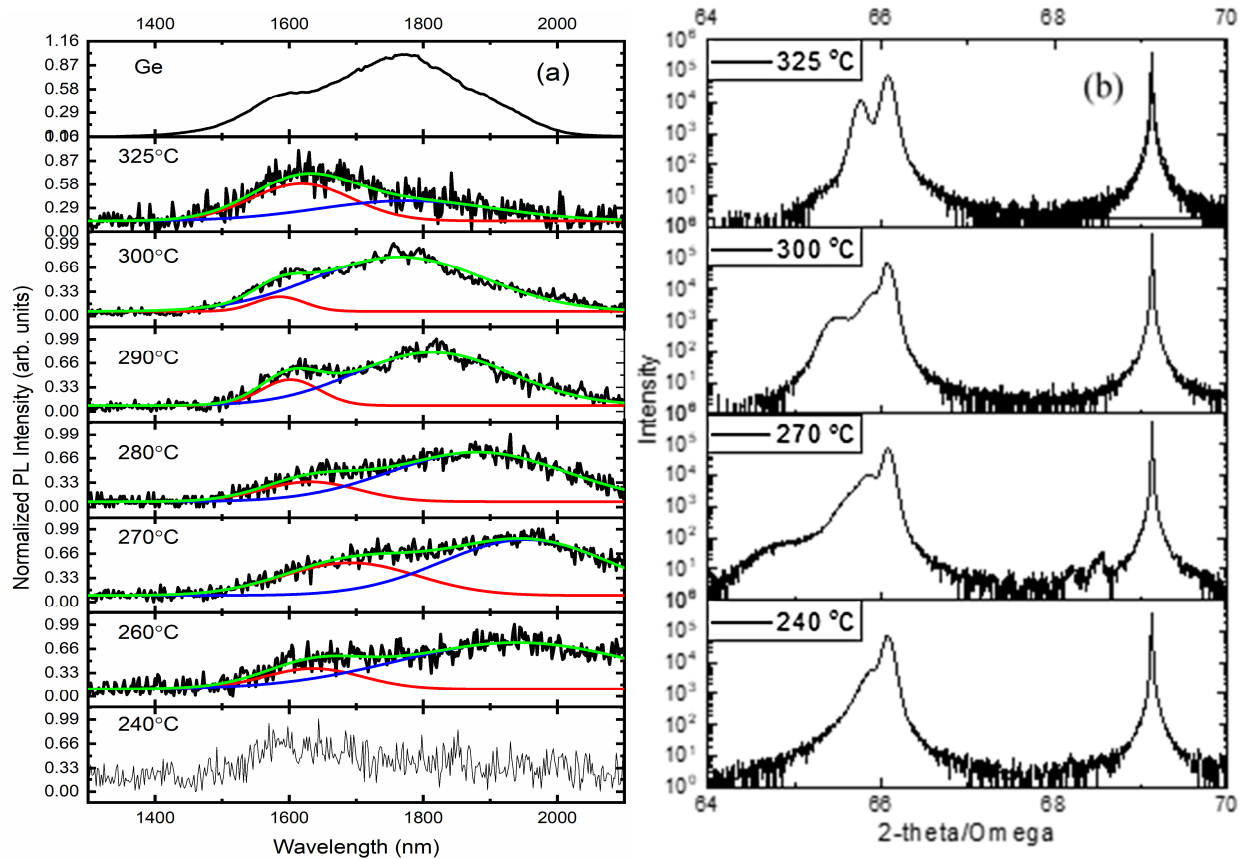


Figure 6.5: Comparison plots of GeSn grown at different temps using (a) photoluminescence and (b) XRD-RC.

The results were confirmed using XRD rocking curves at which the GeSn peak shifted to lower angles which was indicative of larger amounts of Sn composition in the epitaxial alloy film.

These rocking curves also indicated an extra peak at growth temperature below 325 °C that showed no growth temperature dependence. From the XRD-RC and PL results, samples were identified for further characterization by XRD- RSM and TEM (Figures 6.6a, 6.6b, 6.6c). The results indicated that the films contained a near 1% Sn pseudomorphic layer along with a layer

that showed temperature dependence on incorporation. This temperature dependent layer

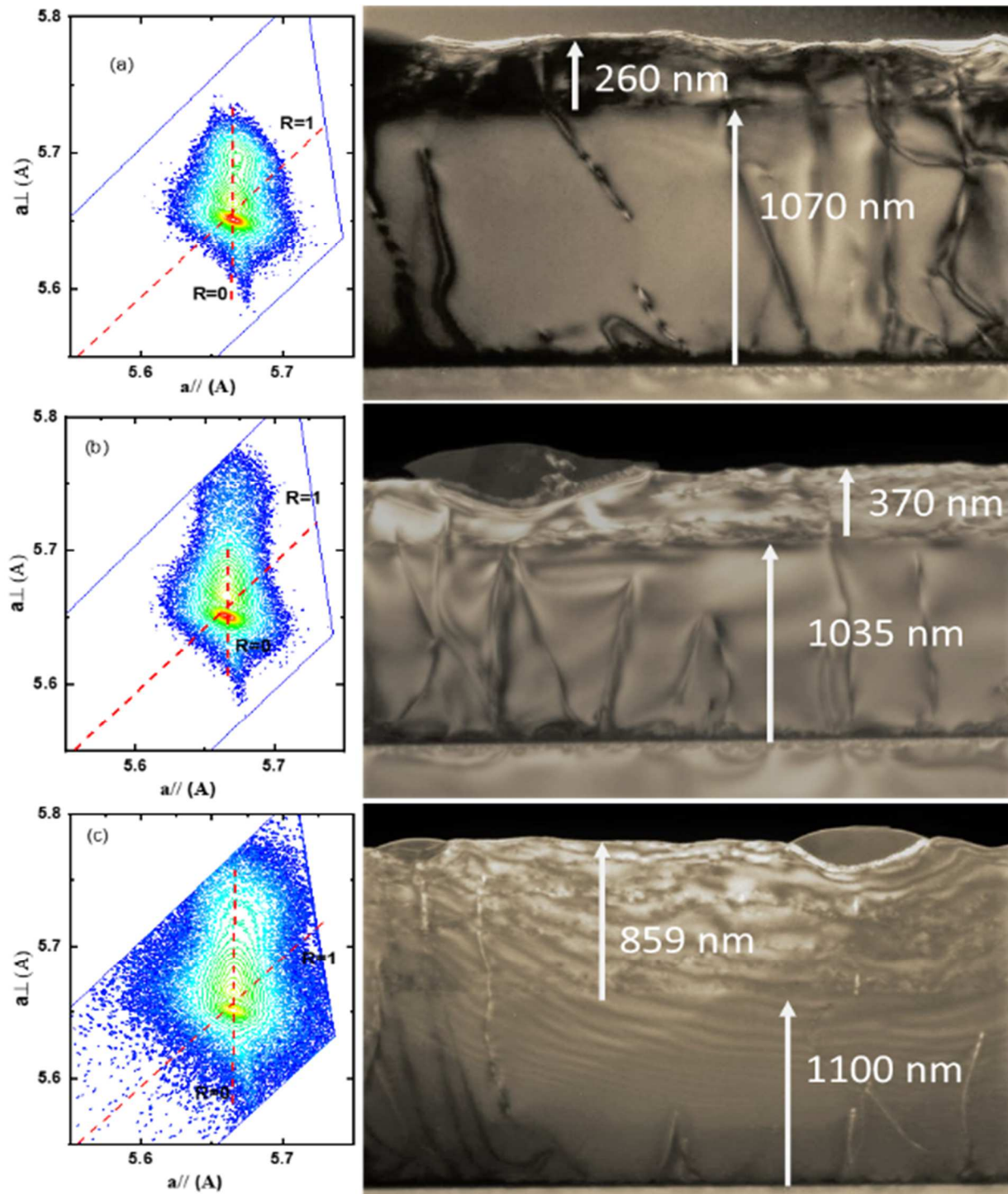


Figure 6.6: XRD-RSM plots with corresponding TEM images for samples grown for 30 min at (a) 300 °C, (b) 270 °C, and for 1 hr. at (c) 270 °C.

showed a maximum Sn incorporation in the range of 8%. Noted in the TEM imaging is that the surface of the films showed a surface segregation of Sn in the form of a droplet and a relatively consistent thickness of the Ge buffer layer in the range of 1000 to 1100 nm. The growths of 60 min were used to show no significant improvement in film quality or composition with significant change in the film thickness. Another series of growths using a fixed growth temperature of 270 °C were produced by reducing the SnCl<sub>4</sub> flow fraction from the level used in the first series of temperature dependent growths. The flow fraction of SnCl<sub>4</sub> was calculated to be 2.5 x 10<sup>-3</sup> using Equations 6.1 and 6.2.

$$Q \left( \frac{cm^3}{min} \right) * \rho \left( \frac{kg}{cm^3} \right) * \frac{1}{M} \left( \frac{mol}{kg} \right) = m \left( \frac{mol}{min} \right) \quad (\text{Equation 6.1})$$

where  $Q$  is the gas flow rate in  $\frac{cm^3}{min}$ ,  $\rho$  is the density of the gas precursor,  $\frac{1}{M}$  is the inverse of the molar mass of the precursor, and  $m$  is the molar flow rate of the precursor gas.

$$\frac{m_{SnCl_4}}{(m_{GeH_4} + m_{SnCl_4} + m_{Ar})} = mff_{SnCl_4} \quad (\text{Equation 6.2})$$

where  $m_{SnCl_4}$  is the molar flow rate of SnCl<sub>4</sub>,  $m_{GeH_4}$  is the molar flow rate of GeH<sub>4</sub>,  $m_{Ar}$  is the molar flow rate of Ar, and  $mff_{SnCl_4}$  is the molar flow fraction of SnCl<sub>4</sub>. The flow fraction of the first series of growths had a value that was orders of magnitude above that which has been reported for commercially grown high quality GeSn [45]. The SnCl<sub>4</sub> flow fraction was reduced in three steps from the first series of growths. The reductions in steps 1, 2, and 3 had values that were calculated to be 1.4 x 10<sup>-3</sup>, 4.5 x 10<sup>-4</sup>, and 2.3 x 10<sup>-4</sup>, respectively. These films, along with those of the first series, showed a cloudy surface that corresponded to the Sn segregation on the surface that could be visually observed to change to a shiny surface indicating a material quality improvement in surface segregation of the film. This visual inspection was also a good

indication the reduction in SnCl<sub>4</sub> was occurring. The visual inspection was not a verification there was no Sn segregation on the surface and further characterization was needed for confirmation. The SnCl<sub>4</sub> flow fraction of  $2.3 \times 10^{-4}$  was the limit to which SnCl<sub>4</sub> could be reduced using the current machine configuration. For further reductions another method will be discussed later in this section (Figure 6.7).

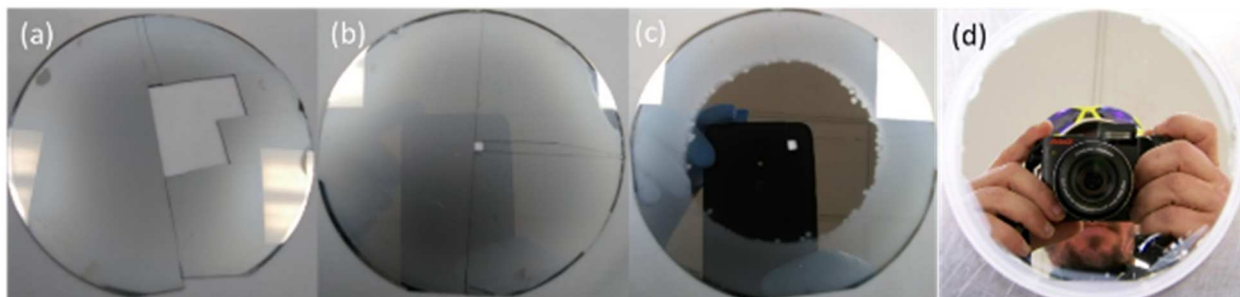


Figure 6.7: Images of samples grown with varying SiH<sub>4</sub> flow fractions of (a)  $2.5 \times 10^{-3}$ , (b)  $1.4 \times 10^{-3}$ , (c)  $4.5 \times 10^{-4}$ , and (d)  $2.3 \times 10^{-4}$ .

The results from the ellipsometry and Raman spectroscopy for the SnCl<sub>4</sub> reduction series of growths are shown in (Table 6.1). The PL results from this series of film growths showed there was no improvement in the PL spectra until the flow fraction for the SnCl<sub>4</sub> was in the range of mid  $10^{-4}$  shown in Figure 6.8. The PL results showed an improvement on the second set of growths in the series over that of the first set of growths which was similar in response to the initial comparison growth. The third growth of the series showed further improvement in peak intensity indicating improved material quality, however, it was noted that the peak position of the third growth was significantly shifted to shorter wavelengths. The shifting of the peak position to shorter wavelengths can be explained from an increase in compressive strain in the sample due to a reduced thickness as compared to the second growth as noted in Table 6.1.

To verify the incorporation changes of Sn in the grown films, XRD was performed on the samples and compared to the results of the initial SnCl<sub>4</sub> state from the first series of growths

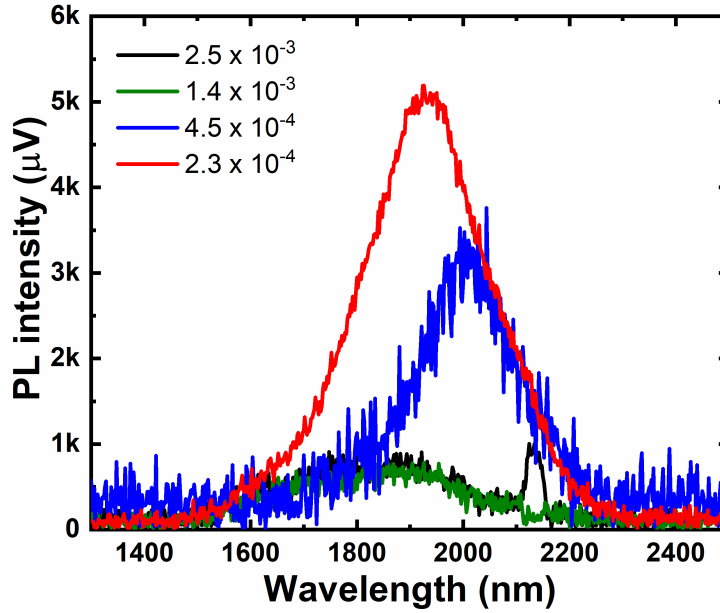


Figure 6.8: Photoluminescence plot of samples for each SnCl<sub>4</sub> flow fraction reduction.

(Figure 6.9). The results of the XRD-RC showed that the GeSn peak position of the samples were similar in position indicating that the Sn composition was very similar for the samples.

Table 6.1: Table of characterization results from Raman and ellipsometry.

Reduction step	SnCl <sub>4</sub> flow fraction	Ellipsometry thickness	Raman shift (Ge-Ge LO phonon)
Step 1	$2.5 \times 10^{-3}$	849 nm	$-1.0 \text{ cm}^{-1}$
Step 2	$1.4 \times 10^{-3}$	901 nm	$-2.0 \text{ cm}^{-1}$
Step 3	$4.5 \times 10^{-4}$	228 nm	$-2.0 \text{ cm}^{-1}$
Step 4	$2.3 \times 10^{-4}$	156 nm	$-1.0 \text{ cm}^{-1}$

This indicated that temperature, not SnCl<sub>4</sub> flow rate, was the driving factor in the amount of Sn composition for the films. The XRD-RC peak position for the GeSn peak also showed a reduction in the FWHM from the comparison growth in the first series to those growths with flow fractions in the range of  $\sim 10^{-4}$ .

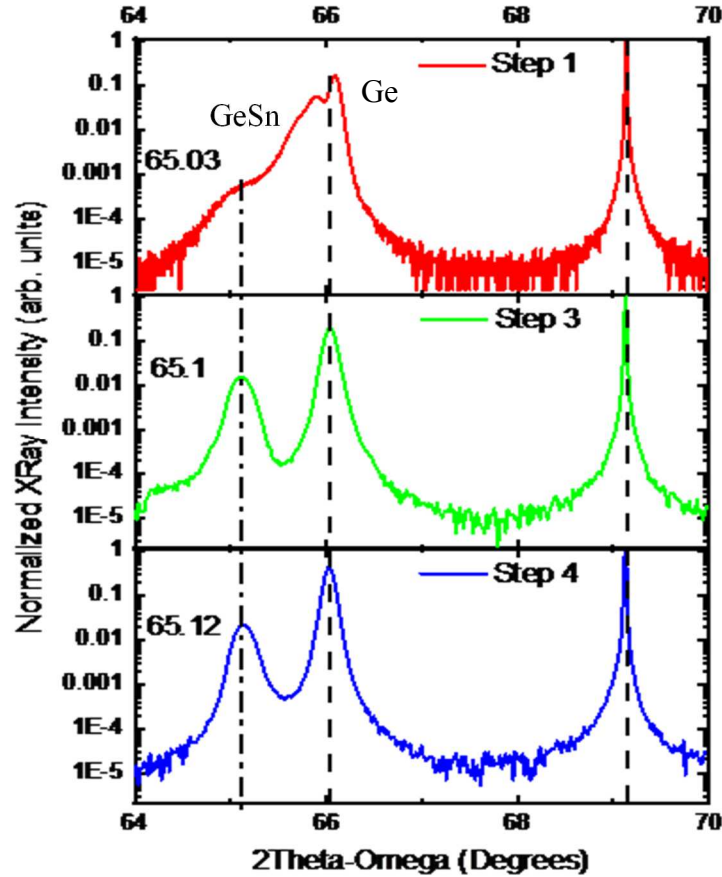


Figure 6.9: Comparison plots of XRD-RC data from growths using different  $\text{SnCl}_4$  flow fractions showing similar positions for GeSn peaks.

Further characterization was performed using scanning electron microscopy (SEM).

These images of the surface for the sample in the second series of growths showed that the size of the Sn droplets on the surface of the films reduced with each subsequent reduction in  $\text{SnCl}_4$  flow fraction. The size of these droplets reduced from  $\sim 3 \mu\text{m}$  to a size of  $< 1 \mu\text{m}$  as the  $\text{SnCl}_4$  flow rate reduced from  $2.5 \times 10^{-3}$  to  $2.3 \times 10^{-4}$  (Figure 6.10). This characterization indicated that at the machine limit of Sn precursor flow, there could be improvement in the Sn composition through a further reduction in temperature from the growth temperature of the second series.

A third series of growths was performed using the same flow rate, time, and pressure conditions of the second series of growths to increase the Sn composition of the grown film while maintaining the high material quality achieved during the second series of growths. These



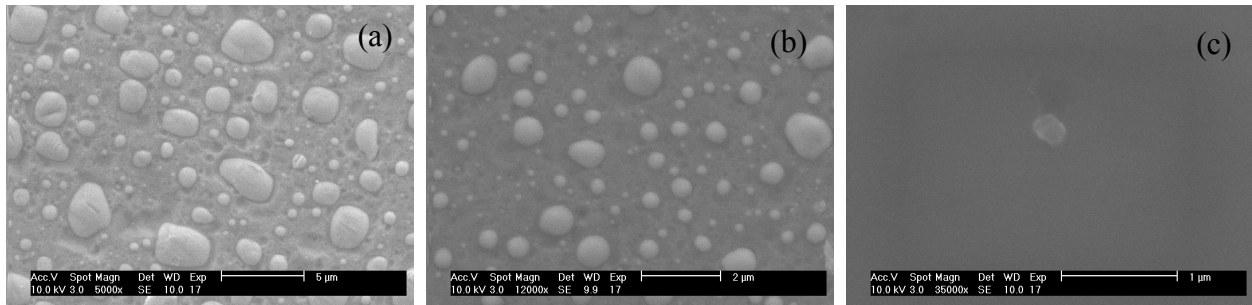


Figure 6.10: SEM imaging of sample surfaces from Sn flow fraction reduction test: a) cloudy surface from the initial state, b) hazy surface step 1, and c) clear surface from step 3.

growths lowered the growth temperature in subsequent steps of 10 °C from the growth temperature of 270 °C of the second series. These samples were characterized using ellipsometry, Raman spectroscopy, PL, and XRD as well as visual inspection. The initial visual inspection of the films indicated that the sample was increasing in Sn segregation in the surface as the temperature was further reduced indicating the need to further reduce the Sn precursor flow fraction beyond the current capabilities of the UHV-CVD system (Figure 6.11). The PL measurements for the sample showed an increase in wavelength as the growth temperature was

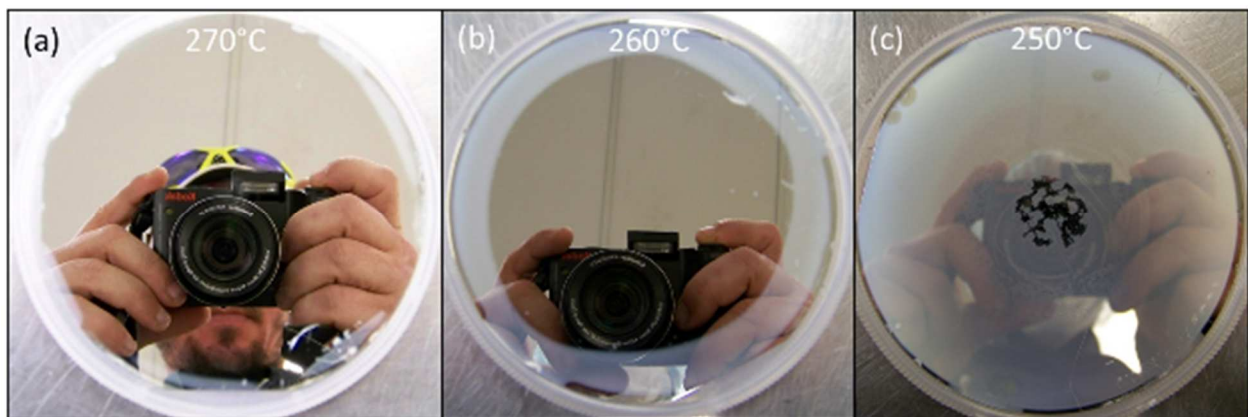


Figure 6.11. Images of sample grown using lowest SnCl<sub>4</sub> flow fraction showing the cloudy surface returning as temperature was decreased.

reduced indicating that the Sn composition of the films was increasing (Figure 6.12). The XRD-RC 2 $\theta$ - $\omega$  scans showed further evidence of increased composition of Sn as the GeSn peak



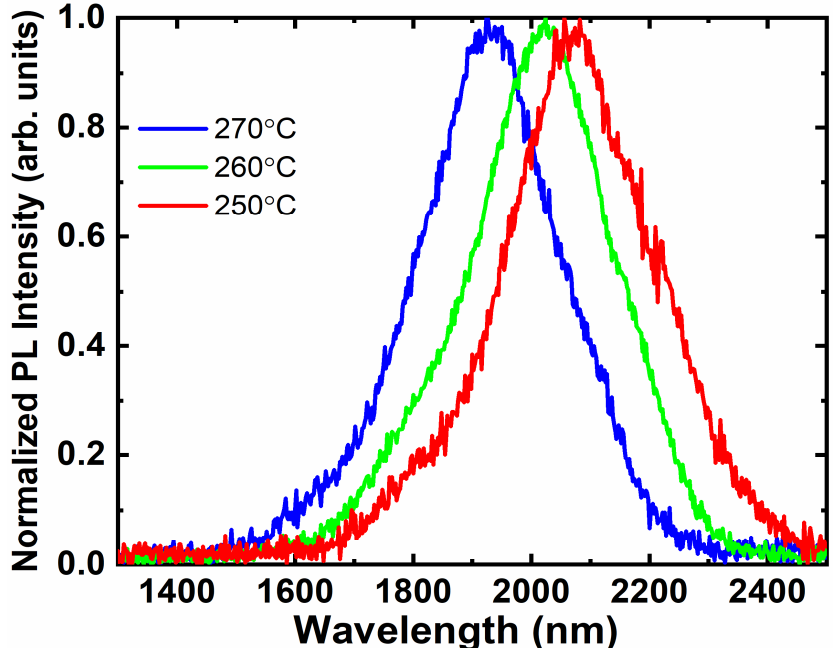


Figure 6.12: Normalized PL results from the temperature reduction growths.

position shifted lower. It was also noted an indication of a 1% compositional Sn layer in the plot for the 250 °C growth. The material quality of the grown films was shown to decrease when the layer of ~1% Sn returned as indicated by an increase in the FWHM of the films that shifted from a low of 1.55° for the 260 °C growth to 0.242° for the 250 °C growth (Figure 6.13).

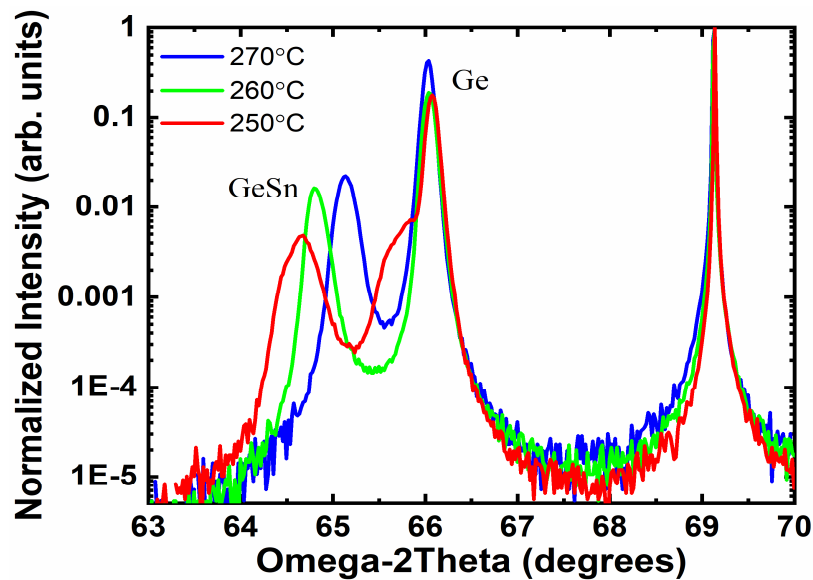


Figure 6.13: XRD-RC  $2\theta$ - $\omega$  scans of the temperature reduction growths.

## 6.4 Summary

The growth of the GeSn material system has been explored using a cold walled UHV-CVD reactor. These growths were produced directly on Si using a dilute Sn precursor mixture to provide a basis for subsequent growths. They were compared to Ge growths under the same conditions. The results of the comparison showed that the growth rate for GeSn directly on Si was increased over that of the Ge films by nearly 2x for the studied temperatures. The GeSn films produced room temperature photoluminescence that increased in intensity with a corresponding increase in growth thickness. The observation of the room temperature PL spectra was an indicator for higher relative material quality. The dilute GeSn films were compared to the Ge using XRD-RC. These results showed an increase in material quality for the GeSn films over that of the Ge materials for the same growth temperatures as evidenced by a reduction in the FWHM of the GeSn peak compared to the Ge peak. Reciprocal Space Map characterizations showed that the GeSn films were nearly fully relaxed. Subsequent growths on Ge buffered Si using the buffer recipe developed in Chapter 4 showed an increase in the PL wavelength and a shifting of the XRD-RC peak position to values of  $2\theta$ . These results indicated a temperature dependence on the composition of Sn as the PL peak position increased to longer wavelengths indicating increasing Sn composition. The XRD-RSM confirmed this by showing a temperature dependent layer with a maximum of ~8% Sn composition at a growth temperature of 270 °C. The TEM imaging of these samples showed that the buffer layers were relatively consistent in thickness and that Sn segregation was occurring on the surface of the films. A second series of GeSn growths showed that temperature was a driving factor for the incorporation of Sn as there was little change in the XRD-RC GeSn peak position between the growths. These films showed that a reduction in the SnCl<sub>4</sub> flow fraction would improve the material quality by reducing the

surface segregation for a single temperature. The growth of this series of films reached the limits of the configuration of the UHV-CVD system for the reduction of the SnCl<sub>4</sub> flow fraction. A final round of growths was explored to further increase the composition of Sn in the films. This was done by further reducing the growth temperature. These growths showed an increase in the Sn composition to ~ 10% while maintaining high quality until Sn segregation returned as the temperature was lowered. The compositional increase was confirmed using XRD-RC of the samples in the third series of growths. This return of the Sn segregation was attributed to the reduction in the decomposition rate of GeH<sub>4</sub> near the wafer surface resulting in a Sn overpressure condition.

## Chapter 7 Growth of SiGeSn

### 7.1 Introduction

The SiGeSn ternary alloy material system has gained much interest for silicon photonics for their CMOS compatibility and their independent band gap and lattice constant tunability [35][46][47]. This tuning capability by varying the Si and Sn composition of the alloy leads to optical properties that can be tailored for many different device applications [47]. The SiGeSn material system has the possibility for a type-I band alignment for the use in active devices [48]. This material system has been shown in efficient devices such as light sources [48][49], solar cells [50], transistors [51], quantum cascade lasers [52], photodiodes [53], and waveguides[54]. The solar cell applications have been of interest as the photodiodes using SiGeSn have shown collection efficiency of 75%, which exceeds that of state of the art InGaN devices. The ability to tune the band gap provides the ability to cover wavelengths from the near infrared to 12  $\mu\text{m}$  and beyond [55]. The property of the material to have both its band gap and lattice constants independently engineered would provide for the integration into a multijunction solar cell with a direct band gap energy of 1.0 eV and a lattice matching to that of GaAs. These engineered parameters would provide an increased efficiency while allowing for the introduction of Si substrates to a III-V junctioned solar cell [56][57]. The material also leads to CMOS compatibility with growth temperatures below 400  $^{\circ}\text{C}$  [58][57].

### 7.2 Growth matrix and results

The growth of SiGeSn has been explored using multiple techniques. This material system has been shown to be successfully grown using techniques such as UHV-CVD [59], MBE [60], and magnetron sputtering [58][61]. The success of these techniques does not lessen the difficulty of growths using this material system. Some of the issues with the growth of

SiGeSn include the low solubility <1% of Sn in Ge[62], the instability of  $\alpha$ -Sn at temperatures above 13 °C [23], and the surface energy difference of Si, Ge, and Sn [58]. Alloys of GeSn also have a thermodynamic instability that shows improvement with the addition of Si to form the ternary alloy [39]. The growth of SiGeSn has been accomplished in CVD growths using many different precursors such as SiGeH<sub>6</sub> [60] and SiGe<sub>2</sub>H<sub>8</sub> [59] along with SnD<sub>4</sub> as well as Si<sub>3</sub>H<sub>8</sub> [57]. More recently, SiGeSn has been produced using the precursors SiH<sub>4</sub>, GeH<sub>4</sub>, and SnCl<sub>4</sub> using both UHV-CVD and reduced pressure CVD (RPCVD) [47][63]. The planned growths for this section were produced by UHV-CVD using silane, germane, and stannic chloride. The single sample was grown on a p-type inch Si substrate that was prepared using the method described by Mosleh, et al [23]. The growth of more samples was planned, however, due to machine technical issues only one of these growths was completed. The growth was performed on Ge buffered Si using the buffer growth method previously discussed in Chapter 4. The planned growth matrix for the UHV-CVD SiGeSn growths was based on previous work for GeSn and SiGe on Si (100) (Table 5.2). The planned growth temperature ranged from 250 °C to 350 °C. The germane precursor and Ar carrier gas flow rates were fixed at 20 and 200 sccm, respectively, and the growth time was to be fixed at 60 minutes. The planned growth pressure was 2 Torr through the growth cycle. The SiH<sub>4</sub> flow rate was to be varied between 1 to 10 sccm.

The single UHV-CVD grown sample was characterized using visual inspection, ellipsometry, Raman spectroscopy and photoluminescence. The sample was produced using a temperature of 270 °C and a SiH<sub>4</sub> flow rate of 10 sccm. The visual inspection of the wafer showed a ring pattern of cloudy and shiny rings across that surface of the substrate(Figure 7.1). The ellipsometry fitting provided a film thickness of 2 nm on a Ge buffer of 1030 nm (Figure 7.2). The absorption cutoff wavelength was ~1700 nm. The plot of the absorption coefficient as



Figure 7.1: Image of SiGeSn sample showing "tree ring" pattern indicating competition for incorporation between Si and Sn.

a function of wavelength closely follows the plot for the Ge reference sample. The Raman spectroscopy data showed a Ge-Ge LO phonon wavenumber shift to  $298 \text{ cm}^{-1}$ . There was no indication from the Raman spectroscopy plot of Ge-Sn or Si-Ge LO phonons with this sample that could indicate poor material quality and segregation of Si and Sn in the material. The PL was measured at three points along the surface i) the center of the grown sample, ii)  $\sim 25 \text{ mm}$  from the sample edge, and iii)  $\sim 10 \text{ mm}$  from the sample edge (Figure 7.3). The PL data, Figure 7.4, showed that the peak position for the center of the sample was  $\sim 1724 \text{ nm}$  with an intensity

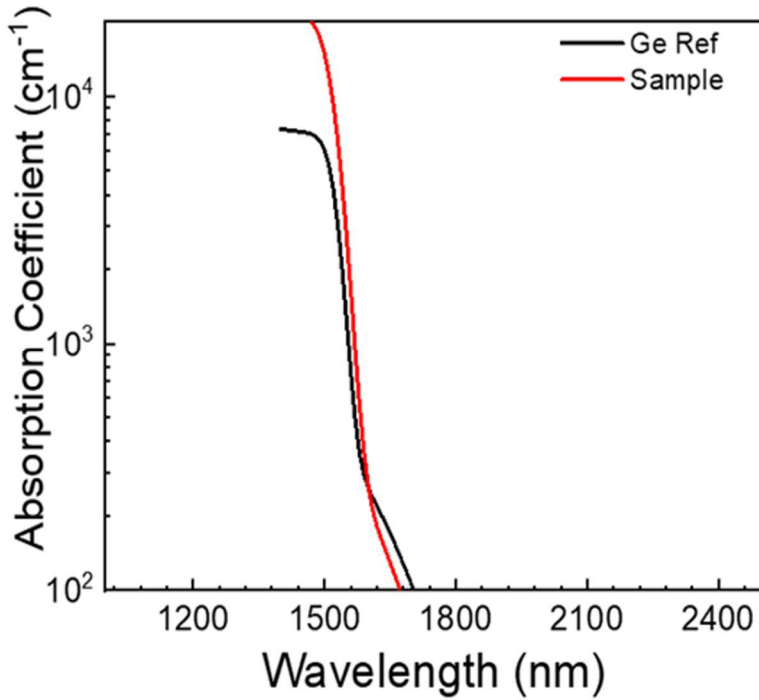


Figure 7.2: Absorption coefficient plot for SiGeSn on Ge buffered Si from ellipsometry measurements.

that was 1/62 of the direct peak intensity of the Ge reference sample. The second measured location (25 mm from the sample edge) provided a PL peak at ~ 1740 nm and an intensity that

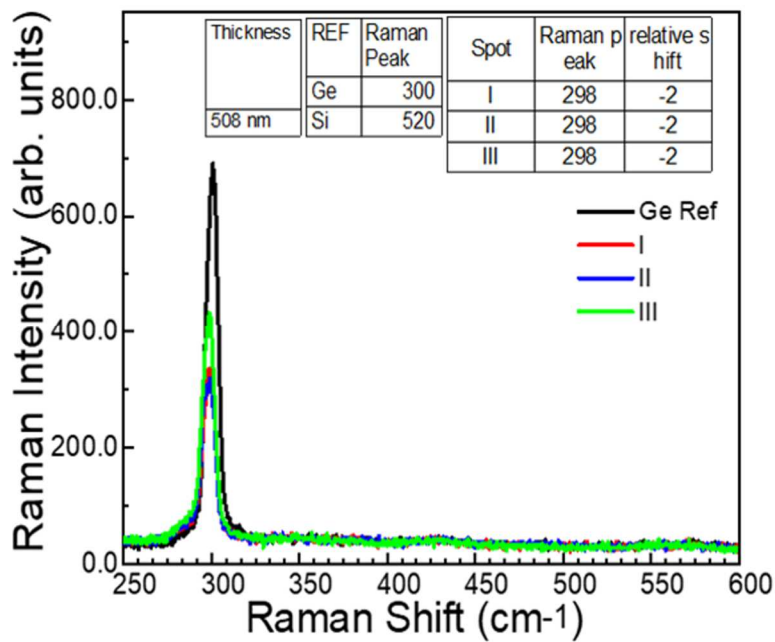


Figure 7.3: Typical Raman spectroscopy plot for SiGeSn on Ge buffered Si.

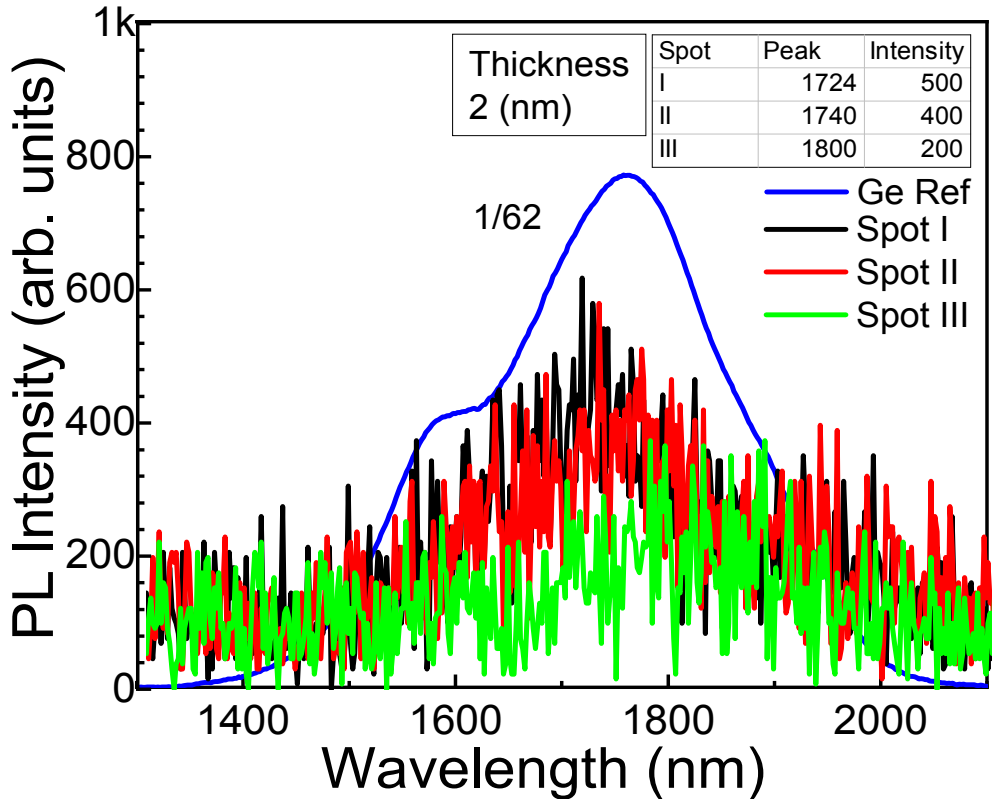


Figure 7.4: Typical PL plot for SiGeSn on Ge buffered Si.

was similar to that of the center position. The PL peak position of ~1800 nm was indicated at the outer measured position and this peak had a reduced intensity that was indicative of reduced material quality. The shifting of the outer peak could have been an indication of reduced Si composition resulting from Sn segregation in the film.



## Chapter 8 Conclusions and Future Work

### 8.1 Conclusions

The critical technologies for growth of the SiGeSn material system was investigated using UHV-CVD. The growths for the ternary alloy drew upon the knowledge gained through the growth of the base materials of Ge, SiGe, and GeSn. The Ge material growths were used to refine the growth recipes to narrow the growth window for the GeSn growths. From the Ge growths it was determined the growth rate at low temperatures ranged from 1 to 2.88 nm/min. These low growth rates were desirable for the 2-dimensional growth to prevent island formation in the film seed layer for Ge low temperature buffers. The growth of the high temperature Ge steps provided a high-quality material growth with sufficient growth rate that a Ge buffer layer of  $\sim 1.1 \mu\text{m}$  could be deposited with a TDD of  $\sim 1 \times 10^7 \text{ cm}^{-2}$  without an annealing step (and would be expected to improve using a high temperature insitu anneal). This TDD was within an order of magnitude of the TDD of optimized buffer layers that have been reported with an annealing step that are in the range of  $\sim 10^5$  to  $10^6 \text{ cm}^{-2}$ . Germanium-tin films were produced directly on Si substrates to compare the growth behavior of GeSn film to that of Ge. The fitting of the growth rates of the GeSn showed faster growth rates that ranged from 1.2 to 5.6 nm/min under near identical growth conditions as Ge films. However, the growth of GeSn took longer to initiate film growth. The GeSn films on Si produced PL at room temperature whereas, the equivalent Ge films did not.

The growth of SiGe was explored on multiple substrates. The growth was investigated across a temperature range from 450 °C to 600 °C, and varying SiH<sub>4</sub> flow rates. The growth rate for films varied between substrates with transition from gas phase transport to gas depletion noted for film on Si (100) grown at temperatures below 500 °C. Films grown on Si (111) and

sapphire (0001) indicated that the transition did not occur in the studied temperature range as the growth of SiGe was in the  $\langle 111 \rangle$  direction. The Raman spectroscopy results showed less shifting of the Ge-Ge LO phonon peak as the growth changed from SiGe  $\langle 100 \rangle$  to SiGe  $\langle 111 \rangle$ . Single crystalline material was indicated from x-ray diffraction results that showed material quality improvement as growth temperature increased for all substrates. A flow rate dependence was established for the molar fraction of Si in  $\text{Si}_x\text{Ge}_{1-x}$  films produced on sapphire substrates. Phi scans of SiGe on sapphire indicated a near equal distribution of crystalline twins with 60-degree rotations resulting in material defects.

The growth of GeSn on Ge buffered Si substrates was explored using UHV-CVD techniques. The films were grown using a temperature range of 325 °C to 240 °C and varying flow rates of stannic chloride. The results indicated that the Ge buffer recipe was repeatable yielding consistent thickness results that ranged from 1 to 1.1  $\mu\text{m}$ . The temperature dependence on Sn incorporation showed that the composition of Sn increased as temperature decreased. TEM imaging showed Sn segregation that reduced as the Sn flow fraction reduced and visual inspection showed that the surface became shiny from a cloudy condition. The flow fraction was reduced to the limits of the current configuration of the UHV-CVD system. The results of the GeSn growths showed that a narrow window for growth of high-quality material exists for a given temperature that is dependent on the Sn flow fraction.

The growth of SiGeSn was explored using UHV-CVD processes. The initial result showed the appearance of Sn and Si segregation. The Raman spectroscopy results showed no indication of Si-Ge or Ge-Sn LO phonons. The sample produced RT PL that indicated poor material quality and a peak shifting that indicated a possible difference of composition across the sample surface. The growth by RP-CVD of SiGeSn was compared to equivalent growths of

GeSn with similar Sn compositions. The results from ellipsometry, PL, and XRD-RC indicated that the introduction of Si to GeSn to form the ternary alloy increased the band gap of the alloy. This change in band gap energy was indicated by a reduction in absorption wavelength cutoff and PL wavelength. The addition of Si to form the SiGeSn alloy also changed the lattice parameters of the crystalline film as indicated by a positive shift in the  $2\theta$ - $\omega$  scans.

## 8.2 Future work

### 8.2.1 Improvement in material quality and composition

The improvement in material quality and Sn composition discussed in Chapter 4 reached the limits of the CVD system under its current configuration. To further improve the material quality and composition produced by the system would require further increases in the capacities of the mass flow controllers used for the germanium precursor and Ar carrier gas so as to further increase the flow fraction of  $\text{SnCl}_4$ . This would also necessitate a larger supply of germane or more frequent purchases of the current cylinder size. Another option would be to premix the precursors and carrier gas prior to injection into the CVD reactor. This could be accomplished using a gas mixing system such as the one in Figure 8.1. This gas mixing system would work by first injecting the  $\text{SnCl}_4$  into the mixing chamber to an indicated pressure. This would be followed by an injection of  $\text{GeH}_4$  into the chamber until a desired pressure is reached. The final injection of carrier gas would complete the process to reach a desired flow fraction. The mixing chamber would be continuously stirred with an impeller to ensure consistency of the gas mixture to be delivered to the reactor. Once the chamber is filled, the chamber would be closed and isolated while the delivery line is pumped to a pressure in the range of  $10^{-6}$  Torr so that a residual gas analyzer can be used to verify the composition of the mixture. Following the verification of the mixture composition the delivery line would be isolated from the turbo pump and the residual

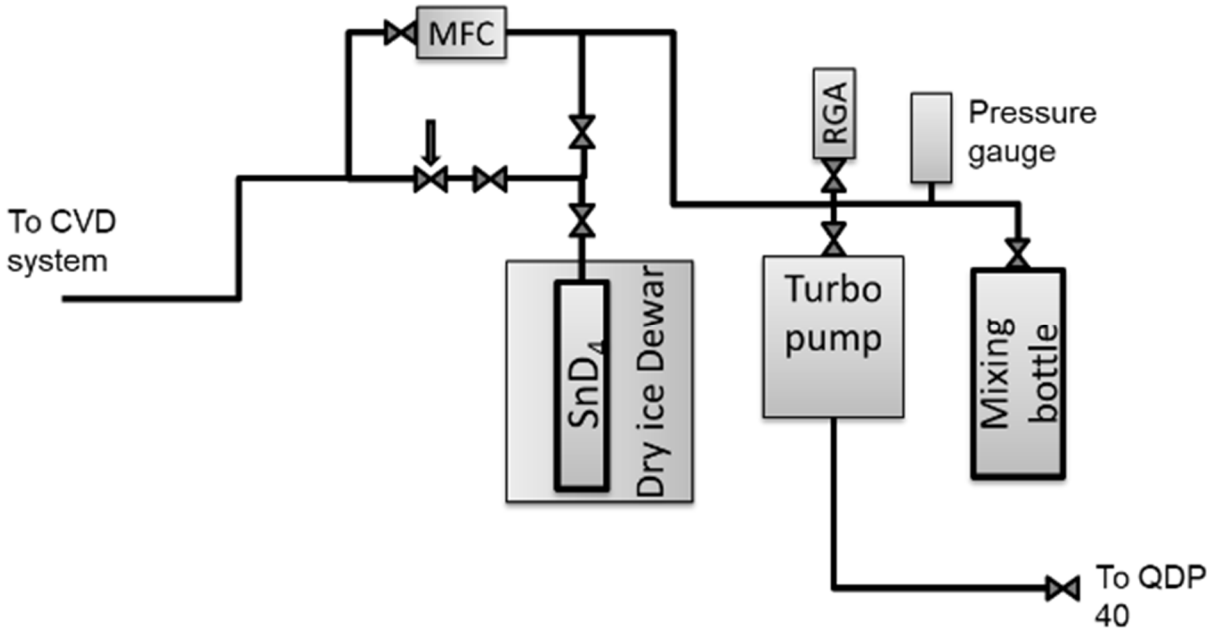


Figure 8.1. Schematic for the gas mixing system.

gas analyzer. The delivery line would then be reconnected to the mixing chamber by opening the isolation valve. The system would then flow the gas mixture back to the CVD system through an MFC to control the rate of injection into the reactor for growth rate control and process repeatability. This solution will be built to be used in future growths to improve material quality and Sn composition.

The gas mixing system would consist of an Edwards 75-XD turbo pump that will be backed by the UHV-CVD systems QDP40 corrosion resistant mechanical pump, a CC-10 pressure gauge, a Stanford Research Systems RGA 200 amu residual gas analyzer (RGA), a 10-inch stainless steel flanged nipple, 10-inch to 2.75 inch reducing flanges, 2.75 inch flanged magnetically coupled feed through, an internal custom impeller, a gear reduction stepper drive motor, a MKS mass flow controller, pneumatic bellows valves, and pneumatic solenoids. The system was designed to provide the ability to provide designed gas mixtures to the CVD reactor with a high degree of control and repeatability. The system will be controlled by electrical

switches to provide power to the pneumatic solenoids. The mixing bottle will be contained in a gas cabinet connected to the exhaust system to provide secondary containment of the system in case of system integrity failure.

### 8.2.2 Design and layout of system

The gas mixing system will use the 10-inch nipple as a mixing bottle. The bottom flange will be sealed using a 10 inch to 2.75 inch reducing flange. The 2.75-inch connection of the bottom flange will have the ½ inch magnetically coupled drive feed through mounted. This feed through will provide the drive connection from the custom four bladed impeller (Figure 8.2) to

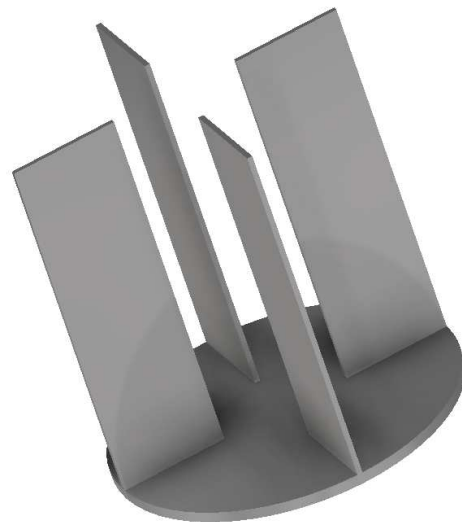


Figure 8.2: Image of custom designed impeller for the gas mixing system.

the gear reduction stepper motor. The stepper motor will provide a designed 40 to 60 revolutions per minute set using the drive controller provided with the stepper motor. The upper flange of the bottle will be sealed using a second reducing flange that is identical to the lower unit. The upper 2.75-inch port was designed to have a pneumatically operated 90° bellows valve that acts as the chamber isolation valve. The bellows valve will have a 2.75-inch tee that uses the offset flange for the mount of the CC-10 all range pressure gauge. The inline flange will be connected

to a 4-way tee that serves as the mounting flanges for the two 2.75-inch bellows isolation valves. The upper valve serves as the mounting connection for the (RGA). The lower isolation valve will be the mounting for the turbo pump. The inline flange of the 4-way tee will be sealed with a 2.75-inch to ¼ inch VCR connection intended to serve as the gas line connection from the mixing unit to the mass flow controller. The mass flow controller used in the initial design will require a differential pressure of a minimum 10 psi or 517 Torr. The mass flow controller from the initial design was evaluated to be insufficient for use in the gas mixing system due to its operating pressure requirements and a low differential pressure mass flow controller was researched and chosen to replace the original mass flow controller. The pressure requirements of the mass flow controller would result in the waste of large quantities of premixed gases. The new mass flow controller is designed to have a minimum operating differential pressure of 2 Torr this will result in a reduction of waste mixed gas. The selected all range pressure gauge has a maximum indicated pressure of 990 Torr and a minimum of  $10^{-9}$  Torr.

### **8.2.3 Operation and safety systems**

The gas mixing system will be controlled using electrical switches to send power to electrically control pneumatic valves that are connected to a nitrogen supply that is regulated to 40 psig. The solenoids send nitrogen to the pneumatic bellows and control valves provide mixed precursor gas flow control throughout the system. The system has a three-position electrical control switch wired to ensure that the feed valve and fill valve cannot both be open at the same time. The feed/fill interlock switch is needed due to the connection to the gas manifold of the CVD system being used to fill the gas mixing system with the individual precursor and carrier gases from the manifold. The feed valve will be connected to allow mixed gas from the mixing bottle to flow through the mass flow controller to the gas manifold prior to entry to the CVD

reactor. The turbo pump and RGA isolation valve will be closed prior to the filling of the system. The system will be filled, with the impeller rotating, by injecting each precursor gas individually based on calculations to a specific pressure indicated on the CC10 all range pressure gauge to reach desired gas ratios starting with stannic chloride due to its low vapor pressure at room temperature. The stannic chloride fill will be followed by the injection of germane which will be followed by the carrier gas. After the filling process is complete the feed/fill control will be switched to isolation and the gas bottle isolation valve closed. The section of the mixing system between the feed, fill and bottle isolation valves will be pumped in to the  $10^{-6}$  Torr range before the RGA isolation valve is opened. The RGA will be used to sample the gas mixture remaining to confirm the gas ratios in the gas mixing system prior to the start of the growth process. This measurement is to ensure repeatability and precise control over the gas ratios. Following the RGA measurement the RGA isolation valve will be closed and the turbo pump isolated by closing its isolation valve. The system will be placed in the growth condition by switching the feed/fill interlock to feed at the start of the growth cycle.

The safety systems of the gas mixing system include a gas cabinet that will be connected to the secondary containment exhaust system that provides air flow through the cabinet of ~ 400 cfm that is exhausted to atmosphere outside of the facility. The secondary containment system includes a toxic gas sensing module with a gas sensing cartridge installed for the precursor of the highest hazard rating. The gas sensing system will be tied to the building alarm system to provide audible and visual indications of a gas leak that is measured in parts per billion. The gas sensing modules will also be tied to valve interlocks that automatically close all stem valves and gate valves in the CVD and gas mixing systems to prevent excessive danger to the system, facility and lab occupants. The building alarms will also be tied to the outgoing alarms to notify

emergency response personnel to a detected leak condition.



## References

- [1] P. Seidenberg, "From Germanium to Silicon, A History of Change in the Technology of the Semiconductors," *Facet. New Perspect. Hist. Semicond.*, edited by A. Goldstein and W. Aspray (IEEE Center for the History of Electrical Engineering, New Brunswick, NJ), pp. 35–74, 1997.
- [2] M. E. Groenert, C. W. Leitz, A. J. Pitera, V. Yang, H. Lee, R. J. Ram, and E. A. Fitzgerald, "Monolithic integration of room-temperature cw GaAs/AlGaAs lasers on Si substrates via relaxed graded GeSi buffer layers," *J. Appl. Phys.*, vol. 93, no. 1, pp. 362–367, 2003.
- [3] P. Moontragoon, R. A. Soref, and Z. Ikonc, "The direct and indirect bandgaps of unstrained  $\text{SixGe}_{1-x-y}\text{Sny}$  and their photonic device applications," *J. Appl. Phys.*, vol. 112, no. 7, p. 073106, 2012.
- [4] N. Bhargava, M. Coppinger, J. Prakash Gupta, L. Wielunski, and J. Kolodzey, "Lattice constant and substitutional composition of GeSn alloys grown by molecular beam epitaxy," *Appl. Phys. Lett.*, vol. 103, no. 4, p. 041908, 2013.
- [5] T. Yamaha, O. Nakatsuka, S. Takeuchi, W. Takeuchi, N. Taoka, K. Araki, K. Izunome, and S. Zaima, "Growth and Characterization of Heteroepitaxial Layers of GeSiSn Ternary Alloy," *ECS Trans.*, vol. 50, no. 9, pp. 907–913, Mar. 2012.
- [6] F. Adar, S. Atzeni, R. Gilchrist, L. Goldstone, and J. Noonan, "Detector choice is vital to spectroscopy," *Laser Focus World*, no. April, 2002, <https://www.laserfocusworld.com/articles/print/volume-38/issue-4/features/detectors/detector-choice-is-vital-to-spectroscopy.html>, accessed 05-01-2019
- [7] W. H. Bragg and W. L. Bragg, "The Reflektion of X-rays by Crystals," *Proc. R. Soc. London. Ser. A, Contain. Pap. a Matheatical Phys. Character*, vol. 88, no. 605, pp. 428–438, 1913.
- [8] J. E. Bowers A. Ramaswamy, D. Dai, W. S. Zaoui, Y. Kang, T. Yin, and M. Morse, "Recent advances in Ge/Si PIN and APD photodetectors," *Phys. Status Solidi Curr. Top. Solid State Phys.*, vol. 7, no. 10, pp. 2526–2531, 2010.
- [9] S. B. Samavedam, M. T. Currie, T. A. Langdo, and E. a. Fitzgerald, "High-quality germanium photodiodes integrated on silicon substrates using optimized relaxed graded buffers," *Appl. Phys. Lett.*, vol. 73, no. 15, pp. 2125–2127, 1998.
- [10] J. Margetis, S. Al-Kabi, W. Du, W. Dou, Y. Zhou, T. Pham, P. Grant, S. Ghetmiri, A. Mosleh, B. Li, J. Liu, G. Sun, R. Soref, J. Tolle, M. Mortazavi, and S.-Q. Yu, "Si-Based GeSn Lasers with Wavelength Coverage of 2–3  $\mu\text{m}$  and Operating Temperatures up to 180 K," *ACS Photonics*, vol. 5, no. 3, pp. 827–833, 2017.

- [11] A. Mosleh, S. A. Ghetmiri, B. R. Conley, M. Hawkrige, M. Benamara, A. Nazzal, J. Tolle, S. Q. Yu, and H. A. Naseem, "Material characterization of  $\text{Ge}_{1-x}\text{Sn}_x$  alloys grown by a commercial CVD system for optoelectronic device applications," *J. Electron. Mater.*, vol. 43, no. 4, pp. 938–946, Apr. 2014
- [12] W. Dou, B. Alharthi, P. C. Grant, J. M. Grant, A. Mosleh, H. Tran, W. Du, M. Mortazavi, B. Li, H. A. Naseem, and S. Q. Yu, "Crystalline GeSn growth by plasma enhanced chemical vapor deposition," *Opt. Mater. Express*, vol. 8, no. 10, pp. 3220–3229, 2018
- [13] R. Roucka, J. Xie, J. Kouvetakis, J. Mathews, V. D'Costa, J. Menéndez, J. Tolle, and S.-Q. Yu "Ge<sub>1-y</sub>Sn<sub>y</sub> photoconductor structures at 1.55 $\mu\text{m}$ : From advanced materials to prototype devices," *J. Vac. Sci. Technol. B Microelectron. Nanom. Struct.*, vol. 26, no. 6, pp. 1952–1959, Nov. 2008.
- [14] R. Roucka, J. Tolle, C. Cook, A. V. G. Chizmeshya, J. Kouvetakis, V. D'Costa, J. Menendez, Zhihao D. Chen, and S. Zollner "Versatile buffer layer architectures based on  $\text{Ge}_{1-x}\text{Sn}_x$  alloys," *Appl. Phys. Lett.*, vol. 86, no. 2005, p. 191912, 2005.
- [15] G. Grzybowski, L. Jiang, J. Mathews, R. Roucka, C. Xu, R. T. Beeler, J. Kouvetakis, and J. Menéndez "Photoluminescence from heavily doped GeSn:P materials grown on Si(100)," *Appl. Phys. Lett.*, vol. 99, no. 17, pp. 171910-171910-3, Oct. 2011.
- [16] J. L. Liu, S. Tong, Y. H. Luo, J. Wan, and K. L. Wang, "High-quality Ge films on Si substrates using Sb surfactant-mediated graded SiGe buffers," *Appl. Phys. Lett.*, vol. 79, no. 21, p. 3431, 2001.
- [17] Y. Bogumilowicz, J. M. Hartmann, G. Rolland, and T. Billon, "SiGe high-temperature growth kinetics in reduced pressure-chemical vapor deposition," *J. Cryst. Growth*, vol. 274, no. 1–2, pp. 28–37, 2005.
- [18] J. Margetis, S. A. Ghetmiri, W. Du, B. R. Conley, A. Mosleh, R. A. Soref, G. Sun, L. Domulevich, H. A. Naseem, S.-Q. Yu, and J. Tolle, "Growth and Characterization of Epitaxial  $\text{Ge}_{1-x}\text{Sn}_x$  Alloys and Heterostructures Using a Commercial CVD System," *ECS Trans.*, vol. 64, no. 6, pp. 711–720, 2014.
- [19] M. Oehme, D. Widmann, K. Kostecki, P. Zaumseil, B. Schwartz, M. Gollhofer, R. Koerner, S. Bechler, M. Kittler, E. Kasper, and J. Schulze, "GeSn/Ge multiquantum well photodetectors on Si substrates.," *Opt. Lett.*, vol. 39, no. 16, pp. 4711–4714, 2014.
- [20] H. C. Luan D. R. Lim, K. K. Lee, K. M. Chen, J. G. Sandland, K. Wada, and L. C. Kimerling, "High-quality Ge epilayers on Si with low threading-dislocation densities," *Appl. Phys. Lett.*, vol. 75, no. 19, pp. 2909–2911, Nov. 1999.
- [21] V. Destefanis, J. M. Hartmann, A. Abbadie, A. M. Papon, and T. Billon, "Growth and structural properties of SiGe virtual substrates on Si(100), (110) and (111)," *J. Cryst. Growth*, vol. 311, no. 4, pp. 1070–1079, Feb. 2009.

- [22] E. A. Fitzgerald, Y.. Xie, M. L. Green, D. Brasen, A. R. Kortan, J. Michel, Y. Mii, and B. E. Weir, "Totally relaxed  $\text{Ge}_x\text{Si}_{1-x}$  layers with low threading dislocation densities grown on Si substrates," *Appl. Phys. Lett.*, vol. 59, no. 7, pp. 811–813, Aug. 1991.
- [23] A. Mosleh, M. A. Alher, L. C. Cousar, W. Du, S. A. Ghetmiri, T. Pham, J. M. Grant, G. Sun, R. A. Soref, B. Li, H. A. Naseem, and S.-Q. Yu, "Direct Growth of  $\text{Ge}_{1-x}\text{Sn}_x$  Films on Si Using a Cold-Wall Ultra-High Vacuum Chemical-Vapor-Deposition System," *Front. Mater.*, vol. 2, no. April, pp. 1–7, 2015.
- [24] J. M. Hartmann, A. Abbadie, and S. Favier, "Critical thickness for plastic relaxation of SiGe on Si(001) revisited," *J. Appl. Phys.*, vol. 110, no. 8, 2011.
- [25] R. Soref, D. Buca, and S.-Q. Yu, "Group IV Photonics," *Opt. Photonics News*, vol. 27, no. 1, pp. 32–39, 2016.
- [26] S. Q. Yu, S. A. Ghetmiri, W. Du, J. Margetis, Y. Zhou, A. Mosleh, S. Al-Kabi, A. Nazzal, G. Sun, R. A. Soref, J. Tolle, B. Li, and H. A. Naseem, "Si based GeSn light emitter : Mid-infrared devices in Si photonics," *Proc. SPIE 9367, Silicon Photonics X*, vol. 9367, no. February, p. 93670R, 2015.
- [27] S. Wirths, R. Geiger, N. von den Driesch, G. Mussler, T. Stoica, S. Mantl, Z. Ikonik, M. Luysberg, S. Chiussi, J. M. Hartmann, H. Sigg, J. Faist, D. Buca, and D. Grützmacher, "Lasing in direct-bandgap GeSn alloy grown on Si," *Nat. Photonics*, vol. 9, no. 2, pp. 88–92, 2015.
- [28] S. Al-Kabi, S. A. Ghetmiri, J. Margetis, T. Pham, Y. Zhou, W. Dou, B. Collier, R. Quinde, W. Du, A. Mosleh, J. Liu, G. Sun, R. A. Soref, J. Tolle, B. Li, M. Mortazavi, H. A. Naseem, and S. Q. Yu, "An optically pumped 2.5  $\mu\text{m}$  GeSn laser on Si operating at 110 K," *Appl. Phys. Lett.*, vol. 109, no. 17, p. 171105, Oct. 2016.
- [29] W. Du, Y. Zhou, S. A. Ghetmiri, A. Mosleh, B. R. Conley, A. Nazzal, R. A. Soref, G. Sun, J. Tolle, J. Margetis, H. A. Naseem, and S. Q. Yu., "Room-temperature electroluminescence from Ge/ $\text{Ge}_{1-x}\text{Sn}_x$ /Ge diodes on Si substrates," *Appl. Phys. Lett.*, vol. 104, no. 24, pp. 4–8, 2014.
- [30] J. Taraci, J. Tolle, J. Kouvetakis, M. R. McCartney, D. J. Smith, J. Menendez, and M. A. Santana, "Simple chemical routes to diamond-cubic germanium-tin alloys," *Appl. Phys. Lett.*, vol. 78, no. 23, pp. 3607–3609, 2001.
- [31] O. Gurdal, P. Desjardins, J. R. A. Carlsson, N. Taylor, H. H. Radamson, J.-E. Sundgren, and J. E. Greene, "Low-temperature growth and critical epitaxial thicknesses of fully strained metastable  $\text{Ge}_{1-x}\text{Sn}_x$  ( $x \leq 0.26$ ) alloys on  $\text{Ge}(001)2 \times 1$ ," *J. Appl. Phys.*, vol. 83, no. 1, p. 162, 1998.
- [32] R. Chen, H. Lin, Y. Huo, C. Hitzman, T. I. Kamins, and J. S. Harris, "Increased photoluminescence of strain-reduced, high-Sn composition Ge  $1-x\text{Sn}_x$  alloys grown by

- molecular beam epitaxy,” *Appl. Phys. Lett.*, vol. 99, no. 18, pp. 2013–2016, Oct. 2011.
- [33] J. Werner, M. Oehme, M. Schmid, M. Kaschel, A. Schirmer, E. Kasper, and J. Schulze, “Germanium-tin p-i-n photodetectors integrated on silicon grown by molecular beam epitaxy,” *Appl. Phys. Lett.*, vol. 98, no. 6, pp. 2011–2014, Feb. 2011.
- [34] M. Coppinger, J. Hart, N. Bhargava, S. Kim, and J. Kolodzey, “Photoconductivity of germanium tin alloys grown by molecular beam epitaxy,” *Appl. Phys. Lett.*, vol. 102, no. 14, pp. 2013–2016, 2013.
- [35] J. Kouvetakis and A. V. G. G. Chizmeshya, “New classes of Si-based photonic materials and device architectures via designer molecular routes,” *J. Mater. Chem.*, vol. 17, no. 17, p. 1649, 2007.
- [36] B. R. Conley, A. Mosleh, S. A. Ghetmiri, W. Du, R. A. Soref, G. Sun, J. Margetis, J. Tolle, H. a Naseem, and S.-Q. Yu, “Temperature dependent spectral response and detectivity of GeSn photoconductors on silicon for short wave infrared detection,” *Opt. Express*, vol. 22, no. 13, pp. 15639–52, 2014.
- [37] S. Wirths, D. Buca, G. Mussler, A. T. Tiedemann, B. Hollander, P. Bernardy, T. Stoica, D. Grutzmacher, and S. Mantl, “Reduced Pressure CVD Growth of Ge and Ge<sub>1-x</sub>Sn<sub>x</sub> Alloys,” *ECS J. Solid State Sci. Technol.*, vol. 2, no. 5, pp. N99–N102, 2013.
- [38] R. Roucka, R. Beeler, J. Mathews, M. Ryu, Yung K. Yeo, J. Menéndez, and J. Kouvetakis, “Complementary metal-oxide semiconductor-compatible detector materials with enhanced 1550 nm responsivity via Sn-doping of Ge/Si(100),” *J. Appl. Phys.*, vol. 109, no. 10, p. 103115, May 2011.
- [39] L. Jiang, C. Xu, J. D. Gallagher, R. Favaro, T. Aoki, J. Menéndez, and J. Kouvetakis, “Development of light emitting group IV ternary alloys on Si platforms for long wavelength optoelectronic applications,” *Chem. Mater.*, vol. 26, pp. 2522–2531, 2014.
- [40] C. L. Senaratne, J. D. Gallagher, L. Jiang, T. Aoki, D. J. Smith, J. Menéndez, and J. Kouvetakis, “Ge<sub>1-y</sub>Sn<sub>y</sub> (y = 0.01-0.10) alloys on Ge-buffered Si: Synthesis, microstructure, and optical properties,” *J. Appl. Phys.*, vol. 116, no. 13, p. 133509, 2014.
- [41] J. Mathews, Z. Li, Y. Zhao, J. D. Gallagher, I. Agha, J. Menéndez, and J. Kouvetakis, “Toward GeSn lasers: Light Amplification and Stimulated Emission in GeSn Waveguides at Room Temperature,” *ECS Transactions*, vol. 75, no. 8, pp. 163–176, 2016.
- [42] B. Vincent, F. Gencarelli, H. Bender, C. Merckling, B. Douhard, D. H. Petersen, O. Hansen, H. H. Henrichsen, J. Meererschaut, W. Vandervorst, M. Heyns, R. Loo, and M. Caymax, “Undoped and in-situ B doped GeSn epitaxial growth on Ge by atmospheric pressure-chemical vapor deposition,” *Appl. Phys. Lett.*, vol. 99, no. 15, p. 152103, 2011.
- [43] S. A. Ghetmiri, W. Du, J. Margetis, A. Mosleh, L. Cousar, B. R. Conley, L. Domulevicz,

- A. Nazzal, G. Sun, R. A. Soref, J. Tolle, B. Li, H. A. Naseem, and S.-Q. Yu, "Direct-bandgap GeSn grown on silicon with 2230 nm photoluminescence," *Appl. Phys. Lett.*, vol. 105, no. 15, 2014.
- [44] W. Dou, Y. Zhou, J. Margetis, S. A. Ghetmiri, S. Al-Kabi, W. Du, J. Liu, G. Sun, R. A. Soref, J. Tolle, B. Li, M. Mortazavi, and S. Q. Yu., "Optically pumped lasing at 3  $\mu\text{m}$  from compositionally graded GeSn with tin up to 22.3%," *Opt. Lett.*, vol. 43, no. 19, p. 4558, Oct. 2018.
- [45] J. Margetis, A. Mosleh, S. Al-Kabi, S. A. Ghetmiri, W. Du, W. Dou, M. Benamara, B. Li, M. Mortazavi, H. A. Naseem, S. Q. Yu, and J. Tolle, "Study of low-defect and strain-relaxed GeSn growth via reduced pressure CVD in  $\text{H}_2$  and  $\text{N}_2$  carrier gas," *J. Cryst. Growth*, vol. 463, pp. 128–133, 2017.
- [46] R. Soref, "Emerging SiGeSn integrated-photonics technology," *2016 IEEE Photonics Soc. Summer Top. Meet. Ser. SUM 2016*, vol. 3, pp. 100–101, 2016.
- [47] A. Mosleh, M. Alher, W. Du, L. Cousar, S.A. Ghetmiri, S. Al-Kabi, W. Dou, P. Grant, G. Sun, R. Soref, B. Li, H. Naseem, and S. Q. Yu, " $\text{Si}_y\text{Ge}_{1-x-y}\text{Sn}_x$  films grown on Si using a cold-wall ultrahigh-vacuum chemical vapor deposition system," *J. Vac. Sci. Technol. B, Nanotechnol. Microelectron. Mater. Process. Meas. Phenom.*, vol. 34, no. 1, p. 011201, Jan. 2016.
- [48] J. Menéndez and J. Kouvetakis, "Type-I  $\text{Ge}/\text{Ge}_{1-x-y}\text{Si}_x\text{Sn}_y$  strained-layer heterostructures with a direct Ge bandgap," *Appl. Phys. Lett.*, vol. 85, no. 7, pp. 1175–1177, Aug. 2004.
- [49] G. Sun, R. A. Soref, H. H. Cheng, G. Sun, R. A. Soref, and H. H. Cheng, "Design of an electrically pumped SiGeSn / GeSn / SiGeSn double-heterostructure midinfrared laser Design of an electrically pumped SiGeSn / GeSn / SiGeSn double- heterostructure midinfrared laser," vol. 033107, no. 2010, 2016.
- [50] Y.-Y. Fang, J. Xie, J. Tolle, R. Roucka, V. R. D'Costa, A. V. G. Chizmeshya, Jose Menendez, and John Kouvetakis, "Molecular-based synthetic approach to new group IV materials for high-efficiency, low-cost solar cells and Si-based optoelectronics.," *J. Am. Chem. Soc.*, vol. 130, no. 47, pp. 16095–16102, 2008.
- [51] S. Wirths, A. T. Tiedemann, Z. Ikonik, P. Harrison, B. Holländer, T. Stoica, G. Mussler, M. Myronov, J. M. Hartmann, D. Grützmacher, D. Buca, and S. Mantl, "Band engineering and growth of tensile strained Ge/(Si)GeSn heterostructures for tunnel field effect transistors," *Appl. Phys. Lett.*, vol. 102, no. 19, p. 192103, 2013.
- [52] G. Sun, H. H. Cheng, J. Menéndez, J. B. Khurgin, and R. A. Soref, "Strain-free Ge/GeSiSn quantum cascade lasers based on L-valley intersubband transitions," *Appl. Phys. Lett.*, vol. 90, no. 2007, pp. 23–25, 2007.
- [53] R. T. Beeler, D. J. Smith, and J. Kouvetakis, "GeSiSn Photodiodes With 1eV Optical

- Gaps Grown,” *IEEE Journal of Photovoltaics*, vol. 2, no. 4, pp. 434–440, 2012.
- [54] R. Soref, “Silicon-based silicon-germanium-tin heterostructure photonics,” *Philos. Trans. R. Soc. A Math. Phys. Eng. Sci.*, vol. 372, no. 2012, pp. 20130113–20130113, Feb. 2014.
- [55] R. Soref, “Towards Silicon-based Longwave Integrated Optoelectronics ( LIO ),” *SPIE Photonics West*, vol. 6898, no. 0704, p. 14, 2008.
- [56] S. Essig, M. Steiner, C. Allebé, J. Geisz, B. Paviet-Salomon, S. Ward, A. Descoeurdes, V. LaSalvia, L. Barraud, N. Badel, A. Faes, J. Levrat, M. Despeisse, C. Ballif, P. Stradins, and D. Young, “Realization of GaInP/Si Dual-Junction Solar Cells With 29.8% 1-Sun Efficiency,” *IEEE J. Photovoltaics*, vol. 6, no. 4, pp. 1012–1019, Jul. 2016.
- [57] V. R. D’Costa, Y. Y. Fang, J. Tolle, J. Kouvetakis, and J. Menéndez, “Tunable optical gap at a fixed lattice constant in group-IV semiconductor alloys,” *Phys. Rev. Lett.*, vol. 102, no. 10, pp. 1–4, 2009.
- [58] J. Zheng, S. Wang, T. Zhou, Y. Zuo, B. Cheng, and Q. Wang, “Single-crystalline  $\text{Ge}_{1-x-y}\text{Si}_x\text{Sn}_y$  alloys on Si (100) grown by magnetron sputtering,” *Opt. Mater. Express*, vol. 5, no. 2, p. 287, 2015.
- [59] P. Aella, C. Cook, J. Tolle, S. Zollner, A. V. G. Chizmeshya, and J. Kouvetakis, “Optical and structural properties of  $\text{Si}_x\text{Sn}_y\text{Ge}_{1-x-y}$  alloys,” *Appl. Phys. Lett.*, vol. 84, no. 6, pp. 888–890, Feb. 2004.
- [60] M. Bauer, C. Ritter, P. A. Crozier, J. Ren, J. Menendez, G. Wolf, and J. Kouvetakis, “Synthesis of ternary SiGeSn semiconductors on Si(100) via  $\text{Sn}_x\text{Ge}_{1-x}$  buffer layers,” *Appl. Phys. Lett.*, vol. 83, no. 11, pp. 2163–2165, Sep. 2003.
- [61] J. Zheng, L. Li, T. Zhou, Y. Zuo, C. Li, B. Cheng, and Q. Wang, “Growth of Crystalline  $\text{Ge}_{1-x}\text{Sn}_x$  Films on Si (100) by Magnetron Sputtering,” *ECS Solid State Lett.*, vol. 3, no. 9, pp. P111–P113, Jul. 2014.
- [62] C. D. Thurmond, F. A. Trumbore, and M. Kowalchik, “Germanium Solidus Curves,” *J. Chem. Phys.*, vol. 25, no. 4, pp. 799–800, Oct. 1956.
- [63] B. Alharthi, J. Margetis, H. Tran, S. Al-kabi, W. Dou, S. A. Ghetmiri, A. Mosleh, J. Tolle, W. Du, M. Mortazavi, B. Li, H. Naseem, and S.-Q. Yu “Study of material and optical properties of  $\text{Si}_x\text{Ge}_{1-x-y}\text{Sn}_y$  alloys for Si-based optoelectronic device applications,” *Opt. Mater. Express*, vol. 7, no. 10, p. 3517, Oct. 2017.

## **Appendix A: Description of Research for Popular Publication**

The revolution in electronics that began with the solid-state transistor has seen electronic devices not only advance but become an integral part of everyday life. There is nearly worldwide coverage of electronic devices from cell phones and wearable electronics to medical equipment and transportation. One segment of these electronic devices that have expanded into our daily lives is optoelectronics. These light producing or detecting devices can be found in cameras, TV remotes, safety systems, and fiber optics systems that have revolutionized the speed and capacity at which information can be shared. This type of device can operate in wavelengths from the ultraviolet to the infrared including the visible light ranges that we can see. The infrared wavelengths are beyond what our eyes can detect and are used by devices for fiber optic communications, communication with spacecraft, and safety sensors such as motion detectors and gas sensors.

Since its introduction, silicon has been the main basis for most of the electronic devices found in today's society. More than 70 years of progress has led to systems that are smaller and more powerful in order to keep up with the demands from the individuals who use them. This, however, is a problem for silicon which has poor optical material properties when compared to materials such as indium-gallium-arsenide which is one of many III-V materials preferred by the optoelectronics industry. Many of these materials are expensive to produce even though they are highly efficient light producers and receivers. This efficiency has led to silicon-based optoelectronic devices to fall behind in the consumer market. One solution to try and improve the competitiveness of silicon-based devices is to create hybrid devices using a III-V material on a silicon substrate. This, however, has been problematic as the III-V material is typically incompatible with silicon processing methods. Another solution is to develop devices and device

structures from group IV materials, which are found in the same column on the periodic table of elements as silicon, for the infrared wavelengths. In recent decades, researches have made a concerted effort to develop optoelectronic devices made of silicon and germanium, though due to silicon's poor electrical properties limits the efficiency of such devices. Germanium, however, can become a direct band-gap material when placed in a tensile strain condition though the wavelength range of operation is limited.

At the University of Arkansas, Joshua M. Grant, a Microelectronics -Photonics student of Dr. Shui-Qing (Fisher) Yu of the Electrical Engineering department, has recently worked on research to clear some of the hurdles needed to bring the next generation of infrared materials and devices to everyday life by investigating the technologies that make these advancements possible. Mr. Grant has said, "Imagine an infrared camera in your phone, now there are no more dark parking lots, no more dark alleys, nothing hides anymore. Now, consider if it will fit in your cell phone, where else can the device go. One place could be in the front of your car so that it enables you to see the deer standing on the side of the road that your headlights missed before it totals out your ride and leaves you stranded in the middle of nowhere." Achieving a direct band-gap material with the benefits of a III-V material has been shown in group IV materials by alloying germanium and tin. This alloy material system has the ability to cover the same wavelength spectrum as traditional III-V materials but has the advantage of being compatible with the processing methods used for silicon devices and can easily be integrated to a silicon substrate.

There have been several reported devices made from the material alloys of germanium and tin such as lasers and light emitting diodes as well as photoconductors and photodiodes that show promise to reach efficiencies near that of some traditional III-V based devices. These



results have shown that germanium-tin alloys could compete in the market with the traditional infrared materials and offer the advantage of a sizeable reduction in cost due to standardized and well understood silicon processing methods. These processing methods have the ability to produce a chipset for a digital camera which could fit in a cellular phone effectively bringing true night vision technology to the masses. The processes that produce the materials can be quite complicated. “One method,” Mr. Grant said, “uses solid materials that are heated to extremely high temperatures and the material is evaporated and sent towards the substrate that the material is to be grown upon. This is the simplest way I can describe molecular beam epitaxy or MBE for short. Another method for producing these materials is through using gas sources that are mixed and injected into a vacuum chamber and then use temperature and pressure to break apart the gases and deposit the targeted material onto the substrate to grow a single crystal material which is the simplistic way to describe chemical vapor deposition or CVD.” The materials grown by MBE tend to be costlier to produce as compared to their chemical vapor deposition counterparts. This has led to the development of cheap, commercially available source gases for the CVD method which in turn translates into cost efficient materials.

Through the use of this technology the ability to save and protect lives can become more cost effective, enabling disaster volunteers and emergency personnel a tool at their disposal that would not be affected by dust, smoke, or fog without burdening these individuals or their respective companies with the high cost of current quality infrared equipment. Mr. Grant said “This could allow for more personnel and volunteers available to respond to a disaster when the need arises. An example that I can think of was the World Trade Center collapse in 2001 and seeing the dust cloud and smoke immediately following the collapse.” Another benefit of infrared technology is in the diagnosis and treatment of internal injuries as a result of an

accident. The ability for some internal injuries to be detected under infrared light allows emergency responders to identify internal injuries and provides one more piece of information in the treatment of a patient at the scene. Another benefit for this technology would be in the computing and data industries. Current methods for storing transmitting and processing data is done using electronic devices. These devices use chipsets that require various means of cooling such as fans, and even liquid cooling, to dissipate the heat that is generated due to the resistance of the wires and connections in the chipset. Replacing the wires and connections using optical waveguides and on-chip infrared optoelectronic lasers and detectors that are silicon-based to transfer the information instead of electrons, the cooling requirements would be reduced lending to more power efficient systems. Mr. Grant said, “Think of fiber optic lines that run your internet except inside the chips of your computer allowing all of the necessary communications to occur at the speed of light.”

## **Appendix B: Executive Summary of Newly Created Intellectual Property**

Newly created intellectual property is as follows:

- i) Plasma enhanced UHV-CVD growth of GeSn directly on silicon or germanium buffered silicon substrates.
- ii) Use of the proposed gas mixing system to precisely control the gas flow fraction for SnCl<sub>4</sub> to increase Sn content as the growth temperature is reduced

## **Appendix C: Potential Patent and Commercialization Aspects of Listed Intellectual Property Item**

### **C.1 Patentability of Intellectual Property (Could Each Item be Patented)**

Each piece of the intellectual property was examined to determine its patentability.

- i) The plasma enhanced system could be patented.
- ii) The gas mixing for precise control could be patented.

### **C.2 Commercialization Prospects (Should Each Item Be Patented)**

- i) No, the method of plasma enhancement could easily be replicated or even modified as plasma enhancement is used in different variations and has been available for other processes in commercial applications.
- ii) No, precise control of gas ratios is well understood and available on commercial processes that have larger precursor supplies available and larger mass flow controllers.

### **C.3 Possible Prior Disclosure of IP**

- i) Not applicable.
- ii) Not applicable.

## **Appendix D: Broader Impact of Research**

### **D.1 Applicability of Research Methods to Other Problems**

The availability of the (Si)GeSn material system could be a disruptive technology within the infrared materials market. The methods used to research the technologies involved in developing these materials could be useful in finding solutions to other issues as well. One of the methods used for this that was most helpful was the same day feedback of characterization data that was obtained for each sample that provided information on the sample's visual surface appearance, thickness, composition, and quality. This feedback was collected and documented in both hardcopy and softcopy formats in multiple locations for quick reference. Those samples that showed results that were of interest had further characterization performed on them using more in-depth methods. This method of rapid feedback allowed for team members to share the collected information among themselves and allowed for the research to progress toward the desired goals by being able to adjust growths early without wasting sample growths while waiting for the data from an earlier growth.

### **D.2 Impact of Research Results on U.S. and Global Society**

The impact of the (Si)GeSn material system could have a great impact on the U.S. and global society. The infrared optoelectronics market has been dominated by III-V materials for decades though their integration into mass markets has been limited due to their high cost. The development of group IV materials, such as GeSn, on silicon substrates has the potential to reduce the cost of these devices by 50%. Throughout the world cellphones, personal electronics, and computers have become so common it is more shocking to find someone without than with these items.

GeSn material on Si has been reported to show the necessary characteristics needed to

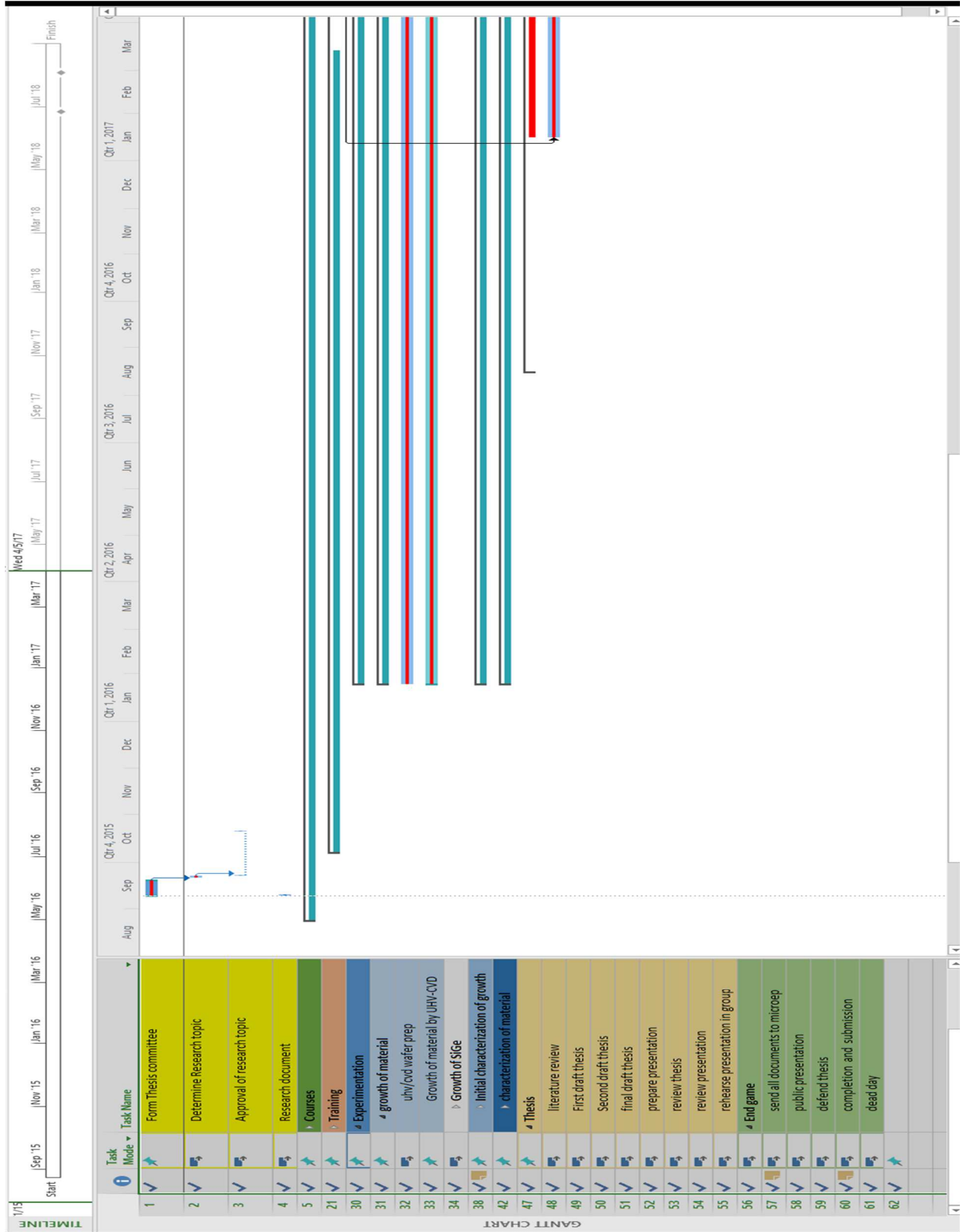
facilitate the on-chip transfer of data optically. This would allow for the devices and systems that use chipsets with this optical integration to operate faster with less power thereby increasing their efficiency while reducing the power requirements on the global energy grids. This reduction in power requirements would lead to a reduction in the demand for the fuels that are currently used to produce that power like coal, natural gas, and oil. Infrared optical devices using GeSn would also allow for vision in the night, through smoke and in fog. This would allow for safer travel in these conditions and allow for better response from emergency personnel during a time of disaster. These types of devices could also be applied to new self-driving vehicles to allow for better safety by leading to the ability to discern the environment around the vehicle in these types of conditions. This gives devices using the GeSn material the potential to disrupt the infrared market with efficient and inexpensive devices.

### **D.3 Impact of Research Results on the Environment**

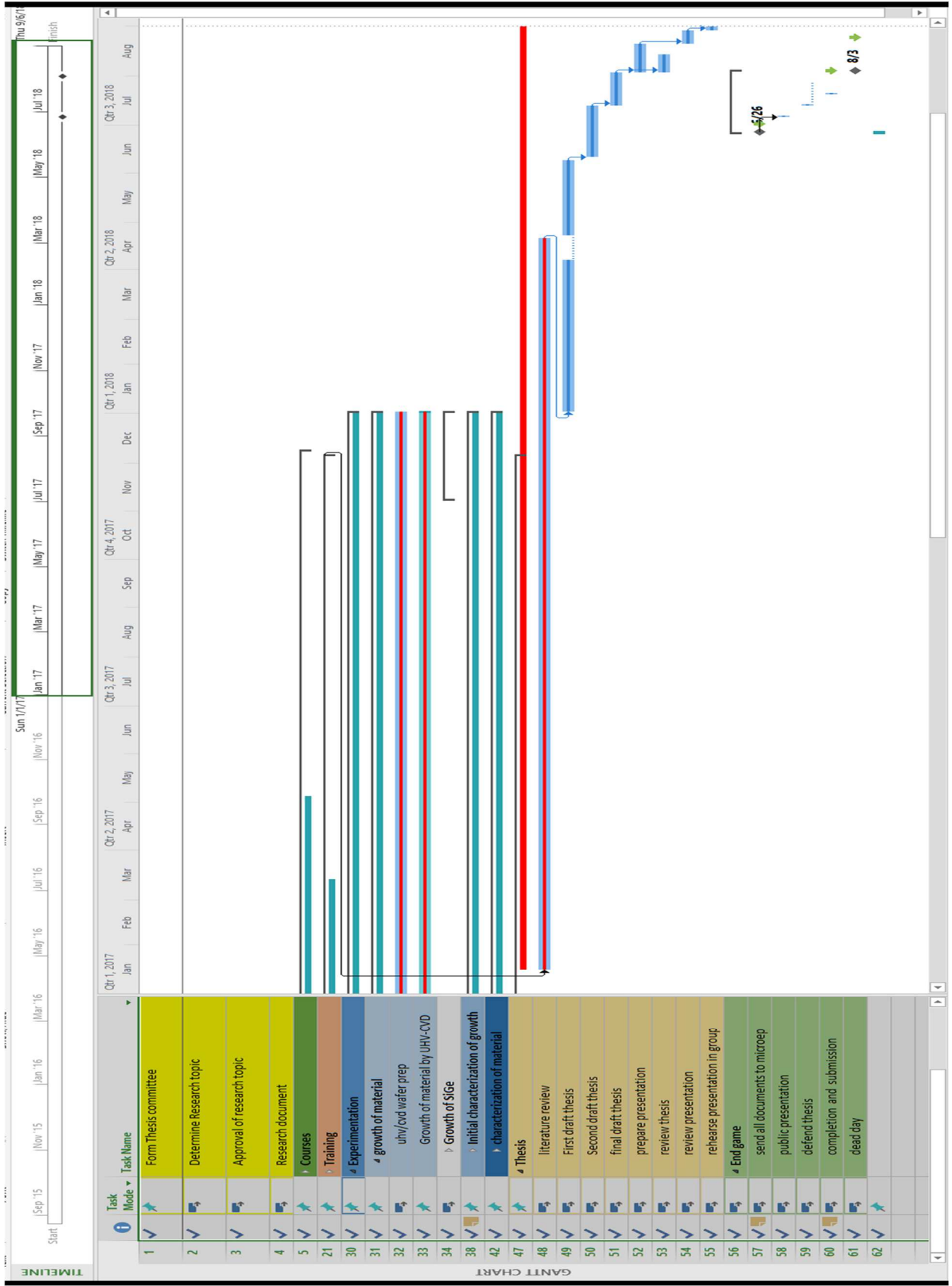
The results from this research has the potential to impact the environment in several ways. The (Si)GeSn materials would reduce the need to mine for rare earth metals that form the basis for many III-V materials. This would lead to a reduction of the impact on local ecosystems where these materials are located as their demand decreases. This would lead to less pollution and other effects to the environment in those areas. The increased power efficiency of devices and systems using the on-chip integrated optoelectronics would lead to a reduction in the demand for natural gas, oil, and coal as the demand for power on the global power grids is reduced. The integration of these (Si)GeSn materials into solar cell applications has the potential to increase solar cell efficiency that would allow for the production of more renewable energy from solar applications further reducing the demand for fossil fuels for power generation. The development of these materials beyond their current level has the potential to not only improve how our world

communicates and operates but could eventually improve the world as a whole for everyone.

# Appendix E: Microsoft Project for MS MicroEP Degree Plan







## **Appendix F: Identification of All Software Used in Research and Thesis Generation**

### **Computer #1:**

Model Number: GP70 2QF-486US-GG7472H8G1T0S81M

Serial Number: GP70 2QF-486USK1503000097

Location: Personal laptop

Owner: Joshua M. Grant

### Software #1:

Name: Microsoft Office 2016

Purchased by: Electrical Engineering Department, University of Arkansas

### Software #2:

Name: Microsoft Project 2018

Provided by: Electrical Engineering Department, University of Arkansas

### Software #3:

Name: Mendeley

Purchased by: Free download available from Mendeley.com

### Software #5

Name: OriginPro 2018

Purchased by Joshua M. Grant

### Software #6

Name: Autocad Inventor Design Suite 2018 (student version)

Purchased by Joshua M. Grant

### **Computer #2:**

Model Number: Dell Vostro

Serial Number: 52M6XK1

Location: ENRC Room 2923

Owner: Dr. Shui-Qing Yu

### Software #1:

Name: SynerJY with built-in Origin software

Purchased by: Dr. Shui-Qing Yu

### **Computer #3:**

Model Number: Dell Inspiron

Serial Number: 52M6XK1

Location: ENRC Room 2923

Owner: Dr. Shui-Qing Yu

### Software #1:

Name: SynerJY with built-in Origin software

Purchased by: Dr. Shui-Qing Yu

## Appendix G: All Publications Published, Submitted, and Planned

### i. Articles in Refereed Journals

#### 2018

9. Thach Pham, Huong Tran, Joe Margetis, Yiyin Zhou, Wei Dou, Perry C. Grant, **Joshua M. Grant**, Sattar Alkabi, Emad Badrdeen, Wei Du, Tansel Karabacak, Greg Sun, Richard A. Soref, John Tolle, Baohua Li, Mansour Mortazavi, and Shui-Qing Yu, Si-based GeSn photodetectors towards mid-infrared imaging applications, In preparation, to be submitted to Nature Communications.
8. Bader Alharthi, Wei Dou, Perry C. Grant, **Joshua M. Grant**, Timothy Morgan, Aboozar Mosleh, Wei Du, Baohua Li, Mansour Mortazavi, Hameed Naseem, and Shui-Qing Yu, Growth of High Quality Ge Buffer using Plasma Enhancement via UHV-CVD System for Photonic Devices Applications, Submitted to Applied Surface Science, Under Review
7. Perry C. Grant, Wei Dou, Bader Alharthi, **Joshua M. Grant**, Huong Tran, Grey Abernathy, Aboozar Mosleh, Wei Du, Baohua Li, Mansour Mortazavi, Hameed A. Naseem, Shui-Qing Yu, UHV-CVD Growth of High Quality GeSn Using SnCl<sub>4</sub>: From Growth Optimization to Prototype Devices, Submitted to Journal of Applied Physics, Special Topic: Highly Mismatched Semiconductors Alloys: from Atoms to Devices, Under Review.
6. Wei Dou, Bader Alharthi, Perry C. Grant, **Joshua M. Grant**, Aboozar Mosleh, Huong Tran, Wei Du, Mansour Mortazavi, Baohua Li, Hameed Naseem, and Shui-Qing Yu, “Crystalline GeSn growth by plasma enhanced chemical vapor deposition,” Opt. Mater. Express **8**, 3220-3229 (2018).
5. Huong Tran, Thach Pham, Wei Du, Yang Zhang, Perry C. Grant, **Josh M. Grant**, Greg sun, Richard A. Soref, Joe Margetis, John Tolle, Baohua Li, Mansour Mortazavi, and Shui-Qing Yu, High performance Ge<sub>0.89</sub>Sn<sub>0.11</sub> photodiode for low-cost shortwave infrared imaging, Journal of Applied Physics 124, 013101 (2018); doi: 10.1063/1.5020510.
4. Bader Alharthi, **Joshua M. Grant**, Wei Dou, Perry C. Grant, Aboozar Mosleh, Wei Du, Mansour Mortazavi, Baohua Li, Hameed Naseem, and Shui-Qing Yu, Heteroepitaxial Germanium-on-Silicon Using RF Plasma Enhancement for Ultra-High Vacuum Chemical Vapor Deposition, Journal of Electronic Materials (2018), doi.org/10.1007/s11664-018-6315-5.

#### 2017

3. Perry C. Grant, Wei Dou, Bader Alharthi, **Joshua M. Grant**, Aboozar Mosleh, Wei Du, Baohua Li, Mansour Mortazavi, Hameed A. Naseem, and Shui-Qing Yu, Comparison study of

the low temperature growth of dilute GeSn and Ge, Journal of Vacuum Science & Technology B, Nanotechnology and Microelectronics: Materials, Processing, Measurement, and Phenomena 35, 061204 (2017); doi: 10.1116/1.4990773.

## **2015**

2. Sattar Al-Kabi, Seyed Amir Ghetmiri, Joe Margetis, WeiDu, Aboozar Mosleh, Murtadha Alher, Wei Dou, **Joshua M. Grant**, Greg Sun, Richard A. Soref, John Tolle, Baohua Li, Mansour Mortazavi, Hameed A. Naseem, and Shui-Qing Yu, Optical Characterization of Si-Based  $Ge_{1-x}Sn_x$  Alloys with Sn Compositions up to 12%, Journal of Electronic Materials, DOI: 10.1007/s11664-015-4283-6 (2015)
1. Aboozar Mosleh, Murtadha Alher, Larry C. Cousar, Wei Du, Seyed Amir Ghetmiri, Tach Pham, Benjamin R. Conley, **Joshua M. Grant**, Greg Sun, Richard A. Soref, Baohua Li, Hameed. A. Naseem, and Shui-Qing Yu, Direct growth of  $Ge_{1-x}Sn_x$  films on Si using a cold-wall ultra-high-vacuum chemical-vapor-deposition system, Frontiers in Materials, vol. 2, pp. 30 (2015).

## **ii. Articles and Abstracts in Conference Proceedings**

## **2018**

5. W. Dou, P. Grant, **J. Grant**, H. Tran, W. Du, M. Mortazavi, B. Li, H. Naseem, S.-Q. Yu, Bader Alharthi, Buffer-free GeSn on Si Substrate by Plasma Enhanced Chemical Vapor Deposition, MIOMD 2018 (Flagstaff, Arizona), WeA9.
4. **J. Grant**, W. Dou, B. Alharthi, H. Tran, A. Mosleh, W. Du, B. Li, M. Mortizavi, H. Naseem, S.-Q. Yu, Perry Grant, Growth and Characterization of GeSn using UHV  $\square$  CVD System, MIOMD 2018 (Flagstaff, Arizona), WeA6.
3. Huong Tran, Thach Pham, Wei Du, Yang Zhang, Amir Ghetmiri, Perry C. Grant, **Joshua M. Grant**, Greg Sun, Richard A. Soref, Joe Margetis, John Tolle, Baohua Li, Mansour Mortazavi, and Shui-Qing Yu, Systematic Study of  $Ge_{0.89}Sn_{0.11}$  Photodiodes for Low-Cost Shortwave Infrared Imaging, CLEO 2018 (San Jose): Science and Innovations, STh4I. 2.

## **2017**

2. P.C. Grant, W. Dou, B. Alharthi, **J. Grant**, A. Mosleh, W. Du, B. Li, M. Mortizavi, H.A. Naseem, S.-Q. Yu, Dilute GeSn: A study on the Effects of Adding Stannic Chloride to UHV-CVD Growth, EMC 2017.
1. Bader Alharthi, **Joshua M. Grant**, Wei Dou, Perry C. Grant, Aboozar Mosleh, Wei Du, Mansour Mortazavi, Baohua Li, Hameed Naseem, and Shui-Qing Yu, Low Temperature Ge Growth Using Plasma Enhanced CVD Technique, EMC 2017.